eXPRESS Polymer Letters Vol.10, No.4 (2016) 273
Available online at www.expresspolymlett.com
DOI: 10.3144/expresspolymlett.2016.25

Editorial corner – a personal view
Development of antimicrobial polymers by incorporation of bacteriophages

*J. Puiggalí**

Chemical Engineering Department, Polytechnic University of Catalonia (UPC), Barcelona, Spain

Bacterial adhesion and proliferation on the surface of materials is a current cause of severe health and environmental problems. Bacteria can be organized in colonies with functional heterogeneity, forming biofilms where microorganisms can survive for long periods of time, especially in hospital environments. *Staphylococcus aureus* is probably the most dangerous type of bacteria associated with hospital infections since some strains become drug-resistant. In this sense, the use of natural agents like phages is receiving increasing attention. Phage therapy was developed in the Soviet Union. At present, the main research center is located at the George Eliava Institute in Tbilisi, Georgia. The extensive use of phages demonstrated their great specificity and efficacy in lysing targeted pathogens, as well as high ability to be quickly modified through natural selection and act against newly arising bacteria threads. Biotechnological companies around the world continue exploring the potentiality of phage therapy since it can find a niche in the Western medicine. However, regulatory and manufacturing practices, as well as profits, are yet not well-established, and consequently great difficulties exist in commercializing products. In this sense, academic centers should play a fundamental role.

PhagoBioDerm is an example of a commercial product that is highly efficient in treating patients with venous stasis ulcers, in promoting the healing of wounds or even prevention of infections (DOI: 10.1046/j.1365-4362.2002.01451.x).

Different methodologies have been proposed to incorporate phages into a polymer surface. For example, plasma treatment functionalizes inert polymers like polyethylene with COOH groups at which phages could be covalently anchored while retaining their activity (DOI: 10.1021/bm400290u). Efforts are also focused on incorporating phages into electrospun scaffolds because of their wide use in tissue engineering. Chemical attachment onto microfiber surfaces, adsorption on scaffold surfaces (e.g. by using cationic biodegradable polymers such as poly(ester amide)s based on arginine amino acid (DOI: 10.1021/bm5005977)) and encapsulation of phages during electrospinning are methodologies that are being developed. In the last case, it should be guaranteed that activity will not be lost as a consequence of the high applied electric field or the use of an organic solvent. Dual, coaxial and miniemulsion electrospinning may allow the use of an aqueous environment to protect phages, becoming suitable methods with a great potential for phage therapy.

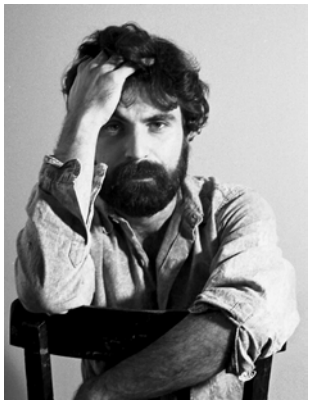

Prof. Dr. Jordi Puiggalí
Member of International Advisory Board

*Corresponding author, e-mail: Jordi.Puiggali@upc.edu

eXPRESS Polymer Letters Vol.10, No.4 (2016) 274–288
Available online at www.expresspolymlett.com
DOI: 10.3144/expresspolymlett.2016.26

Composition dependence of the synergistic effect of nucleating agent and plasticizer in poly(lactic acid): A Mixture Design study

M. K. Fehri[1], C. Mugoni[2], P. Cinelli[1], I. Anguillesi[1], M. B. Coltelli[1], S. Fiori[3], M. Montorsi[2], A. Lazzeri[1]*

[1]Inter University Consortium of Materials Science and Technology (INSTM) c/o University of Pisa, Department of Civil and Industrial Engineering - DICI, Largo Lucio Lazzarino 1, 56122 Pisa, Italy
[2]University of Modena and Reggio Emilia, Department of Engineering Sciences and Methods – DISMI, via Amendola 5, 42122 Reggio Emilia, Italy
[3]Condensia Química S.A, C/ La Cierva, 8; P.I.: Can Cortés, 08184 Palau-Solitá i Plegamans, Barcelona, Spain

Received 31 July 2015; accepted in revised form 19 October 2015

Abstract. Blends consisting of commercial poly(lactic acid) (PLA), poly(lactic acid) oligomer (OLA8) as plasticizer and a sulfonic salt of a phthalic ester and poly(D-lactic acid) as nucleating agents were prepared by melt extrusion, following a Mixture Design approach, in order to systematically study mechanical and thermal properties as a function of composition. The full investigation was carried out by differential scanning calorimetry (DSC), dynamic mechanical thermal analysis (DMTA) and tensile tests. The crystallization half-time was also studied at 105 °C as a function of the blends composition. A range of compositions in which the plasticizer and the nucleation agent minimized the crystallization half-time in a synergistic way was clearly identified thanks to the application of the Mixture Design approach. The results allowed also the identification of a composition range to maximize the crystallinity developed during the rapid cooling below glass transition temperature in injection moulding, thus allowing an easier processing of PLA based materials. Moreover the mechanical properties were discussed by correlating them to the chemical structural features and thermal behaviour of blends.

Keywords: *biodegradable polymers, mixture design, poly(lactic acid), plasticizer, nucleating agents*

1. Introduction

For applications where selective collection and chemical-mechanical recycling are not economical or feasible, the use of some specific bio-polymers would enable bio-recycling, particularly in the field of packaging. During the last decade, among biodegradable and biocompatible polymers, Poly lactic acid (PLA) has been considered as a potential alternative for oil derived plastic materials on the basis of its good processability, and relatively low cost [1]. The commercial PLA consists mainly of L-lactic acid units but it contains a few percentage by weight of D-lactic acid units. The content of D-lactic acid units in commercial PLA is different in dependence of the final specific grade, developed to fulfil the final application requirements. Although some modulation of properties was achieved by controlling the D-monomer content in the polymer, its applications are anyway limited by the low glass transition (about 60 °C), the brittleness, and the intrinsic low crystallization rate [2–6].

In order to overcome limitations in some properties, additives such as polymers [7, 8], fillers [9, 10] or plasticizers can be used also in combination [11, 12].

*Corresponding author, e-mail: a.lazzeri@ing.unipi.it

Plasticizers such as poly (ethylene glycol) [13], oligomeric lactic acid [14, 15], citrate esters [16] are frequently used to tune PLA mechanical properties increasing its ductility. In terms of thermal properties the addition of a plasticizer usually results in a strong increase in spherulitic growth rate with respect to pure PLA. The effect of plasticization was also studied in PLA based blends by Quero *et al*. [17]. They studied the effect on PLA crystallization rate of the acetyl tri-n-butyl citrate (ATBC) plasticizer and of poly(butylene adipate-co-terephthalate) (PBAT). The addition of the plasticizer resulted in a decrease in glass transition temperature of PLA. However the addition of increasing amount of PBAT resulted in an increase in PLA glass transition temperature as a consequence of preferential migration of ATBC in the PBAT phase [16] and a general synergistic effect was evidenced on the overall crystallization rate of the PLA component when both PBAT and ATBC were added to PLA.

In the industrial production usually PLA is melt processed and then rapidly cooled [2] below its glass transition temperature. As the crystallization of PLA is slow, final products (such as injection moulded or blow moulded parts or containers) are mainly amorphous. Thus the increase of temperature above PLA glass transition during the further processing steps (e.g. in the packaging of hot products) or during the use of the material, can enable cold crystallization, resulting in undesired shrinkages leading to dimension instability and deformation of the items. In addition, an increase in brittleness and change in optical properties can be observed as a consequence of crystallinity increase. In particular, for packaging of 'hot-filled' food or beverage bottles or other containers, i.e. filled at the food-manufacturing or beverage-bottling plant while the food or beverage is still hot from pasteurization, amorphous PLA is not suitable. Thus the use of proper nucleating agents, allowing increasing the crystallization rate of PLA during the rapid cooling is particularly interesting on a technological point of view. In PLA [18, 19] nucleating agents are reported to much affect the crystallinity content because they promote the formation of a high number of crystallization nuclei, thus consequently influencing also crystal growth and transparency [20]. Nucleated PLA thus results stabilized and its optical and mechanical properties are not modified as a consequence of heating in the temperature range of its glass transition.

Much attention is thus devoted to PLA nucleating agents, organic [21–23], such as sodium benzoate, or inorganic, such as calcium carbonate, talc, boron nitride [24, 25] to better tune crystallization rate and final crystallinity content. Nano-fillers, such as cellulose nano-whiskers [26], carbon nano-tubes [27] or graphene oxide [28] were also reported to act as nucleating agents for PLA, although composition and geometrical characteristics of the nano-fillers were reported to have a strong effect on overall crystallization rate. In general, a planar structure in organic molecules or rigid surface in nano-fillers and also groups interacting with polyester chains (also leading to chain scission [21]) are characteristics typical of all the effective nucleating agents, indicating that both the formation of specific directional linkages or confinement effects can affect the mobility and orientation at a molecular scale, thus influencing crystals formation.

Interestingly the effect of a plasticizer and a nucleating agent can be combined [29, 30]. For instance You *et al*. [31] used dibenzylidene sorbitol as organic nucleant agent, PEG as plasticizer and a multifunctional reactive molecule. Dibenzylidene sorbitol nanofibrils formed in the PEG gel, could supply active nucleating sites for PLA when the gel is added in PLA. The reactive molecules can introduce extra interaction between PLA macromolecules and Dibenzylidene sorbitol nanofibrils, which makes the nucleation easier and faster. Yu *et al*. [32] studied the cold crystallization of materials based on PLA containing talc and plasticized with compressed carbon dioxide. They reported that a plasticizer can increase the crystallization rate through accelerating the spherulite growth rate thanks to the increased mobility of the polymeric chains, while a nucleating agent can enhance the crystallization rate by increasing the nuclei density. Li and Huneault [33] investigated the combined effect of both plasticizer (acetyl triethyl citrate) and nucleating agents (talc, sodium stearate and calcium lactate) on mechanical and thermal properties of PLA. In the non-isothermal DSC experiments, the crystallinity developed upon cooling was systematically studied at different cooling rates. The non-isothermal data showed that the combination of nucleating agent and plasticizer is necessary to develop significant crystallinity at high cooling rates. A sort of synergy was thus observed, but the composition range in which this synergy can be obtained and the trend of properties as a function of

composition of the ternary systems was not determined in a systematic way.

Oligomeric poly(lactic acid)s are newly conceived plasticizers developed for the plasticization of PLA and biodegradable polymers obtained from bio-renewable raw materials and fully biodegradable and bio disposable. When they are used in PLA they allow obtaining stretched films with excellent mechanical properties without loss of transparency [14, 15]. However their effect combined with nucleating agents has never been studied.

In the field of nucleating agents the commercial product LAK (an aromatic sulfonate) is reported to provide a high crystallinity, high heat-stability of PLA mould parts and allows the onset of cold crystallization beginning at higher temperature [34]. PDLA was also found to behave as a nucleating agent for decreasing the half-time of crystallization [35] of PLA, with the advantage of the excellent compatibility because of the much similar structure and also thanks to the formation of stereocomplexes [36, 37]. More recently Shi *et al*. [38] evidenced again the synergistic effect of nucleating agents and plasticizer by plasticizing PLA with PEG and adding also different nucleating agents such as PDLA, LAK and talc. LAK and PDLA effects were reported to be different and both promising because LAK showed an effective promotion of PLA crystallization behavior due to heterogeneous nucleation, while the addition of PDLA to PLA resulted in the formation of PLA stereocomplexes, acting as another type of nucleation process. In the paper of Shi *et al*. [38] a combination of LAK as nucleation agent and talc, used also as reinforcing filler, was reported to allow a good combination of properties, as the crystallization half-time was reduced and, regarding the mechanical properties, an improved ductility of the material was attained. However, any evidence about what can be the trend of thermal and mechanical behaviour as a function of composition was not reported.

The present work, is devoted to investigate the use of a biodegradable plasticizer Glyplast OLA8 (OLA8) based on oligomeric PLA, in combination with nucleating agents, poly(D-lactic acid) (PDLA) or LAK301 (LAK), in PLA formulation in order to improve the mechanical and thermal properties of PLA controlling its processing. In particular, in order to systematically study this system as a function of composition, in the present study the effects of four mixture components PLA, OLA8 (as plasticizer) and LAK and PDLA (as nucleating agents) on the thermal and mechanical properties of the blends were investigated by using multivariate statistical methods which allowed identifying the compositional region where the crystallization rate is maximized and where a synergistic effect between plasticizer and nucleation agents can be observed. The work was planned using an extension of the Design of Experiments (DoE) method called Mixture Design approach, in which the weight fraction of formulations components constitute the input factors. DoE represents a very important tool complementary to the traditional approaches (based on one factor variation at a time) in order to improve the performances of the process correlated both to the material design and to its synthesis [39]. Specifically, the Mixture Design considers the different components of formulation as not completely independent from each other, allowing estimating how the ratios between ones to each other directly affect the target properties [40].

2. Experimental section

2.1. Materials and methods

PLA NatureWorks LLC INGEO 2003D, (average molecular weight 200 000, melting point temperature T_m = 160 °C, glass temperature T_g = 55–58 °C; D-lactic acid content in the range 4–4,5% [41]) has been used. The plasticizer Glyplast OLA8 (Figure 1), an alkyl terminated oligoester of lactic acid, and the PDLA were provided by Condensia Quimica, Spain. LAK-301 (LAK) is an aromatic sulfonate derivative produced by Takemoto oil&fat Co.Lt, Japan and currently employed in Ingeo(TM) 3801X (NatureWorks, PLA resin) formulation as nucleating agent.

The blends extrusion was carried out in a Haake Minilab at 180 °C, 90 rpm, recovering the molten material after 1 min of recirculating time. The start-

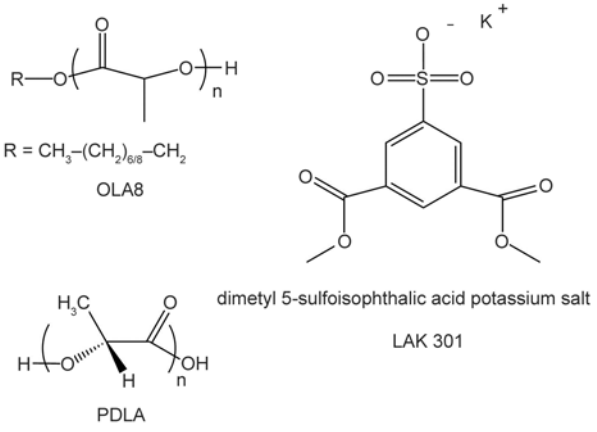

Figure 1. Structure of the additives used in this work

ing polymers were previously dried at 60 °C in vacuum for four days. After extrusion, the molten materials were transferred through a preheated cylinder to the Haake MiniJet II mini injection moulder (Thermo Scientific Haake GmbH, Karlsruhe, Germany), operating at 650 bar pressure, mould temperature of 35 °C, for 15 sec, to obtain Haake type 3 specimens (557–2290) used for measurements and analysis. The specimens were placed in plastic bags for vacuum sealing to prevent moisture absorption. Tensile tests were carried out on an Instron 5500R universal testing machine at 10 mm/min with a load cell of 1 kN. By this tests the elastic modulus (E), the stress at break (σ_b), the yield stress (σ_y) and the elongation at break (ε_b) were determined.

DSC measurements for determining the thermal properties and time of crystallization were carried out on a DSC Q200 TA instrument, setting a first run from 20 °C to 190 at 10°C/min, an isothermal step of 5 min at 190 °C, a fast cooling step to 105 °C, and an isothermal step at 105 °C for 30 min. The latter step was performed to measure the crystallization half-time $t_{1/2}$, since it has to be at least three times longer than the time required for crystallization. Finally the sample is heated up to 190 °C at 10 °C/min.

The blends crystallinity, developed during the rapid cooling (15 seconds) in the mini injection moulder, is determined by calculating the difference (ΔH_m) between the area under the melting peak and the area under the cold crystallization peak. Thus the crystallinity of PLA (% cryst. I) was determined according to Equation (1):

$$\%\ cryst.\ I. = \frac{\Delta H_m}{\Delta H_{100\%C}} \cdot 100 \qquad (1)$$

where $\Delta H_{100\%C}$ is the melting enthalpy of 100% crystalline PLA (93.0 J/g).

From the thermogram of the final heating step the area of the melting peak (ΔH) and the percentage of crystallinity developed after the isothermal process (% cryst. II) were also calculated.

Dynamic mechanical thermal analysis was performed on a GABO Eplexor 100N Instrument, working in tensile mode, on 20×5 mm specimen cut from the Haake type 3 specimens, with an average thickness of 1.6 mm, at a heating rate of 2 °C/min, from –100 to 150 °C, and 1 Hz frequency. By means of the dynamic mechanical thermal the glass transition temperature was determined.

The compositions investigated in this study were planned by using the Mixture Design in which two main constrains were used: the first regarding the proportion of the constituent proportion x_i in the mixture (Equation (2)):

$$0 \le x_i \le 1, \quad i = 1, 2, 3 \ldots q, \quad \sum_{i=1}^{q} x_i = 1 \qquad (2)$$

where q are the constituents. The second regards the additional boundary constrains on the constituent proportion.

In mixture design, there are some additional boundary constraints on the constituents proportion (x_i), which limit the feasible space of components between the lower (L_i) and the upper (U_i) constraints. The general form of the constrained mixture problem is given by (Equation (3)):

$$i = 1, 2, 3, \ldots. Q, \quad 0 < L_i < x_i < U_i < 1 \qquad (3)$$

Restrictions reported in Equation (3) reduce the constraint region given by Equation (2) to an irregular dimensional space.

Mixture models, most commonly used in fitting data, are the functions known as the Scheffé canonical [37] polynomials (Equation (4)) and given by:

$$E(Y) = \sum_{i=1}^{q} \beta_i x_i + \sum_{i<j}^{q} \sum^{q} \beta_{ij} x_i x_j \qquad (4)$$

where $E(Y)$ is the response, β_i and β_{ij} are the regression coefficients calculated from the experimental data by multiple regression, and x_i and x_j are the levels of the independent variables. Table 1 reports the components considered in this work and their specific range.

The resulting experimental region is an irregular polyhedron, thus the mixture components were transformed in U-Pseudo components (reported in Table 1 as Low and High coded), where the maximum value of each component becomes zero and the minimum value approaches one, according to equation reported in literature [40, 42].

Table 1. Composition data and their ranges

Component	Name	Low actual	High actual	Low coded	High coded
A	OLA8	0.05	0.20	0.750	0
B	PLA	0.7	0.90	1.000	0
C	LAK	0	0.05	0.250	0
D	PDLA	0	0.05	0.250	0

Table 2. Experimental plan

Sample	Order of run	OLA 8	POLY L	LAK	PDLA
1	11	0.066	0.834	0.05	0.05
2	2	0.200	0.700	0.05	0.05
3	7	0.100	0.900	0	0
4	6	0.138	0.812	0	0.05
5	4	0.200	0.722	0.028	0.05
6	14	0.200	0.782	0	0.018
7	10	0.200	0.750	0.05	0
8	15	0.133	0.805	0.037	0.025
9	8	0.056	0.900	0.009	0.035
10	3	0.055	0.890	0.05	0.005
11	1	0.129	0.820	0.026	0.026
12	5	0.129	0.820	0.026	0.026
13	9	0.129	0.820	0.026	0.026
14	12	0.129	0.820	0.026	0.026
15	13	0.129	0.820	0.026	0.026
16	16	0.200	0.782	0	0.018

Sixteen experiments, including five center points (that are also replicated points) were planned as detailed in Table 2. The experiments were performed according to the randomized run order. In most of the tested formulations LAK and PDLA were simultaneously present.

For E, σ_b, σ_y, T_g, $t_{1/2}$, % cryst I, % cryst II and ΔH different models were analyzed and their validity were ascertained through the ANOVA analysis by using commercially available software (Design Expert 7, Stat-Ease). The resulting models allowed describing the relationships between the starting composition and the final measured responses.

2.2. Data analysis

The regression analysis of the data was conducted by the analysis of variance called ANOVA. It is a statistical method in which two F-tests (F-test of the model and lack of fit test) were used to assess the validity of the model [40, 42].

The residual analysis is generally used to point out potential deviating experiments. The regression coefficients of the model were analysed and all the terms with a p-value higher than 0.05 were not considered as statically significant and therefore neglected in the model formulation. The trace and the response contour plots are used for a deeper explanation of the role of the mixture components on the final properties. The interpretation of these plots is strongly connected to the use of U-pseudo components used in this work.

In detail, the trace plot shows the effects of changing each component (main effect) along an imaginary line from the reference blend (defaulted the center point) to the vertex. In this plot, the effect (y-axis) produced by the factor variation (x-axis) should be interpreted considering that each component is at the lower real value in the right side of the x-axis, and it is at the higher real value in the left side of the same axis. Generally, the graph lines explain the effect of each component on the analysed response; a horizontal line (the slope is zero) implicates that the response value does not change varying the amount of a component while linear or parabolic trend indicates a strong variation of the response value (keeping the ratio on the proportions of the remaining components constant at the reference mixture) depending by the composition [38]. The response contour plot shows graphically the obtained results also in terms of interactions and quadratic effects and it is also helpful for choosing the best point at which the desired final properties can be satisfied (optimization perspective). In the contour plot the amount of each factor changes in the opposite way with respect to the usual one in simplex lattice design [38].

3. Results and discussion

3.1. Mechanical properties

The experimental results of tensile tests (E, σ_y, ε_y, σ_b, ε_b) and dynamic thermal mechanical analysis (T_g) are reported in Table 3.

A general good reproducibility of the experimental data is observed, because, especially for the E, σ_b, σ_y

Table 3. Results of mechanical tests and dynamic thermal mechanical analysis

Sample	Mechanical properties					DMTA
	E [GPa]	σ_y [MPa]	ε_y [%]	σ_b [MPa]	ε_b [%]	T_g [°C]
1	2.6	47	2.2	40	8.6	57
2	1.2	11	3.5	20	278	45
3	2.7	47	1.9	38	5.6	57
4	2.1	42	2.3	32	5.3	53
5	2.0	18	2.9	23	285	45
6	1.7	17	2.8	28	340	47
7	2.2	28	2.2	18	247	47
8	3.1	41	2.0	31	15.3	53
9	3.1	50	2.1	39	11.0	61
10	3.2	36	1.7	28	9.2	63
11	2.6	39	2.2	31	9.5	53
12	2.5	42	2.2	32	13.5	53
13	2.8	40	1.8	20	15.5	55
14	2.8	38	1.9	30	9.0	51
15	2.7	40	1.8	30	10.5	53
16	1.2	16	2.5	23	310	47

E: Young's modulus, σ_y: yield stress, ε_y: elongation at yield, σ_b: stress at break, ε_b: elongation at break, T_g: glass transition temperature

the values corresponding to the replicated tests (11, 12, 13, 14, 15 ,and 6, 16) are close to each other with a low variation compared to the variation of the entire data.

During the tensile test, all samples showed yielding, flow softening and even strain hardening. After yielding, on the specimen, a necking zone was observed and the neck extended until final fracture.

The effect of the selected input factors on the mechanical properties can be described using a linear model for E and σ_b, and a quadratic one for σ_y. The experiment 10 is not used in the data analysis of both σ_b and σ_y since it was highlighted as deviating experiments.

Table 4 summarizes the ANOVA results for each model.

The *F-values* are higher than one (p-value < 0.05), and the *Lack of Fit* is not significant (p-value > 0.05), thus satisfying the two F-tests. Moreover *R-Squared*, *Adj R-Squared* and *Pred R-Squared* for σ_b and σ_y are higher than 0.8 pointing out the validity of the model. On the contrary the ANOVA parameters for E are not excellent and particularly the Pred *R-Squared* value (0.51) clearly suggests that a more complex model should be developed in order to ensure an appropriate prediction power. Anyway, the aim of this work is mainly focused on a screening perspective, therefore all the models (including that for E) can be used to describe quantitatively and for E just qualitatively, the effect of the blend compositions on the mechanical properties.

Moreover, further analysis of the model coefficients (not reported in this work) suggests that only OLA8 and PLA play a significant role on elastic modulus E excluding any influence of both LAK and PDLA. The trace (reported as example of a trace plot) and contour plots reported in Figure 2a and 2b respectively, show in detail the influence of each factor on E. The first one (Figure 2a) clearly points out that decreasing the amount of OLA8 (from the left to the right side of the plot) the modulus of elasticity increases, while PLA produces the opposite effect. The same information can be also derived from the contour plot reported in Figure 2b. The correlation between E and the OLA8 content is in agreement with the plasticizing effect of this additive.

For the yield stress (σ_y) the overall results of the statistical analysis reveals that a decrease in PLA and LAK content leads to a decrease in σ_y, while by decreasing OLA8 and PDLA the σ_y value increases. For this properties the presence of quadratic terms in the model has been observed and among them the LAK*PDLA is the most significant one. Moreover, it is worth noting that the highest amount of LAK and the lowest amount of PDLA leads to the highest value of σ_y, as illustrated in Figure 3 (two components mix

Table 4. ANOVA results for the mechanical properties: modulus of elasticity (E), stress at break (σ_b), yield stress (σ_y)

	F-value	*p*-value[a]	*Lack of fit*	*p*-value[b]	*R-Squared*	*Adj R-Squared*	*Pred R-Squared*
E	11.70	0.0007	4.79	0.052	0.75	0.69	0.51
σ_b	47.30	< 0.0001	1.46	0.350	0.93	0.91	0.82
σ_y	168.32	< 0.0001	1.16	0.390	0.99	0.99	0.93

[a]*p*-value associated to the F-Test of the regression model
[b]*p*-value associated to the lack of fit test

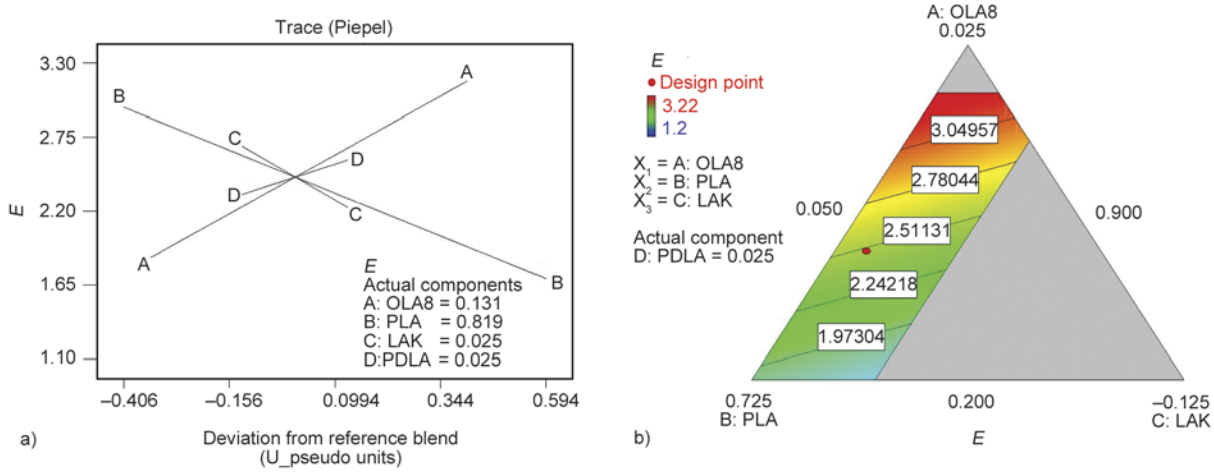

Figure 2. Trace (a) and contour plot (b) of E

graph). Possible explanation of the correlation between PDLA content and σ_y can be derived considering that this component in the blend can promote stereo complexes formation as detailed by Wei *et al.* [35]. In general, when PLLA/PDLA 1:1 solution casted blend are prepared the tensile properties E, σ_y and σ_b increase [36], because the formation of these complexes inside the blend structure leads to an increased structural rigidity due to the formation of a branched/crosslinked system but when the content of PDLA is lower in melt processed blend a decrease in these properties was recently observed [44, 45]. Probably the melt extrusion, having a short residence time, cannot allow an optimal dispersion of PDLA in PLA. In general, in PLA containing less than 10% of PDLA prepared in the melt, an effect onto crystallization behaviour and melt viscosity [46] of the formation of stereocomplexes is reported, but not significant improvement of tensile properties are observed [47]. The maximization of σ_y is thus essentially due to the synergy in increasing crystallinity content when both PDLA and LAK are used and will be more extensively discussed in the following.

As in the case of elastic modulus, the σ_y decreasing by increasing OLA8 concentration can be ascribed to the improved free volume between PLA macromolecules and increased mutual mobility of the PLA chains [36].

Concerning the stress at break (σ_b), which is a measure much dependent on the presence of defects in the material and less reliable than σ_y, the coefficients and the trace plot analysis (not reported) reveal that this property is mainly influenced by OLA8 and PLA content (p-value associated to each coefficient is less than 0.05) (Figure 4). Moreover, as observed for E, also in this case the most significant effect is played by the content of OLA8 in the blend. On the contrary, while a very slight effect of LAK is reported, the PDLA does not produce any significant variation on σ_b. In detail, by decreasing the OLA8 content σb increases whereas a decrease in the LAK content leads to a decrease of this mechanical property.

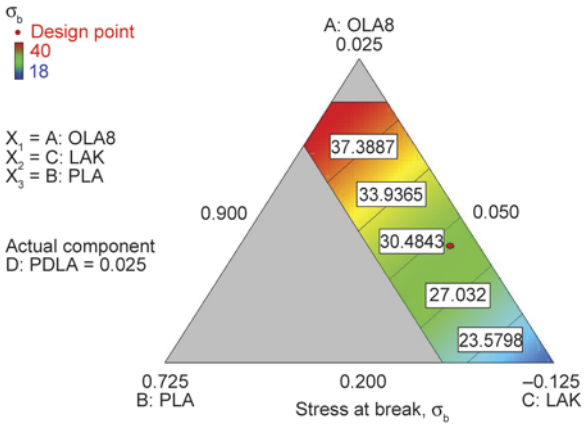

Figure 4. Contour plot of stress at break (σ_b)

The addition of OLA8 to PLA leads to reduction of T_g and also E, σ_y and σ_b as the normal effect of plasticization, thanks to the increased mobility of macromolecular chains at room temperature, making the material less resistant but more ductile. Interestingly σ_y varies monotonously with LAK concentration.

The statistical analysis for elongation at break ε_b is not reported since the model is not significant. The high values of elongation at break (>200%) at the highest content of OLA8 (20 wt%), are in agreement with the high miscibility of these additive with PLA [14, 15].

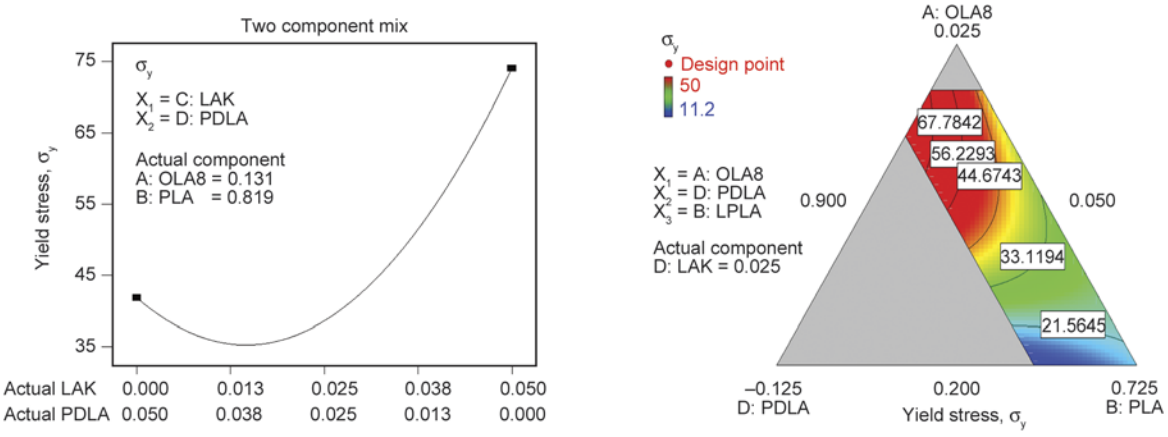

Figure 3. Two components mix graph (a) and contour plot (b) of yield stress (σ_y)

3.2. Thermal properties

The experimental results of DSC analysis reported in Table 5 are codified in terms of time to achieve 50% crystallization at 105 °C ($t_{1/2}$), crystallinity % determined at the first DSC scan (% cryst I) and crystallinity % determined at the second DSC scan (% cryst II). The glass transition temperature values, determined by DMTA tests (Table 4), were also codified as T_g.

In the DSC thermograms during the heating steps (I or II run) two peaks were observed in the melting region. The first peak can be attributed to the melting of more irregular α‘ crystals and the second to the more ordered α crystals [4].

In sample 3, without nucleating agents, there was no crystallization in isothermal treatment at 105 °C, therefore the isothermal crystallization parameters ($t_{1/2}$ and ΔH_c II) were not recorded. In this case the $t_{1/2}$ is higher than 1800 s. The use of PDLA alone (run 6) result in a $t_{1/2}$ of 151 s, in good agreement with the nucleating properties reported for this additive [35]. The use of LAK alone (run 7) determined the decrease of $t_{1/2}$ to 61 s, showing a better efficiency of LAK with respect to PDLA as yet reported by Shi *et al*. [38] for PLA plasticized with PEG.

LAK and PDLA were simultaneously present in most of the prepared samples and their synergy in nucleation, yet evidenced by Shi *et al*. [38], is evident by comparing the first heating scan of the plasticized PLA with the two nucleating agents (St 2) and the one with only LAK (St 7) (Figure 5). In the former trend the crystallization temperature is quite lower than in the latter, while the crystallinity is higher (Table 5). Moreover the $t_{1/2}$ is 48 s if both LAK and PDLA are used and it is 61 s if only LAK is added. The presence of only PDLA (run 4) resulted in a $t_{1/2}$ of 112 s. The presence of both the nucleating agents is thus necessary to increase effectively crystallization rate.

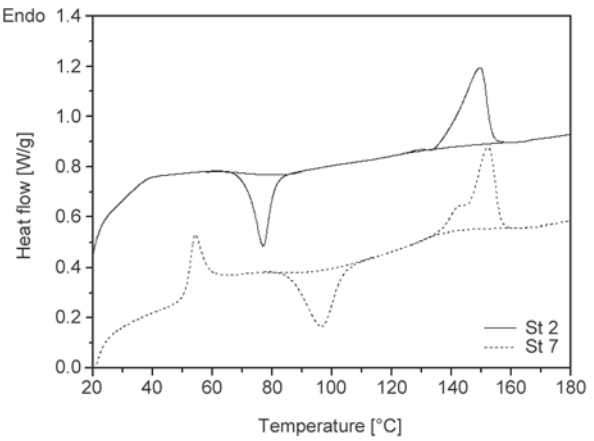

Figure 5. First heating thermogram of St 2 (with both LAK and PDLA) and St 7 (with only LAK)

Concerning the statistical analysis it is worth noting that for $\Delta H_{c\%}$, % cryst I and % cryst II significant models can be derived.

The experiment 5 (considered as an outlier by the residual analysis) is neglected in the ΔH_c, % cryst I and % cryst II statistical data analysis.

The ANOVA analysis shows that while the effect of the mixture components on T_g is well described through the linear model, for ΔH_c, % cryst I, % cryst. II and $t_{1/2}$ quadratic terms need to be

Table 5. Thermal properties of the investigated samples

	I Run					ISO *T* 105 °C		II Run			
St	**ΔH_c I [J/g]**	**T_{m1} [°C]**	**T_m [°C]**	**T_c [°C]**	**% cryst. I**	**$t_{1/2}$ [s]**	**ΔH_c II [J/g]**	**ΔH [J/g]**	**T_{m1} [°C]**	**T_m [°C]**	**% cryst. II**
1	0.25	134	152	87	0.3	51	32.5	21.5	140	151	23.1
2	6.1	130	150	77	6.5	48	14.0	14.7	140	150	15.9
3	1.5	141	155	97	1.6	n. d.	n. d.	23.4	144	154	25.1
4	0.2	140	153	87	0.3	112	41.0	21.3	142	153	22.9
5	6.8	136	152	76	7.3	46	18.0	12.2	140	151	13.1
6	4.0	133	152	84	4.3	151	50.6	20.7	140	151	22.2
7	3.9	143	152	97	4.2	61	20.5	16.2	145	153	17.4
8	3.0	141	153	94	3.3	60	24.5	19.6	145	153	21.1
9	4.4	144	155	98	4.7	152	56.2	23.2	146	155	24.9
10	2.6	145	155	100	2.8	76	16.0	21.1	147	155	22.7
11	3.2	137	153	91	4.6	38	19.0	22.5	143	154	24.1
12	4.3	136	152	90	4.6	40	20.3	22.2	143	153	23.8
13	7.9	138	158	91	4.5	45	20.0	21.4	144	153	22.9
14	5.1	136	152	88	4.5	44	23.0	20.4	142	152	21.9
15	5.1	138	153	90	4.5	41	20.5	22.5	143	153	24.2
16	4.3	132	150	83	4.5	152	45.7	21.4	139	150	23.0

included to improve the goodness of the models. In particular LAK*PLA for both % cryst II and ΔH_c, OLA8*PLA, OLA8*LAK, PLA*LAK, LAK*PDLA for % cryst I and OLA8*PLA, OLA8*LAK, OLA*LAK, OLA8*PDLA, PLA*PDLA for $t_{1/2}$. The models are consistent (p-values of the F-test < 0.05), the *Lack of Fit* is not significant and the model parameters (Table 6) reveal a good fitting and predictive power, except for $t_{1/2}$ for which a high difference between *R-Squared* and *Pred R-squared* (0.38) and data clusters were observed.

The normal distribution of the residuals for the investigated properties satisfy the statistical requirements and therefore are not reported here. Only for the $t_{1/2}$ the residual analysis suggests the presence of a fair normal distribution anyway the high values of *R-Squared* (0.99) and *Adj R-Squared* (0.99), together with an insignificant *Lack of Fit*, allow us to use the obtained model to explore the possible region of interest, as suggested in other works [43].

The coefficients analysis and the trace and contour plots for the T_g reported in Figures 6a and 6b suggests that OLA8 and PLA are significant factors in defining the T_g trend. In particular an increase in OLA8 leads to a decrease of T_g while an almost negligible similar effect of LAK was observed. The glass transition temperature value is thus mainly affected by OLA8 plasticization, increasing the mobility of macromolecular chains and thus reducing the temperature at which the flexible amorphous material can be converted in a rigid amorphous glass.

LAK and OLA 8 concentrations play a moderate effect on % cryst. II and ΔH_c (Figure 7 and Figure 8): decreasing OLA8 and LAK content leads to the increase of both the properties notwithstanding the effect of LAK is lower with respect to that produced by OLA8. These results show that when the material is annealed for long time at 105 °C, the presence of LAK does not lead to crystallinity increase. These results confirm that the effect of a nucleating agent is increasing the nuclei density, but as the number of nuclei is increased, for long annealing time, the crystal growth is limited, leading to crystallinity decrease with respect to not nucleated PLA. This effect was noticed for many other nucleation agents [4]. In a similar way the presence of plasticizer on one side increases the mobility of the chains favouring the crystalline packing, but on the other side introduces disorder in the system, partially replacing inter-macromolecular interactions, significant for crystals

Table 6. ANOVA results for the thermal properties glass transition temperature (T_g), crystallization enthalpy (ΔH_c) and percent crystallinity (% cryst. I and % cryst. II) and crystallization half-time ($t_{1/2}$)

	F-value	*p*-value[a]	*Lack of fit*	*p*-value[b]	*R-Squared*	*Adj R-Squared*	*Pred R-Squared*
T_g	108.6	<0.0001	0.67	0.70	0.96	0.95	0.93
ΔH_c	23.7	<0.0001	1.18	0.43	0.90	0.87	0.82
% Cryst. I	31.9	<0.0001	0.94	0.45	0.97	0.87	0.94
% Cryst. II	23.7	<0.0001	1.17	0.43	0.90	0.88	0.82
$t_{1/2}$	491.39	<0.0001	1.15	0.33	0.99	0.99	0.61

[a]*p*-value associated to the F-Test of the regression model
[b]p-value associated to the lack of fit test

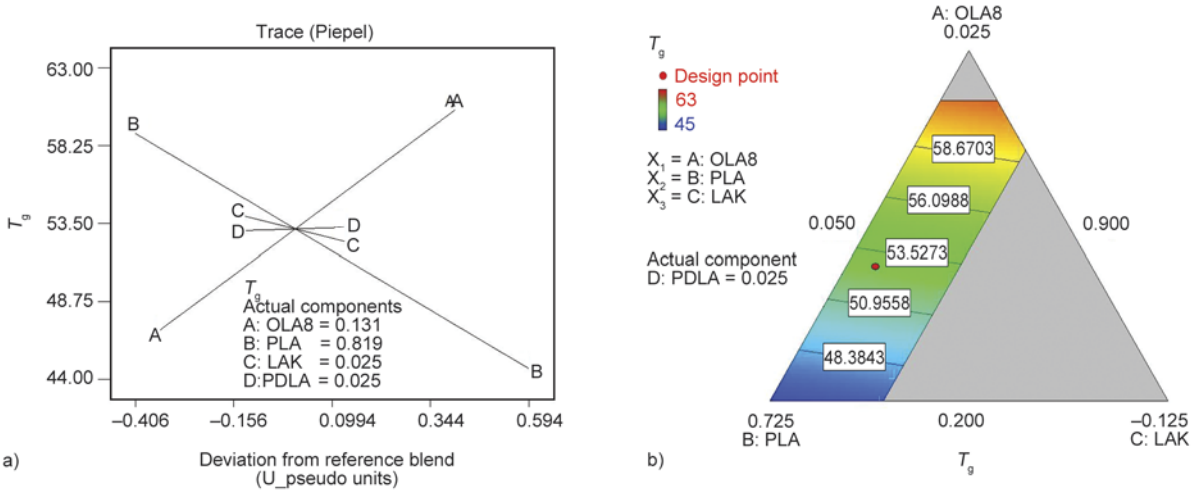

Figure 6. Trace (a) and contour plots (b) of glass transition temperature (T_g)

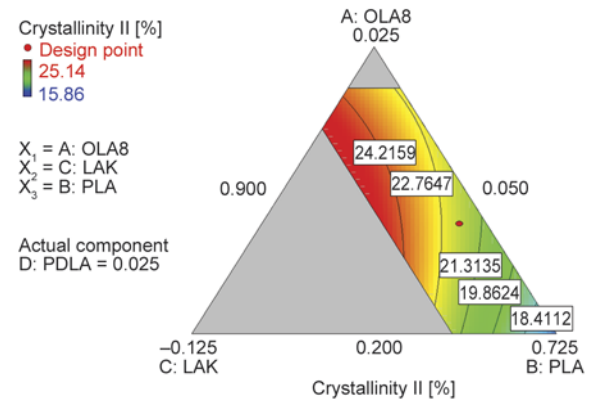

Figure 7. Contour plot of % Cryst. II

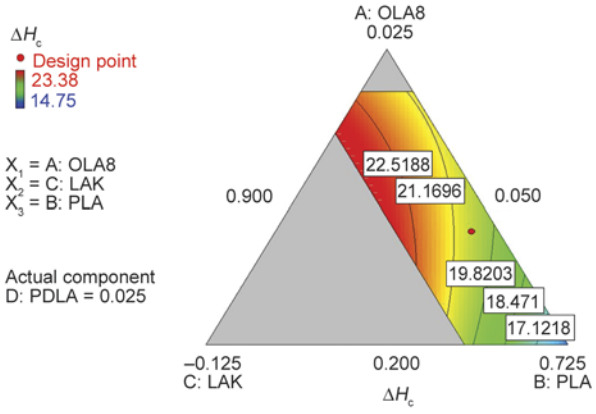

Figure 8. Contour plot of crystallization enthalpy ΔH_c

formation, with plasticizer-macromolecule ones. In the specific case of OLA8 the introduction of disorder is given by the presence of the terminal groups, as the chain structure is the same as PLA. Thermodynamic driving forces thus predominate on kinetic ones. This explains why for high annealing time the crystallinity decreases as a function of OLA8 content [32].

Differently, changes in PDLA content do not produce any variation of % cryst. II and ΔH_c.

The analysis of the crystallization half-time ($t_{1/2}$) shows that all terms, including the interaction ones, cover an important role in the variation of this property. From the trace plot (not showed) it was observed that both LAK and PDLA can contribute to a $t_{1/2}$ variation with a parabolic trend. From the low to the intermediate concentration of LAK the crystallization half-time decreases, but the further increase of LAK leads to an increase of $t_{1/2}$. PDLA has an opposite effect with respect to LAK. Moreover, it is worth noting that the region in which the crystallization half-time is at the minimum level, underlined in the contour plot in Figure 9, is the one in which significant crystallinity can be developed more rapidly.

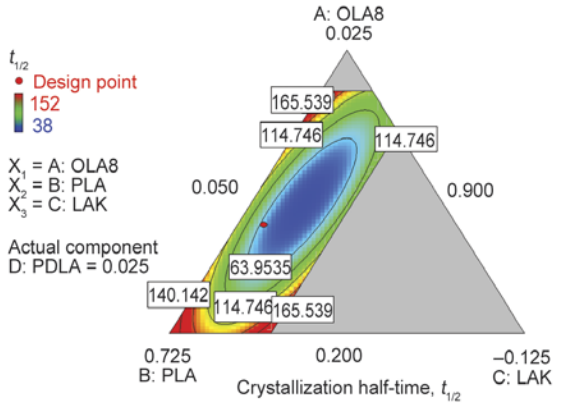

Figure 9. Contour plot of crystallization half-time $t_{1/2}$

On this trend a strong responsibility is played by the non-linear terms such as the OLA8*LAK: modifying this factor allows achieving the lower $t_{1/2}$ values.

The synergistic effect of plasticizer and nucleation agent in increasing the crystallization rate was already suggested and reported in literature but the important value added by this work derive by the definition of a specific region in which this synergy occurs. Hence, this study allows the understanding of the role played by each components and their mutual interaction on the $t_{1/2}$ decreasing [24, 32–33, 46]. The synergy of OLA8 and LAK plays a key role in the crystallization rate properties of the mixture and in particular, an intermediate concentration with respect of the explored range encounters the condition of maximum crystallization rate. In this peculiar range the optimal concentration of LAK to determine the increase of nuclei density is reached and the further addition of LAK is detrimental with respect to heterogeneous nucleation. On the other side an intermediate value of OLA8 content is required to minimize $t_{1/2}$. As the plasticizer is reported to increase the spherulitic growth rate [32] thanks to the increased mobility, we can observe that probably a high concentration of it introduces excessive dilution of macromolecular PLA chains in the system, thus limiting the growth rate. In the composition range where the minimum $t_{1/2}$ is found the correct balance between formation of nuclei rate and spherulitic growth rate can be found.

Since the development of crystallinity in its early stage covers a fundamental role during processing, especially during injection moulding, the % cryst. I (Figure 10), developed during the cooling in the injection molding press, represents a quite interesting technological parameter. The rapid development of crystallinity can allow the rapid development of

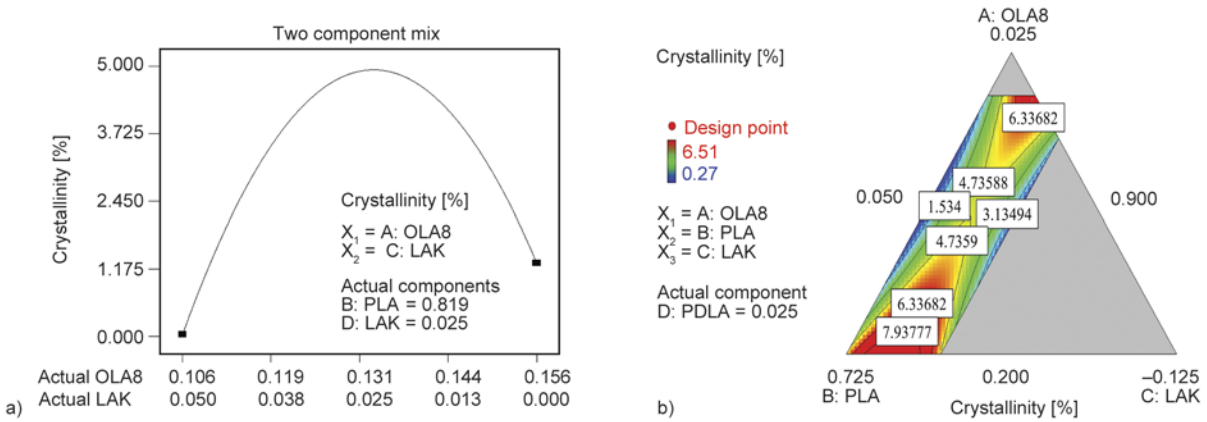

Figure 10. (a) Two components mix graph and (b) contour plot of % Cryst. I

mechanical resistance and the easy removal of the injection molded part from the mould assuring a short industrial cycle. Among the linear terms LAK displays the most important role, and its effect can be described considering that moving from the maximum to the intermediate value (while maintaining constant the ratio between the other components) an increase of the % cryst. I can be observed. On the contrary, further decrease in the LAK content (moving to the minimum value) leads to a decrease in the % cryst. I.

In agreement with $t_{1/2}$ results, an intermediate content of LAK with respect to the explored range can assure the highest content of crystallinity, probably thanks to the same capacity of increasing nuclei density up to an optimal concentration.

Concerning the crystallinity of the mixture a quite different trend is observed with respect to % Cryst. II. In fact a parabolic trend with a minimum was observed as a function of OLA8 content: the highest value of % Cryst. I is achieved when the content of plasticizer is the highest. This effect is in contrast with the trend observed for the use of only a plasticizer in PLA, because usually the crystallinity developed during rapid cooling increases by increasing the plasticizer content [16, 29, 30]. In this case is the heterogeneity introduced by the plasticizer in nucleating crystals. This is in agreement with the recent use of miscible polymers as nucleating agents [20]. On the other hand, in the presence of a nucleating agent the beginning of crystals growth occurs starting on the nuclei surface. When the concentration of plasticizer is low (up to 10%), it hinders the crystal growth with respect to pure PLA. As the chemical structure of OLA8 is identical to the one of PLA, this action is certainly attributable to the higher concentration of terminals, creating local disorder and thus disabling crystal packing close to nucleating agent surface. It is possible to hypothesize that the terminal groups are more concentrated close to the nucleating agent surface because of the attraction between the terminal groups of OLA and the polar groups on the LAK particles surface. On the contrary, when the concentration is high the main effect of OLA8 is allowing the spatial separation of macromolecules providing a higher free volume for segments motions, allowing the chains fragments to assemble in crystals more easily. Hence the plasticizer, which was reported to favour in general crystal growth [32], is found here to disturb crystal growth in the early stage of crystal formation if present at intermediate concentration and to favour it if present at high concentration. Hence during the rapid cooling below glass transition the availability of free volume is confirmed to be a factor that improves crystal growth rate on a kinetic point of view but only at high OLA8 content.

3.3. Comparison between thermal and mechanical data

Thermal data related to the first DSC heating step and mechanical data can be correlated as resulting from testing on specimens underwent to identical thermal treatment. The application of the Mixture Design approach to PLA containing a plasticizer and two different nucleating agents evidenced that the mechanical properties, such as E, σ_b and σ_y decreased by increasing OLA8 because of plasticization. On the other hand the crystallinity % Cryst. I correspondingly showed a minimum-like trend. However the crystallinity content of the sample developed in the cold mould at 35 °C is quite low. If we consider the semi-crystalline PLA as a particulate composite consisting in an amorphous matrix with

dispersed crystalline domains, we can consider that (Equation (5)):

$$\sigma_b = \sigma_{cryst} V_{cryst} + \sigma_{amor} V_{amor} \quad (5)$$

where σ_b is the measured stress at break of PLA and σ_{cryst}, V_{cryst}, σ_{amor} and V_{amor} are the stress at break and volume fractions of its crystalline and amorphous phases, respectively. We have to notice that Equation (5) represents a strong approximation, since $\sigma_{cryst} V_{cryst}$ is probably the sum of contributions of two different kinds of crystals: α and α′. In fact both kinds of crystals are present, as revealed by DSC analysis. However, as the material is mainly amorphous (in fact the crystallinity varies in the range 0.3–7.3%) in this case the mechanical properties strongly depend on the rigidity of the amorphous phase. In fact the elastic modulus of the amorphous phase, as well as the T_g value, decreases as the OLA8 content increases. This can easily explain the trend of E, σ_y and σ_b as a function of OLA8 content.

On the other hand E, σ_b and σ_y were found to increase with LAK content whereas the % Cryst. I crystallinity showed a maximum at about 3% LAK. The trend can be explained again keeping into account that mechanical properties are mainly consequence of the rigidity of the amorphous phase. In this case, we can consider the interaction of LAK or small LAK aggregates with PLA macromolecules, acting as physical cross-linking points, thus resulting in an increased modulus of the amorphous matrix. In accordance this can explain why E, σ_b and σ_y increase upon increasing LAK concentration.

4. Conclusions

The application of a Mixture Design approach allowed investigating the influence of plasticization and nucleation onto thermal behaviour and mechanical properties of PLA based materials in a systematic way, by clearly identifying composition regions where the crystallization rate is maximized and where a synergistic effect can be observed between plasticizer and nucleation agents, attributed to the optimization of balance between formation of nuclei rate and spherulitic growth rate. LAK resulted efficient as nucleating agent since the half time of crystallization of PLA in the blends with LAK and PDLA was significantly reduced.

Interestingly the crystallinity developed during injection moulding resulted maximized at intermediate LAK content with respect to the investigated range, whereas it presents a minimum-like trend as a function of OLA8 concentration. Hence the plasticizer, which was reported to favour in general crystal growth [32], is found here to disturb crystal growth in the early stage of crystal formation if present in intermediate concentration and to favour it if present at higher concentration.

However the mechanical properties were found to be mainly dependent on the amorphous phase rigidity of the PLA based compounds as the crystallinity content developed was low, in the range 0,3–7,3% in the experimented conditions. Hence E, σ_b and σ_y were found to increase as a function of LAK content increase and decrease as a function of OLA8 increase. The former trend was attributed to specific interaction between LAK and PLA macromolecules improving amorphous phase rigidity and the latter can be attributed to reduction of amorphous phase rigidity thanks to plasticization.

The technological exploitation of this study can occur by correctly modifying mould temperature (close to cold crystallization temperature) and holding time (it should be increased) in injection moulding to benefit of the improved crystallization rate in the composition range where a synergy between plasticization and nucleation was found. In the case of fast cooling below glass transition temperature (condition experimented in the present work) this study demonstrates that the developed crystallinity is quite low, but can be maximized by using intermediate concentration of LAK and a high content of OLA8, to find, even in these less favourable conditions for crystallization, the best compromise between the increase of nuclei density due to LAK and the increase of spherulite growth rate due to OLA8.

Acknowledgements

Authors acknowledge the financial support from the European Union's Seventh Framework Programme, DIBBIOPACK [Development of injection and extrusion blow moulded biodegradable and multifunctional packages by nanotechnologies GA: n° 280676.]

References

[1] Liu H., Zhang J.: Research progress in toughening modification of poly(lactic acid). Journal of Polymer Science Part B: Polymer Physics, **49**, 1051–1083 (2011). DOI: 10.1002/polb.22283

[2] Lim L-T., Auras R., Rubino M.: Processing technologies for poly(lactic acid). Progress in Polymer Science, **33**, 820–852 (2008). DOI: 10.1016/j.progpolymsci.2008.05.004

[3] Auras R., Harte B., Selke S.: An overview of polylactides as packaging materials. Macromolecular Bioscience, **4**, 835–864 (2004). DOI: 10.1002/mabi.200400043

[4] Saeidlou S., Huneault M. A., Li H., Park C. B.: Poly(lactic acid) crystallization. Progress in Polymer Science, **37**, 1657–1677 (2012). DOI: 10.1016/j.progpolymsci.2012.07.005

[5] Garlotta D.: A literature review of poly(lactic acid). Journal of Polymers and the Environment, **9**, 63–84 (2001). DOI: 10.1023/A:1020200822435

[6] Kister G., Cassanas G., Vert M.: Effects of morphology, conformation and configuration on the IR and Raman spectra of various poly(lactic acid)s. Polymer, **39**, 267–273 (1998). DOI: 10.1016/S0032-3861(97)00229-2

[7] Coltelli M-B., Bronco S., Chinea C.: The effect of free radical reactions on structure and properties of poly(lactic acid) (PLA) based blends. Polymer Degradation and Stability, **95**, 332–341 (2010). DOI: 10.1016/j.polymdegradstab.2009.11.015

[8] Nerkar M., Ramsay J. A., Ramsay B. A., Vasileiou A. A., Kontopoulou M.: Improvements in the melt and solid-state properties of poly(lactic acid), poly-3-hydroxyoctanoate and their blends through reactive modification. Polymer, **64**, 51–61 (2015). DOI: 10.1016/j.polymer.2015.03.015

[9] Raquez J-M., Habibi Y., Murariu M., Dubois P.: Polylactide (PLA)-based nanocomposites. Progress in Polymer Science, **38**, 1504–1542 (2013). DOI: 10.1016/j.progpolymsci.2013.05.014

[10] Kowalczyk M., Piorkowska E., Kulpinski P., Pracella M.: Mechanical and thermal properties of PLA composites with cellulose nanofibers and standard size fibers. Composites Part A: Applied Science and Manufacturing, **42**, 1509–1514 (2011). DOI: 10.1016/j.compositesa.2011.07.003

[11] Pluta M., Paul M-A., Alexandre M., Dubois P.: Plasticized polylactide/clay nanocomposites. I. The role of filler content and its surface organo-modification on the physico-chemical properties. Journal of Polymer Science Part B: Polymer Physics, **44**, 299–311 (2006). DOI: 10.1002/polb.20694

[12] Scatto M., Salmini E., Castiello S., Coltelli M-B., Conzatti L., Stagnaro P., Andreotti L., Bronco S.: Plasticized and nanofilled poly(lactic acid)-based cast films: Effect of plasticizer and organoclay on processability and final properties. Journal of Applied Polymer Science, **127**, 4947–4956 (2013). DOI: 10.1002/APP.38042

[13] Hassouna F., Raquez J-M., Addiego F., Dubois P., Toniazzo V., Ruch D.: New approach on the development of plasticized polylactide (PLA): Grafting of poly (ethylene glycol) (PEG) *via* reactive extrusion. European Polymer Journal, **47**, 2134–214 (2011). DOI: 10.1016/j.eurpolymj.2011.08.001

[14] Burgos N., Tolaguera D., Fiori S., Jimenez A.: Synthesis and characterization of lactic acid oligomers: Evaluation of performance as poly(lactic acid) plasticizers. Journal of Polymers and the Environment, **22**, 227–235 (2014). DOI: 10.1007/s10924-013-0628-5

[15] Burgos N., Martino V. P., Jiménez A.: Characterization and ageing study of poly(lactic acid) films plasticized with oligomeric lactic acid. Polymer Degradation and Stability, **98**, 651–658 (2013). DOI: 10.1016/j.polymdegradstab.2012.11.009

[16] Coltelli M-B., Della Maggiore I., Bertoldo M., Bronco S., Signori F., Ciardelli F.: Poly(lactic acid) properties as a consequence of poly(butylene adipate-*co*-terephthalate) blending and acetyl tributyl citrate plasticization. Journal of Applied Polymer Science, **110**, 1250–1262 (2008). DOI: 10.1002/app.28512

[17] Quero E., Müller A. J., Signori F., Coltelli M-B., Bronco S.: Isothermal cold-crystallization of PLA/PBAT blends with and without the addition of acetyl tributyl citrate. Macromolecular Chemistry and Physics, **213**, 36–48 (2012). DOI: 10.1002/macp.201100437

[18] Nagarajan V., Zhang K., Misra M., Mohanty A. K.: Overcoming the fundamental challenges in improving the impact strength and crystallinity of PLA biocomposites: Influence of nucleating agent and mold temperature. ACS Applied Material Interfaces, **7**, 11203–11214 (2015). DOI: 10.1021/acsami.5b01145

[19] Wang L., Wang Y-N., Huang Z-G., Weng Y-X.: Heat resistance, crystallization behavior, and mechanical properties of polylactide/nucleating agent composites. Materials and Design, **66**, 7–15 (2015). DOI: 10.1016/j.matdes.2014.10.011

[20] Guo X., Liu H., Zhang J., Huang J.: Effects of polyoxymethylene as a polymeric nucleating agent on the isothermal crystallization and visible transmittance of poly(lactic acid). Industrial and Engineering Chemistry Research, **53**, 16754–16762 (2014). DOI: 10.1021/ie502104y

[21] Penco M., Spagnoli G., Peroni I., Rahman W. A., Frediani M., Oberhauser W., Lazzeri A.: Effect of nucleating agents on the molar mass distribution and its correlation with the isothermal crystallization behavior of poly (L-lactic acid). Journal of Applied Polymer Science, **122**, 3528–3536 (2011).
DOI: 10.1002/app.34761

[22] Nam J. Y., Okamoto M., Okamoto H., Nakano M., Usuki A., Matsuda M.: Morphology and crystallization kinetics in a mixture of low-molecular weight aliphatic amide and polylactide. Polymer, **47**, 1340–1347 (2006).
DOI: 10.1016/j.polymer.2005.12.066

[23] Ma P., Xu Y., Wang D., Dong W., Chen M.: Rapid crystallization of poly(lactic acid) by using tailor-made oxalamide derivatives as novel soluble-type nucleating agents. Industrial and Engineering Chemistry Research, **53**, 12888–12892 (2014).
DOI: 10.1021/ie502211j

[24] Battegazzore D., Bocchini S., Frache A.: Crystallization kinetics of poly(lactic acid)-talc composites. Express Polymer Letters, **5**, 849–858 (2011).
DOI: 10.3144/expresspolymlett.2011.84

[25] Ouchiar S., Stoclet G., Cabaret C., Georges E., Smith A., Martias C., Addad A., Gloaguen V.: Comparison of the influence of talc and kaolinite as inorganic fillers on morphology, structure and thermomechanical properties of polylactide based composites. Applied Clay Science, **116–117**, 231–240 (2015).
DOI: 10.1016/j.clay.2015.03.020

[26] Blaker J. J., Lee K-Y., Walters M., Drouet M., Bismarck A.: Aligned unidirectional PLA/bacterial cellulose nanocomposite fibre reinforced PDLLA composites. Reactive and Functional Polymers, **85**, 185–192 (2014).
DOI: 10.1016/j.reactfunctpolym.2014.09.006

[27] Chen C., He B-X., Wang S-L., Yuan G-P., Zhang L.: Unexpected observation of highly thermostable transcrystallinity of poly(lactic acid) induced by aligned carbon nanotubes. European Polymer Journal, **63**, 177–185 (2015).
DOI: 10.1016/j.eurpolymj.2014.12.012

[28] Liang Y-Y., Yang S., Jiang X., Zhong G-J., Xu J-Z., Li Z-M.: Nucleation ability of thermally reduced graphene oxide for polylactide: Role of size and structural integrity. The Journal of Physical Chemistry B, **119**, 4777–4787 (2015).
DOI: 10.1021/jp511742b

[29] Pluta M.: Morphology and properties of polylactide modified by thermal treatment, filling with layered silicates and plasticization. Polymer, **45**, 8239–8251 (2004).
DOI: 10.1016/j.polymer.2004.09.057

[30] Xiao H., Yang L., Ren X., Jiang T., Yeh J. T.: Kinetics and crystal structure of poly(lactic acid) crystallized nonisothermally: Effect of plasticizer and nucleating agent. Polymer Composites, **31**, 2057–2068 (2010).
DOI: 10.1002/pc.21004

[31] You J., Yu W., Zhou C.: Accelerated crystallization of poly(lactic acid): Synergistic effect of poly(ethylene glycol), dibenzylidene sorbitol, and long-chain branching. Industrial and Engineering Chemistry Research, **53**, 1097–1107 (2014).
DOI: 10.1021/ie402358h

[32] Yu L., Liu H., Dean K., Chen L.: Cold crystallization and postmelting crystallization of PLA plasticized by compressed carbon dioxide. Journal of Polymer Science Part B: Polymer Physics, **46**, 2630–2636 (2008).
DOI: 10.1002/polb.21599

[33] Li H., Huneault M. A.: Effect of nucleation and plasticization on the crystallization of poly(lactic acid). Polymer, **48**, 6855–6866 (2007).
DOI: 10.1016/j.polymer.2007.09.020

[34] Anderson K. A., Randall J. R., Kolstad J. J.: Polylactide molding compositions and molding process. Nature Word Patent, WO 2011085058 A1 (2011).

[35] Wei X-F., Bao R-Y., Cao Z-Q., Zhang L-Q., Liu Z-Y., Yang W., Xie B-H., Yang M-B.: Greatly accelerated crystallization of poly(lactic acid): Cooperative effect of stereocomplex crystallites and polyethylene glycol. Colloid and Polymer Science, **292**, 163–172 (2014).
DOI: 10.1007/s00396-013-3067-x

[36] Tsuji H., Ikada Y.: Stereocomplex formation between enantiomeric poly(lactic acid)s. XI. Mechanical properties and morphology of solution-cast films. Polymer, **40**, 6699–6708 (1999).
DOI: 10.1016/S0032-3861(99)00004-X

[37] Lopez-Rodrıguez N., de Arenaza I. M., Meaurio E., Sarasua J. R.: Improvement of toughness by stereocomplex crystal formation in optically pure polylactides of high molecular weight. Journal of the Mechanical Behavior of Biomedical Materials, **37**, 219–225 (2014).
DOI: 10.1016/j.jmbbm.2014.05.022

[38] Shi X., Zhang G., Phuong T. V., Lazzeri A.: Synergistic effects of nucleating agents and plasticizers on the crystallization behavior of poly(lactic acid). Molecules, **20**, 1579–1593 (2015).
DOI: 10.3390/molecules20011579

[39] Eriksson L., Johansson E., Kettaneh-Wold N., Wikström C., Wold S.: Design of experiments, principle and applications. Umetrics Academy, Stockholm (2008).

[40] Montgomery D. C.: Design and analysis of experiments. Wiley, New York (2001).

[41] Tee Y. B., Talib R. A., Abdan K., Chin N. L., Basha R. K., Yunos K. F. M.: Thermally grafting aminosilane onro kenaf-derived cellulose and its influence on the thermal properties of poly(lactic acid) composites. BioResources, **8**, 4468–4483 (2013).

[42] Scheffé H.: Experiments with mixtures. Journal of the Royal Statistical Society, 20, 344-360 (1958).

[43] Akalin O., Akay K. U., Sennaroglu B., Tez M.: Optimization of chemical admixture for concrete on mortar performance tests using mixture experiments. Chemometrics and Intelligent Laboratory Systems, **104**, 233–242 (2010).
DOI: 10.1016/j.chemolab.2010.08.013

[44] Nam B. U., Lee B. S., Kim M. H., Hong C. H.: Effect of a nucleating agent on crystallization behavior and mechanical property of PLA stereocomplex. in 'ICCM18 proceedings, Jeju, Korea' p.4 (2011).

[45] Nam B-U., Lee B-S.: Toughening of PLA stereocomplex by impact modifiers. Journal of the Korea Academia-Industrial Cooperation Society, **13**, 919–925 (2012).
DOI: 10.5762/KAIS.2012.13.2.919

[46] Jing Z., Shi X., Zhang G., Li J.: Rheology and crystallization behavior of PLLA/TiO_2-g-PDLA composites. Polymers for Advanced Technologies, **26**, 528–537 (2015).
DOI: 10.1002/pat.3485

[47] Phuphuak Y., Miao Y., Zinck P., Chirachanchai S.: Balancing crystalline and amorphous domains in PLA through star-structured polylactides with dual plasticizer/nucleating agent functionality. Polymer, **54**, 7058–7070 (2013).
DOI: 10.1016/j.polymer.2013.10.006

eXPRESS Polymer Letters Vol.10, No.4 (2016) 289–301
Available online at www.expresspolymlett.com
DOI: 10.3144/expresspolymlett.2016.27

Effects of UV-accelerated weathering and natural weathering conditions on anti-fungal efficacy of wood/PVC composites doped with propylene glycol-based HPQM

P. Srimalanon[1], *W. Yamsaengsung*[2], *A. Kositchaiyong*[1], *E. Wimolmala*[1], *K. Isarangkura*[3], *N. Sombatsompop*[1*]

[1]Polymer PROcessing and Flow (P-PROF) Research Group, Division of Materials Technology, School of Energy, Environment and Materials, King Mongkut's University of Technology Thonburi (KMUTT), 126 Pracha-utid Rd., Bangmod, Thungkru, 10140 Bangkok, Thailand
[2]School of Science and Technology, Sukhothai Thammathirat Open University, 9/9 Moo 9, Bangpood, Pakkret, 11120 Nonthaburi, Thailand
[3]Koventure Co., Ltd., 563 Moo 4, Bangpoo Industrial Estate Soi 10, Sukhumvit Rd., Praeksa, Muang, 10280 Samut Prakan, Thailand

Received 21 August 2015; accepted in revised form 20 October 2015

Abstract. This work studied the mechanical, physical and weathering properties and anti-fungal efficacy of polyvinyl chloride(PVC) and wood flour/polyvinyl chloride composites(WPVC). 2-hydroxypropyl-3-piperazinyl-quinoline carboxylic acid methacrylate (HPQM) in propylene glycol was used as an anti-fungal agent. Propylene glycol-based HPQM was doped in neat PVC and in WPVC containing 50 and 100 pph wood (WPVC-50 and WPVC-100). The flexural properties of PVC decreased when propylene glycol-based HPQM was added. However, adding this component did not affect the flexural properties of WPVC. Fungal growth inhibition test and dry weight technique were used for evaluation of anti-fungal effectiveness. *Aspergillus niger* was used as a testing fungus. Adding propylene glycol-based HPQM to WPVC-100 led to the most effective anti-fungal performance. Wood flour acted as an anti-fungal promoter for the WPVC composites. The optimal dosages of propylene glycol-based HPQM in PVC, WPVC-50, and WPVC-100 were 50 000, 15 000, and 10 000 ppm, respectively. UV-accelerated weathering aging and natural weathering conditions were found to affect the flexural properties of PVC and WPVC. The change in the anti-microbial performance of WPVC under natural weathering were slower than those under UV-accelerated weathering aging. The anti-microbial evaluation indicated that the samples doped with less than 20 000 ppm propylene glycol-based HPQM had a more pronounced effect than the ones doped with higher dosages.

Keywords: *polymer composites, wood flour, anti-fungal activities, mechanical properties, environmental degradation*

1. Introduction

Wood/polyvinyl chloride composites (WPVC) can be converted into numerous products for specific applications, such as in the construction and automotive industries, and are widely used due to their desirable properties including cost-effectiveness and easy customization [1, 2]. For outdoor applications, various additives, e.g. stabilizers, reinforcing fillers, and biocides, must be added to WPVC in order to prevent the degradation of the composites [3–11].

Pilarski and Matuana [1] observed a decrease in flexural properties of WPVC due to the accelerated aging effect of freeze-thaw cycles and found that the aging leads to more moisture uptake in the composites, resulting in some deterioration of interfacial adhesion between the wood flour and the PVC matrix.

*Corresponding author, e-mail: narongrit.som@kmutt.ac.th

Naumann *et al*. [10] and Dawson-Andoh *et al*. [4] reported the occurrence of surface micro- and macro-cracks in wood composite materials due to the accelerated weathering aging effect. The results suggest that the accelerated weathering aging effect under UV radiation, water spray, and repeated freeze-thaw cycles causes enhancement of moisture sorption and microbial attacks. According to studies on biological attack on materials, colonization by a variety of fungal species (wood-decay fungi, staining fungi, yeasts, and yeast-like fungi) has been mostly found on the surfaces of materials [4, 12–16]. Gumargalieva *et al*. [3] reported that *Aspergillus niger*, a degradative fungal species, colonizes the surfaces of plasticized-PVC (p-PVC), causing losses of plasticizer. Kaczmarek and Bajer [17] reported that the biodegradation process was significantly more accelerated in p-WPVC as compared with p-PVC when exposed to soil burial conditions, i.e. in forest soil and in soil enriched with microorganisms.

Typically, commercial biocides can be divided into two types: inorganic and organic. Inorganic biocides, which are derived from a chemical reaction process, are generally considered to have high thermal stability; while organic biocides, usually made from plant parts or produced by biochemical processes of living organisms, are normally subject to biodegradation in outdoor environments. Coulthwaite *et al* [18] reported 2-n-octyl-4-isothiazolin-3-one (OIT) encapsulated on silica or zeolite and showed the best long term anti-fungal performance of pPVC materials. Kositchaiyong *et al*. [19] reported that addition of anti-fungal agent (Carbendazim or IPBC) in WPVC composites tended to increase the anti-fungal (*Aspergillus niger*) efficacy. 2-Hydroxypropyl-3-piperazinyl-quinoline carboxylic acid methacrylate (HPQM), or BioCleanAct™ (product code BCA-101A0; Micro Science Tech Co., Ltd., Hwaseong, South Korea), is a new commercial anti-microbial agent that is claimed to be an environmental friendly organic biocide with low toxicity, light elution, and excellent color stability under UV light and pyrolysis conditions. Evidence [20, 21] shows that HPQM performs well against a broad range of the microbial spectrum. Kawahara *et al*. [22] reported that HPQM has an anti-microbial effect against both gram-negative (e.g., *Escherichia coli, Pseudomonas aeruginosa*, and *Salmonella typhimurium*) and gram-positive (e.g., *Staphylococcus aureus*, *Bacillus subtilis*, and *Streptococcus aureus*) bacteria.

Thus, the objective of this work was to study the effects of UV-accelerated weathering aging and natural weathering conditions on the mechanical and physical properties and the anti-fungal efficacy of polyvinyl chloride (PVC) and wood/polyvinyl chloride (WPVC) composites containing propylene glycol-based HPQM (as an anti-microbial agent). Propylene glycol-based HPQM with content ranging from 0 to 50 000 ppm was doped in PVC and in WPVC with wood flour content of 50 and 100 pph (WPVC-50 and WPVC-100). Fungal growth inhibition test and dry weight technique, using *Aspergillus niger* as a testing fungus, were employed to evaluate anti-fungal performance.

2. Experimental

2.1. Materials and chemicals

Suspension PVC with a *K* value of 58 (Siamvic 258RB; Vinythai Public Co., Ltd., Rayong, Thailand), necessary additives, and wood flour from hardwood (V.P. Wood Co., Ltd., Bangkok, Thailand) were used in this work. The PVC and necessary additives were manufactured following the formulations given in our previous study [7]. Wood flour with an average particle size of 100 to 300 μm was chemically treated with *N*-2(aminoethyl)-3-aminopropyl trimethoxysilane (KBM-603; Shin-Etsu Chemical Co., Ltd., Tokyo, Japan) as a coupling agent. Propylene glycol-based HPQM (HPQM), in the form of a light yellow liquid, was used as an anti-fungal agent (Koventure Co., Ltd., Samut Prakan, Thailand), with the chemical formulation of 2-hydroxypropyl-3-piperazinyl-quinoline carboxylic acid methacrylate thiazole,

Table 1. Ingredients in PVC and WPVC compounds

Chemical name	Content [pph*]
Suspension PVC (Siamvic 258RB)	100.0
Emulsion PVC (Siamvic 167GZ)	4.0
Thermal stabilizer (Pb–Ba-based organic, PF 608A)	3.6
Thermal stabilizer (PF 601)	1.5
External lubricant (Finalux-G 741)	0.6
Internal lubricant (calcium stearate)	0.6
Filler (calcium carbonate, Omyacarb® 2T)	12.0
Impact modifier (modified chlorinated polyethylene)	7.7
Processing aid (acrylic, PA-20)	6.0
Wood flour	0, 50, 100
Silane coupling agent (KBM-603)	1 wt% of wood
Anti-microbial agent (propylene glycol-based HPQM)	0–50000 ppm**

*pph: parts per hundred; **ppm: parts per million

freezing point of –59 °C and boiling point of 188 °C. *Aspergillus niger* was used as a testing fungus (*A. niger*, TISTR 3245; Thailand Institute of Scientific and Technological Research, Thailand). Necessary additives included thermal stabilizers, external and internal lubricants, calcium carbonate as a filler, modified chlorinated polyethylene as an impact modifier, and an acrylic polymer as a processing aid (Table 1).

2.2. Sample preparation

The wood flour was chemically surface-treated with *N*-2(aminoethyl)-3-aminopropyl trimethoxysilane at 1.0 wt% of wood flour content using a high-speed mixer at 1000 rpm for 5 min. Treated wood flour was then dried in a hot-air oven at 80 °C for 72 h [7]. The PVC compound was dry-blended with treated wood flour and HPQM using a high-speed mixer at 1000 rpm for 5 min. The components of PVC and WPVC, including the necessary additives, are listed in Table 1. HPQM at a content of 0, 1000, 5000, 10 000, 15 000, 20 000, and 50 000 ppm of PVC compound was doped in PVC and in WPVC containing wood flour at 50 and 100 pph of PVC compound (WPVC-50 and WPVC-100). All compositions were melt-blended using a counter-rotating twin-screw extruder (HAAKE™ Rheomex CTW 100 QC; Thermo Scientific, Waltham, MA, USA) at temperatures of 140, 150, 160 and 160 °C for feed zone to die, respectively. A screw speed of 40 rpm was used to produce pellets of PVC, WPVC-50, and WPVC-100 with different HPQM contents; the pellets were then dried in a hot-air oven at 80 °C for 24 h to remove moisture. Test specimen pellets were prepared using a compression molding machine (LP-20M; Labtech Engineering, Samut Songkhram, Thailand) at 170 °C under a pressure of 150 kg/cm^2 for 8 min.

2.3. Material characterizations

2.3.1. Flexural properties

Flexural properties were measured following the standard test method ASTM D790 (2010), using a universal testing machine (Autograph AG-I; Shimadzu, Kyoto, Japan). The flexural properties of specimens were investigated in terms of flexural modulus and strength. The results were averaged from at least five independent determinations.

2.3.2. Surface contact angle measurement

Surface contact angle value was determined following ASTM D7334 (2008) using a contact angle goniometer (100-00; Ramé-hart Instrument Co., Succasunna, NJ, USA). Surface contact angle value referred to changes of surface chemistry, surface energy, and hydrophobicity of PVC and WPVC. The results were averaged from at least five independent droplets at 100 µL/time of dropped volume size in advancing stage using distilled water as wetting liquid.

2.3.3. Surface morphology

The morphological properties of PVC and WPVC were photographed using a scanning electron microscope (JSM-6301F; JEOL, Tokyo, Japan) under 15 kV of accelerating voltage and backscattering detection mode. The aim of the tests was to study the fracture surface of specimens before and after weathering testing. For specimen preparation, all samples were dried, cleaned, and then gold-coated using a sputter coater before being photographed.

2.3.4. Surface color change

Surface color change of the specimens was measured with a UV-Vis-NIR recording spectrophotometer (UV-3100; Shimadzu, Japan) in accordance with ASTM D1746 (2009), using the Hunter Lab system. The surface color change of specimens was investigated in terms of lightness level (L^*). The results were averaged from at least five independent determinations.

2.4. Evaluation of fungal growth

2.4.1. Fungal growth inhibition test

Fungal growth inhibition [19] against *A. niger*, a testing fungus, was used for anti-fungal evaluation of specimens. The procedure was commenced by preparing an initial fungal spore suspension containing 10^4 spores/mL in 100 mL of 1:1 potato dextrose broth (PDB)/potato dextrose agar (PDA). One piece of specimen (30×30 cm^2) was placed on PDA in a Petri dish (9 cm diameter). Prepared fungal spores were then poured onto the specimen in the dish and incubated at a temperature of 25 °C for 7 days. The results were reported as percent of fungal growth inhibition, as shown in Equation (1):

$$\text{Percent of fungal growth inhibition} = \frac{A_C}{A_S} \cdot 100 \quad (1)$$

where A_C and A_S are the area of fungal growth inhibition on the specimen surface [mm] and the area of the specimen surface [mm], respectively. Each area was calculated using the ImageJ program.

2.4.2. Dry weight technique

The technique was modified from the determination of fungal growth as described in previous studies [23, 24]. The procedure was commenced by preparing an initial fungal spore suspension containing 10^4 spores/mL in 100 mL PDB. Two pieces of specimens (2.5×5 cm^2) were placed into the prepared fungal medium in an Erlenmeyer flask and then shaken at 150 rpm at an incubation temperature of 25 °C for 14 days. After the incubation period, the specimens were collected from the PDB medium and the growing fungi removed by vacuum filtration using high wet-strength Whatman No. 1 filter paper. The filtered fungi were oven-dried at 80 °C for 48 h and then cooled in a desiccator until reaching a constant weight. The weight of growing fungi was calculated by subtracting the weight of the filter paper from the total weight, and was reported in terms of dry weight of fungi in mg/L, as governed by Equation (2):

$$\text{Dry weight of fungi} = \frac{W_d}{V_m} \quad (2)$$

where W_d is the dry weight of filtered fungi [mg] and V_m is the volume of the PDB medium used (100 mL).

2.5. Accelerated weathering studies

2.5.1. UV-accelerated weathering aging testing

Testing was performed following ASTM G154 (2012) cycle I using a QUV Accelerated Weathering Tester (Q-LAB, Westlake, OH, USA). The conditions of UV-weathering aging testing included exposure to UVA radiation at a wavelength of 340 nm and intensity of 0.77 W/m^2 at 60 °C for 8 h, and water condensation at 50 °C for 4 h. The aging times were varied at 0, 4, 8, 16, and 32 days.

2.5.2. Natural weathering testing

Testing was performed in accordance with ASTM D1435 (2005). The specimens were exposed on racks at a 45° angle in a southerly direction on a roof deck at the School of Energy, Environment and Materials building at King Mongkut's University of Technology Thonburi, Bangkok, Thailand, for 52 days during March and April 2014. The conditions for natural weathering testing included UVA radiation at a wavelength of 340 nm and intensity of 0.67 W/m^2 tested by spectroradiometer series CAS140CT-154 (approved by the National Institute of Metrology of Thailand), temperature 26.7 to 36.9 °C, rainfall 23.7 mL/day, and relative humidity 72.5%. Climate data were provided by National Institute of Metrology of Thailand and The Thai Meteorological Department. The natural weathering times were varied at 0, 14, 28, 42, and 56 days.

3. Results and discussion

3.1. Effects of HPQM and wood flour contents

The results of the fungal growth inhibition test and the dry weight technique against *A. niger* for PVC, WPVC-50, and WPVC-100 with different HPQM contents are shown in Figure 1. In general, a greater percentage of fungal growth inhibition usually indicates better anti-microbial efficacy of a material. Figure 1a shows the anti-microbial efficacy in terms of percent of fungal growth inhibition against *A. niger* of PVC at 0, 50, and 100 pph of wood flour doped with HPQM. The minimum HPQM contents to attain 100% fungal growth inhibition for PVC, WPVC-50, and WPVC-100 were 50 000, 15 000, and 10 000 ppm, respectively. It was found that the anti-fungal efficacy of PVC increased with increasing HPQM and wood flour contents. This suggests that the wood flour allows more HPQM to migrate onto the WPVC composite surfaces. An explanation for this phenomenon is that introducing the wood flour, which is highly hydrophilic in nature [25, 26] into the WPVC makes the PVC become more hydrophilic. As a consequence, more water molecules can be absorbed into/onto the HPQM/WPVC surfaces [19]. Another possible reason was that the methoxy groups ($–OCH_3$) in the aminosilane could be hydrolyzed to produce silanol [$–OSi(OH)_3$] and these silanol groups would develop covalent siloxane bonds by reaction with OH groups of wood during the wood flour pretreatment process, and then the PVC could bond with the amine group of aminosilane modified wood flour by an acid–base interaction [27–29]. Accordingly, wood flour acts as an anti-fungal promoter for the WPVC due to its preliminary treatment with amino-based silane coupling agent which reduces the degree of water absorption [30].

Figure 1b shows the anti-fungal efficacy in terms of dry weight against *A. niger* of PVC at 0, 50, and 100 pph of wood flour doped with HPQM. In general, the lower the dry weight of the fungus, the better

the anti-fungal efficacy of the material. In this case, the dry weight of *A. niger* (Figure 1b) decreased with increasing wood flour and HPQM contents. This suggests that wood flour acts as an anti-fungal promoter for WPVC [31]. This property was clearly seen for wood flour contents of 50 and 100 pph. The findings also correspond well to the percent of fungal growth inhibition results shown in Figure 1a.

Table 2 shows the surface contact angle values of PVC and WPVC with different HPQM and wood flour contents. It was observed that adding HPQM tended to lower the surface contact angle values of PVC and WPVC materials. This implies greater hydrophilicity of the PVC and WPVC when HPQM was introduced into the composites due to the high polarity and hydrophilicity of HPQM, which probably migrated onto the PVC and WPVC surfaces. It was also found that the higher the wood flour content, the lower the surface contact angle values. This would be associated with the hydrophilicity of the wood flour in WPVC composites, with high water absorption and polarity. The changes in the hydrophilicity of WPVC by adding wood flour are related to the increase in the number of hydroxyl groups in the wood fiber structure.

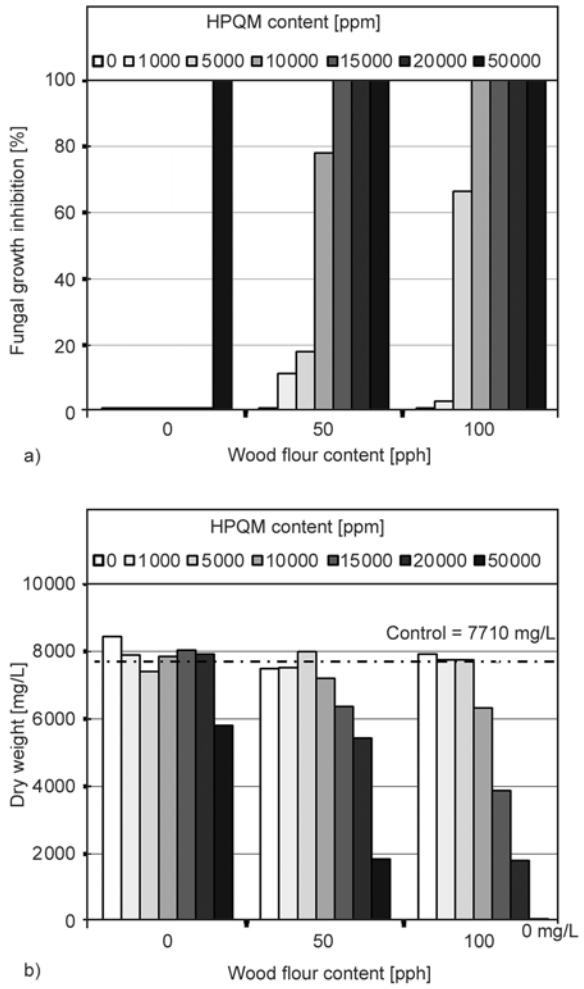

Figure 1. Anti-fungal efficacy of PVC, WPVC-50, and WPVC-100 with different HPQM content: (a) fungal growth inhibition values, and (b) dry weight values

3.2. Effects of QUV-accelerated weathering aging and natural weathering conditions

Anti-fungal efficacy and surface morphology of the PVC and WPVC specimens from the effects of QUV-accelerated weathering are shown in Figures 2 and 3 with respect to the degree of fungal growth inhibition (quantitative analysis) and the results of scanning electron micrographs (SEM) (qualitative analysis), respectively. Figure 2a shows the anti-fungal efficacy in terms of fungal growth inhibition for neat PVC with varying HPQM content under the effect of QUV-accelerated weathering. The degree of fungal growth inhibition for the PVC samples decreased significantly with increasing QUV aging time. The water condensation process accompanying the degradation of the neat PVC during QUV aging could be the main reason for this drastic reduction in the anti-fungal activity of PVC samples. When the PVC samples encountered UV light, some cracks would occur due to PVC degradation. The HPQM was thus able to migrate more easily, or be released through the cracks, and was eventually washed away in the water condensation process during QUV aging. The number of cracks for neat PVC increased with increasing aging time (Figure 3a–3c). These results correspond well with Sributr *et al*. [32]. The findings indicate that HPQM in neat PVC was not capable of maintaining anti-fungal efficacy under prolonged UV light exposure.

Table 2. Contact angles of PVC, WPVC-50, and WPVC-100 with different HPQM content. Mean (±SD).

Wood flour content [pph]	HPQM content [ppm]						
	0	**1000**	**5000**	**10 000**	**15 000**	**20 000**	**50 000**
0	90.9° (±0.7)	88.3° (±0.3)	88.5° (±0.9)	86.8° (±0.5)	84.9° (±1.0)	80.8° (±1.2)	72.9° (±2.2)
50	81.6° (±2.1)	80.6° (±1.6)	80.1° (±1.8)	79.2° (±1.5)	77.9° (±1.0)	75.3° (±0.5)	70.5° (±1.8)
100	78.2° (±1.0)	77.8° (±1.1)	77.3° (±2.0)	74.1° (±0.2)	73.6° (±0.3)	73.4° (±0.2)	66.7° (±0.1)

Figure 2b shows the anti-fungal efficacy in terms of fungal growth inhibition for WPVC-50 with varying HPQM content under the effect of QUV-accelerated weathering. From day 0 to day 8, it was observed that the degree of fungal growth inhibition for the WPVC-50 sample with HPQM content of 5000 ppm increased with increasing QUV aging time. Then, from day 8 to day 32 the degree of fungal growth inhibition for the WPVC-50 sample decreased with increasing QUV aging time. During the first few days of aging, the low anti-fungal efficacy of WPVC-50 was caused by HPQM being trapped by the PVC matrix, thus limiting the diffusion rate of HPQM in the composites. The limited diffusion rate of HPQM may be caused by both H-bonding between HPQM and the coupling agent and dipole–dipole interaction between HPQM and carbon atoms in the PVC matrix. The decrease in the degree of fungal growth inhibition for the WPVC-50 sample after day 8 involved the water condensation process accompanying the degradation of the WPVC-50 during QUV aging, which initiated some cracks on the WPVC-50 composite, thereby increasing the diffusion rate of HPQM through the cracks. The number of cracks for WPVC-50 increased with increasing aging time, as shown in Figure 3d–3f. These results correspond well with Sributr *et al*. [32]. During the condensation process, some of the HPQM was washed away from the composite samples, resulting in a decrease in anti-fungal growth inhibition, as shown in Figure 2b. Similar results, but with more pronounced anti-fungal efficacy, were shown for WPVC-100 with varying HPQM content under the effect of QUV-accelerated weathering (Figure 2c); the surface morphological properties illustrating the results are shown in Figure 3g–3i.

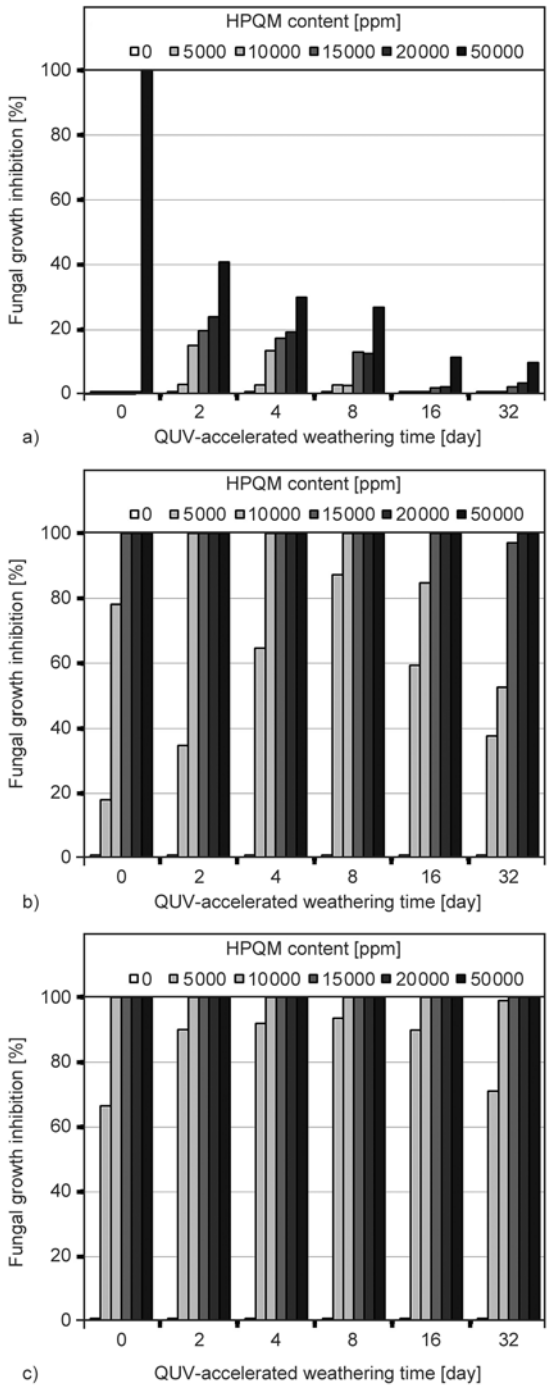

Figure 2. Fungal growth inhibition values for (a) PVC, (b) WPVC-50, and (c) WPVC-100 with different HPQM content, after QUV-accelerated weathering aging

Figures 4 and 5 show the effects of natural weathering conditions on the anti-fungal efficacy and surface morphology (from SEM) of neat PVC and of WPVC-50 and WPVC-100 composites with varying HPQM content. Figure 4a shows the effects of natural weathering conditions on the anti-fungal efficacy of neat PVC with varying HPQM content. Before natural weathering, the anti-fungal efficacy of neat PVC with 50 000 ppm HPQM reached 100% of fungal growth inhibition. Under natural weathering, the anti-fungal efficacy of PVC was generally found to decrease with increasing weathering time. This can be explained by the water condensation process accompanying the degradation of the neat PVC, as mentioned previously. However, at day 56 neat PVC regained some of its anti-fungal efficacy, from 20 to around 48%. In this case, when the PVC samples were exposed to UV light, some cracks would occur due to PVC degradation (Figure 5c). The HPQM was then able to migrate more easily (or be released through the cracks), thus increasing the anti-fungal efficacy of neat PVC.

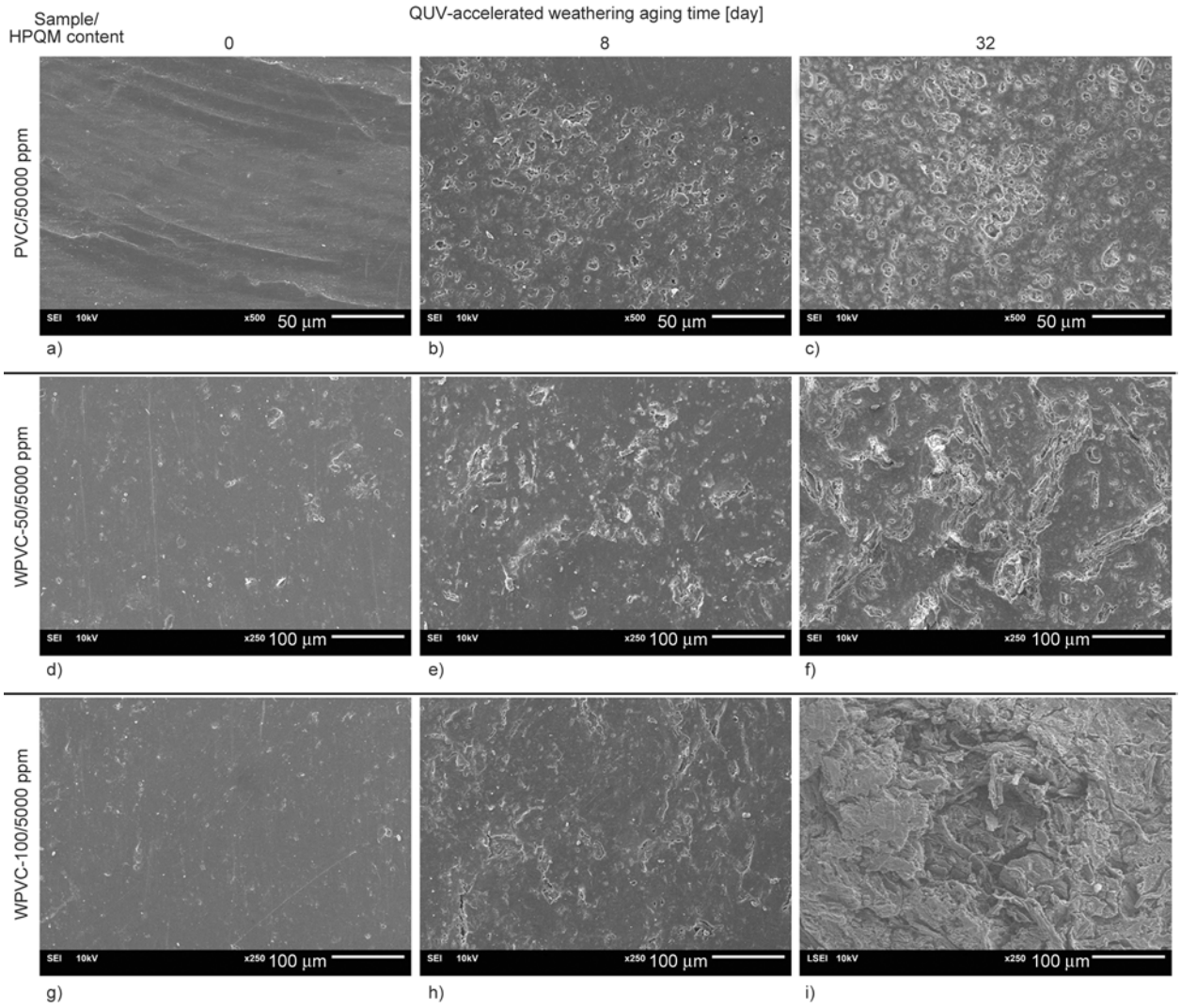

Figure 3. Scanning electron micrographs showing the surface morphology of PVC (a–c), WPVC-50 (d–e), and WPVC-100 (g–i) doped with HPQM, after QUV-accelerated weathering aging

Figure 4b shows the effects of natural weathering conditions on the anti-fungal efficacy of WPVC-50 with varying HPQM content. Before natural weathering, the minimum concentration of HPQM which resulted in 100% of fungal growth inhibition was 15 000 ppm. Under natural weathering, the anti-fungal efficacy of WPVC-50 was found to decrease with increasing weathering time for any given HPQM content (other than 50 000 ppm) until day 56, when the anti-fungal efficacy of WPVC-50 increased. As in the case of neat PVC, when the WPVC-50 samples encountered UV light, some cracks would occur due to WPVC-50 degradation (Figure 5d–5f), allowing the HPQM to migrate more easily (or be released through the cracks) and thus increase the anti-fungal efficacy of WPVC-50.

Figure 4c shows the effects of natural weathering conditions on the anti-fungal efficacy of WPVC-100 with varying HPQM content. Before natural weathering, the minimum concentration of HPQH necessary to achieve 100% of fungal growth inhibition was 10 000 ppm. Under natural weathering, the anti-fungal efficacy of WPVC-100 was found to decrease with increasing weathering time and then increase at day 56. Figure 5g–5i shows the surface morphology during natural weathering of WPVC-100 doped with 10 000 ppm HPQM. When comparing between QUV weathering (Figure 2) and natural weathering (Figure 4), the reduction of anti-fungal efficacy for neat PVC and WPVC was more pronounced for QUV weathering. It is known that radiation from sunlight under natural weathering conditions includes visible light, UV, and infrared radiation; whereas the radiation from a UVB lamp under QUV weathering conditions contains only UV radiation (280–380 nm) [33]. In general, radiation at UV

wavelengths is primarily responsible for PVC degradation. In this case, UV radiation under natural weathering was much lower than under QUV weathering. This is the reason for greater PVC and WPVC degradation under QUV weathering as compared with natural weathering.

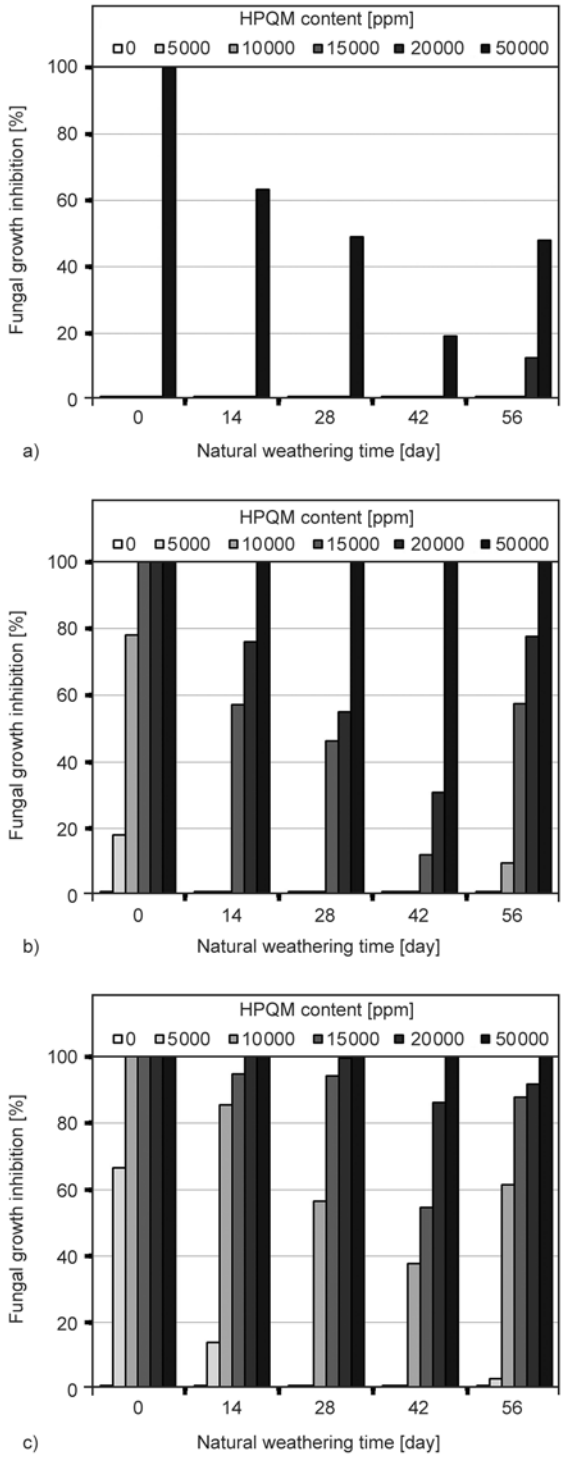

Figure 4. Fungal growth inhibition values for (a) PVC, (b) WPVC-50, and (c) WPVC-100 with different HPQM content, after natural weathering

Figure 6 shows the release behavior model of HPQM in the WPVC matrix when exposed to QUV-accelerated weathering aging and natural weathering. The release behavior of HPQM is composed of four stages: I) initial stage, II) water discharge, III) surface cracks, and IV) more surface cracks with respect to time or severity of QUV-accelerated weathering aging. Figure 6a shows stage I of the WPVC matrix, before applying weathering aging. This stage shows three types of HPQM activity on the WPVC composites: 1) forming H-bonds with the silane coupling agent, 2) forming dipole–dipole interaction with carbon atoms in the WPVC matrix, and 3) releasing HPQM species on the WPVC surface. Figure 6b shows stage II, the water-discharge stage, of the release behavior of HPQM in the WPVC matrix. In this stage, the degree of fungal growth inhibition for the WPVC decreased with increasing weathering time. This is because only the free HPQM on the top surface could achieve anti-fungal efficacy. Most of the HPQM was trapped by the PVC matrix. Figure 6c shows stage III, surface cracks, of the release behavior of HPQM in the WPVC matrix. In this stage, the degree of fungal growth inhibition for the WPVC increased with increasing weathering time. This is because the water condensation process accompanying the degradation of the WPVC generated some cracks; this allowed HPQM to migrate more easily, or be released through the cracks, and eventually be washed away in the water condensation process during QUV aging. In general, HPQM is replaced by water molecules, forming H-bonds with the OH– groups of the wood flour. Figure 6d shows stage IV, more surface cracks from the release behavior of HPQM in the WPVC matrix. In this stage, the degree of fungal growth inhibition for the WPVC decreased with increasing weathering time. This is because less HPQM is left in the WPVC.

Figure 7 shows the timeline of the release behavior of HPQM in the WPVC matrix when exposed to QUV-accelerated weathering aging and natural weathering. Natural weathering occurs in three stages: (I) initialization, (II) water-discharge, and (III) surface cracks. However, for QUV-accelerated weathering aging, there are four stages: (I) initialization, (II) water-discharge, (III) surface cracks, and (IV) more surface cracks. Both natural weathering and QUV-accelerated weathering aging had similar effects on the anti-microbial performance changes for

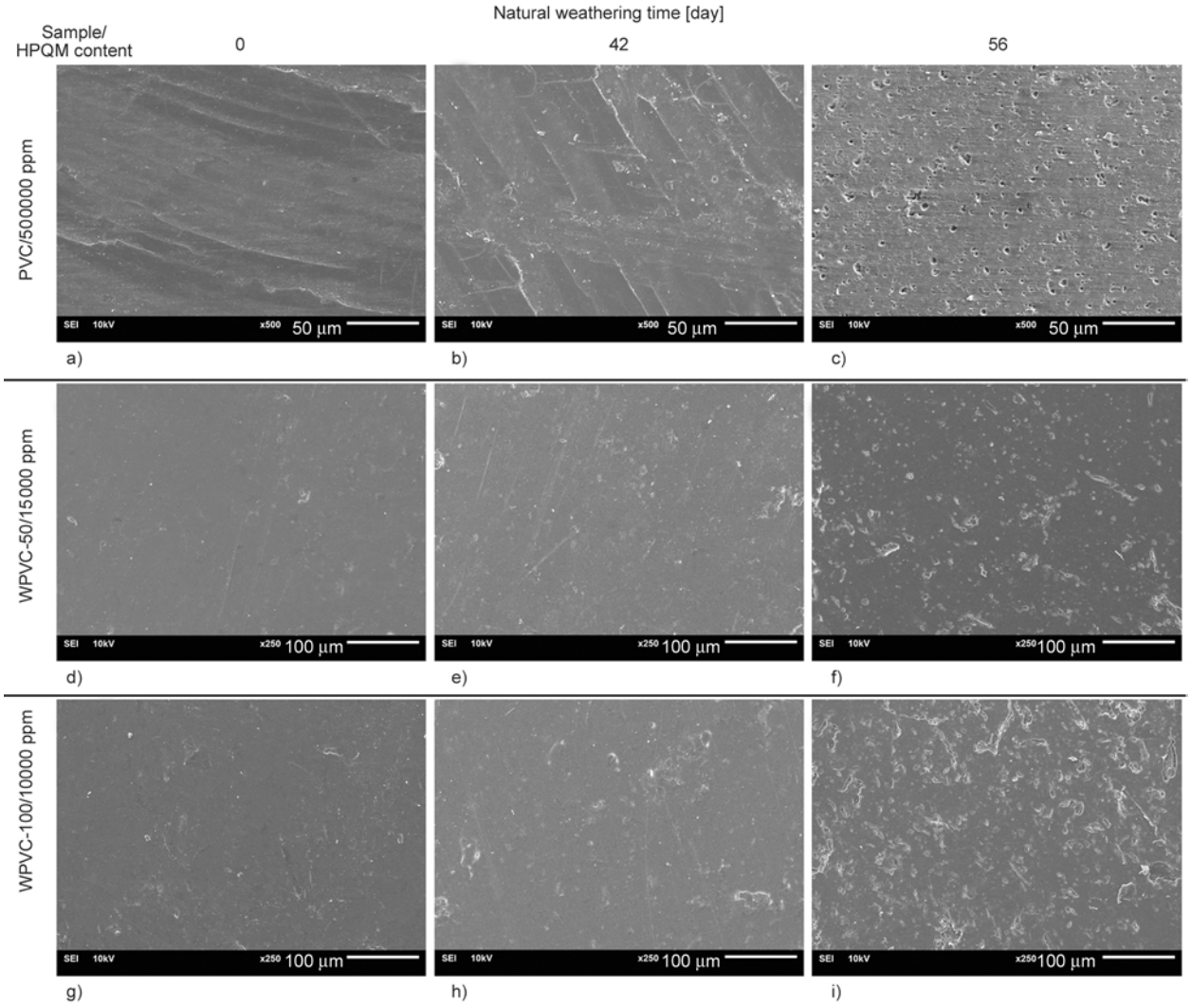

Figure 5. Scanning electron micrographs showing the surface morphology of PVC (a–c), WPVC-50 (d–f), and WPVC-100 (g–i) doped with HPQM, after natural weathering

Table 3. Flexural and physical properties of PVC and WPVC before and after QUV-accelerated weathering aging. Mean (±SD).

Sample	HPQM content [ppm]	QUV-accelerated weathering aging					
		Flexural modulus [MPa]		Flexural strength [MPa]		Lightness (L^*)	
		Before	After	Before	After	Before	After
PVC	0	2347.52 (±128.06)	2477.54 (±78.40)	60.84 (±1.33)	70.64 (±1.22)	80.32 (±0.46)	54.23 (±3.55)
	5000	2332.90 (±89.58)	2327.12(±156.40)	60.04 (±0.61)	70.85 (±2.46)	80.25 (±0.11)	54.86 (±0.56)
	10000	2096.87 (±88.31)	2358.64 (±33.53)	55.45 (±2.51)	64.71 (±3.42)	79.71 (±0.41)	53.27 (±3.22)
	15000	2147.14 (±72.09)	2229.32(±107.60)	53.02 (±1.12)	65.78 (±1.35)	80.26 (±0.27)	50.49 (±0.99)
	20000	2033.49 (±71.46)	2247.46 (±97.20)	52.30 (±0.88)	64.42 (±1.65)	79.28 (±0.31)	44.89 (±1.46)
	50000	2015.70 (±14.35)	2019.31(±153.02)	45.62 (±1.03)	56.06 (±1.46)	75.89 (±0.42)	42.07 (±0.52)
WPVC-50	0	2903.49 (±124.63)	1936.92 (±71.72)	38.35 (±1.62)	33.05 (±1.82)	28.92 (±0.31)	79.84 (±0.23)
	5000	3019.40 (±147.11)	2028.31(±101.44)	40.48 (±1.40)	31.53 (±1.19)	28.99 (±0.30)	77.59 (±0.73)
	10000	3089.78 (±98.48)	2036.32 (±53.53)	40.61 (±1.82)	32.13 (±0.88)	29.20 (±0.08)	78.62 (±0.51)
	15000	3009.10 (±160.80)	1980.18 (±94.87)	40.65 (±3.38)	28.55 (±1.38)	28.61 (±0.29)	75.46 (±0.59)
	20000	2972.06 (±122.81)	2263.35(±102.86)	39.90 (±1.47)	33.02 (±2.33)	29.17 (±0.16)	76.47 (±0.37)
	50000	3024.31 (±116.08)	2132.36 (±91.84)	40.02 (±2.12)	31.99 (±1.77)	28.41 (±0.06)	76.28 (±0.29)
WPVC-100	0	3434.00 (±111.41)	1617.47(±157.51)	37.54 (±1.23)	21.33 (±0.95)	28.43 (±0.17)	74.41 (±0.28)
	5000	3502.67 (±284.04)	1877.49 (±56.98)	40.78 (±2.27)	26.23 (±1.80)	28.62 (±0.33)	72.97 (±0.24)
	10000	3691.17 (±50.71)	2056.45(±122.58)	37.46 (±0.05)	24.63 (±2.83)	28.10 (±0.01)	72.51 (±0.59)
	15000	3471.54 (±155.10)	2188.33 (±198.51)	37.80 (±2.30)	26.61 (±2.93)	28.28 (±0.10)	73.45 (±0.91)
	20000	3464.02 (±122.43)	1934.47(±160.18)	40.59 (±2.13)	26.94 (±0.91)	26.97 (±0.23)	72.03 (±0.92)
	50000	3421.22 (±136.13)	1800.69(±190.37)	39.11 (±0.39)	25.45 (±2.63)	27.30 (±0.14)	69.23 (±0.42)

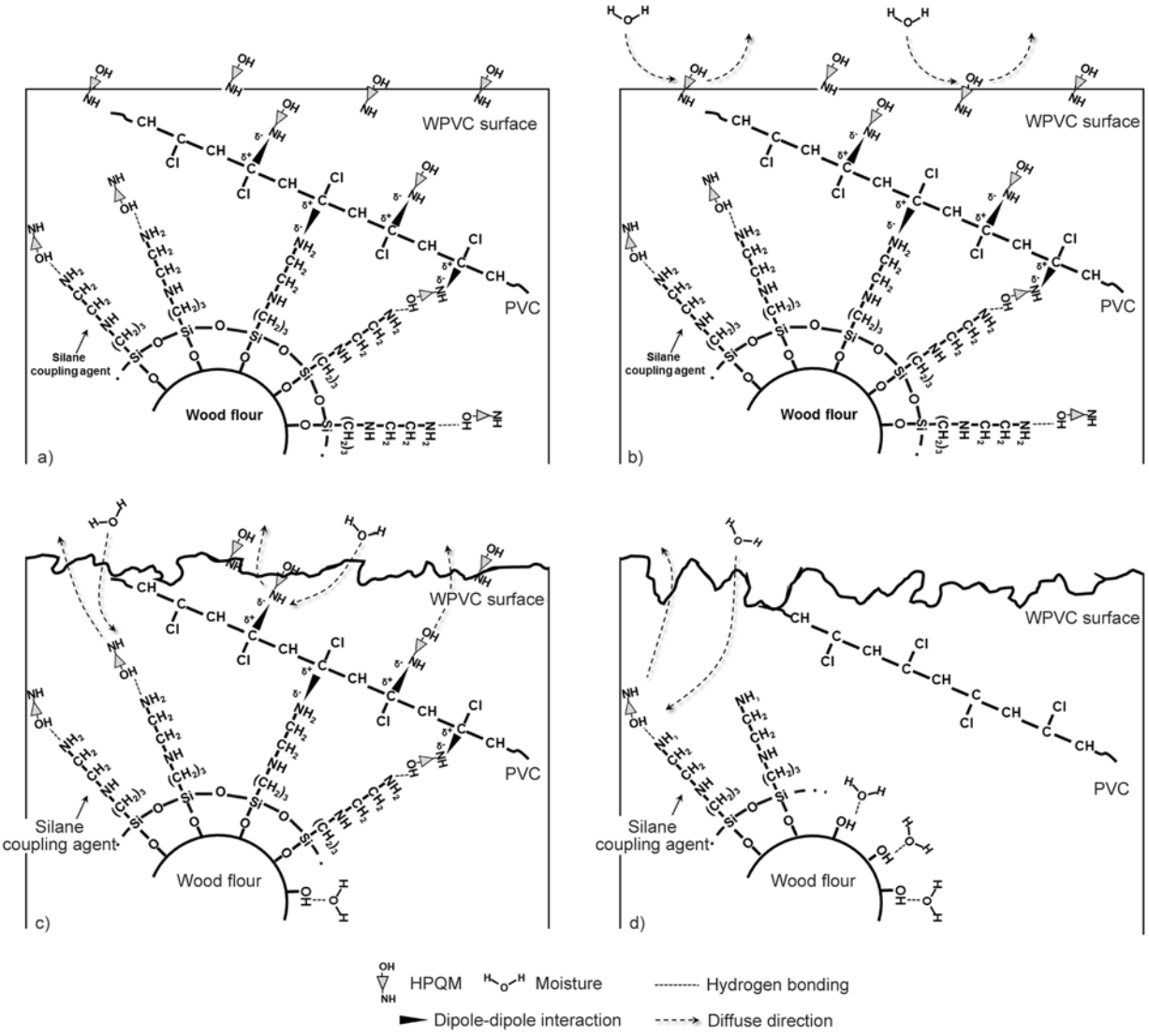

Figure 6. Release behavior of HPQM in the WPVC matrix when exposed to QUV-accelerated weathering aging or natural weathering: (a) initial stage, (b) water discharge, (c) surface cracks, and (d) more surface cracks with respect to time or severity of QUV-accelerated weathering aging

PVC and WPVC composites, but the changes were slower for natural weathering. This can also be explained by the differences in energy provided by natural weathering and QUV aging, as discussed earlier and in Chaochanchaikul *et al*. [33].

Tables 3 and 4 show the flexural and physical properties of PVC and WPVC before and after QUV-accelerated weathering aging and natural weathering. The results show that the flexural modulus for neat PVC was not affected by QUV-accelerated weathering aging and natural weathering. This is because of the high polarity and strong molecular interaction of PVC molecules. When considering the effect of wood flour, the flexural modulus of the WPVC-50 and WPVC-100 composites decreased with increased QUV-accelerated weathering aging

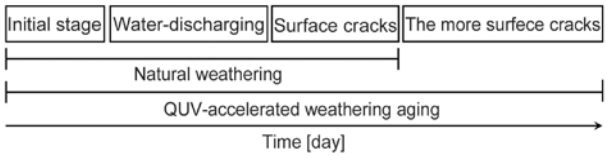

Figure 7. Timeline of release behavior of HPQM in the WPVC matrix when exposed to QUV-accelerated weathering aging and natural weathering

and natural weathering time. This can be explained by the moisture absorption ability of the wood flour. During the aging process, wood flour absorbed moisture, decreasing the interfacial adhesion between wood fibers and the polymer matrix. Moreover, the presence of wood appeared to accelerate the photodegradation of WPVC under QUV-accelerated weathering aging conditions and to decrease the

Table 4. Flexural and physical properties of PVC and WPVC before and after natural weathering. Mean (±SD).

Sample	HPQM content [ppm]	Natural weathering					
		Flexural modulus [MPa]		Flexural strength [MPa]		Lightness (L^*)	
		Before	After	Before	After	Before	After
PVC	0	2347.52 (±128.06)	2386.68 (±261.33)	60.84 (±1.33)	64.81 (±1.08)	80.32 (±0.46)	74.15 (±0.16)
	5000	2332.90 (±89.58)	2364.36 (±234.67)	60.04 (±0.61)	65.37 (±0.70)	80.25 (±0.11)	70.21 (±0.25)
	10000	2096.87 (±88.31)	2225.36 (±107.51)	55.45 (±2.51)	64.72 (±0.05)	79.71 (±0.41)	69.30 (±0.14)
	15000	2147.14 (±72.09)	2236.44 (±138.36)	53.02 (±1.12)	60.17 (±2.51)	80.26 (±0.27)	68.34 (±0.03)
	20000	2033.49 (±71.46)	2172.27 (±99.78)	52.30 (±0.88)	56.87 (±2.25)	79.28 (±0.31)	67.25 (±0.06)
	50000	2015.70 (±14.35)	2008.24 (±139.28)	45.62 (±1.03)	50.58 (±2.43)	75.89 (±0.42)	53.00 (±0.45)
WPVC-50	0	2903.49 (±124.63)	2345.43 (±125.86)	38.35 (±1.62)	35.74 (±1.31)	28.92 (±0.31)	70.56 (±0.75)
	5000	3019.40 (±147.11)	2423.23 (±72.72)	40.48 (±1.40)	35.72 (±1.00)	28.99 (±0.30)	73.88 (±0.90)
	10000	3089.78 (±98.48)1	2365.63 (±79.67)	40.61 (±1.82)	35.04 (±0.47)	29.20 (±0.08)	74.78 (±1.03)
	15000	3009.10 (±160.80)	2404.08 (±67.88)	40.65 (±3.38)	35.86 (±4.27)	28.61 (±0.29)	74.19 (±1.19)
	20000	2972.06 (±122.81)	2360.26 (±235.72)	39.90 (±1.47)	37.35 (±0.42)	29.17 (±0.16)	72.83 (±0.60)
	50000	3024.31 (±116.08)	2347.39 (±139.47)	40.02 (±2.12)	37.23 (±2.04)	28.41 (±0.06)	71.47 (±0.64)
WPVC-100	0	3434.00 (±111.41)	2400.56 (±68.82)	37.54 (±1.23)	29.03 (±0.07)	28.43 (±0.17)	74.98 (±0.33)
	5000	3502.67 (±284.04)	2528.45 (±128.96)	40.78 (±2.27)	30.04 (±0.53)	28.62 (±0.33)	73.89 (±0.16)
	10000	3691.17 (±50.71)	2300.54 (±189.01)	37.46 (±0.05)	30.39 (±2.25)	28.10 (±0.01)	74.85 (±0.28)
	15000	3471.54 (±155.10)	2346.40 (±42.29)-	37.80 (±2.30)	29.54 (±0.52)	28.28 (±0.10)	74.32 (±0.64)
	20000	3464.02 (±122.43)	2220.97 (±272.09)	40.59 (±2.13)	28.09 (±2.29)	26.97 (±0.23)	73.78 (±0.17)
	50000	3421.22 (±136.13)	2149.28 (±98.26)-	39.11 (±0.39)	29.35 (±1.32)	27.30 (±0.14)	73.98 (±0.35)

mechanical properties of the WPVC. This can be explained by the induced dipole–dipole interaction between OH– groups of wood flour and Cl atoms on the PVC chain [33].

The flexural strength of neat PVC increased during QUV-accelerated weathering aging and natural weathering. The increased flexural strength after aging can be explained by the presence of polyene [33]. In the case of WPVC-50 and WPVC-100, the flexural strength decreased during QUV-accelerated weathering aging and natural weathering. The decrease in flexural strength after aging can be explained by the same reason given above. When comparing between QUV-accelerated weathering aging and natural weathering, the reduction of flexural strength for WPVC-50 and WPVC-100 was more pronounced for QUV weathering. This is because the UV radiation under natural weathering was much lower than under QUV-accelerated weathering aging, which explains the greater WPVC degradation under QUV-accelerated weathering aging as compared with natural weathering.

The results of discoloration testing (Tables 3 and 4) for QUV-accelerated weathering aging and natural weathering indicate that the lightness (L^*) of neat PVC decreased with aging. This can be explained by the degradation of PVC, which is confirmed by the presence of polyene. However, the lightness of WPVC-50 and WPVC-100 increased with aging. The increase in lightness of the WPVC composites after QUV-accelerated weathering aging and natural weathering can be explained by the lignin structure in wood flour changing from hydroquinone to para-quinone [34].

4. Conclusions

Adding wood flour to the PVC matrix could improve the anti-fungal efficacy of the WPVC composites. For killing fungi, the optimal dosages of propylene glycol-based HPQM in PVC, WPVC-50, and WPVC-100 were 50000, 15000, and 10000 ppm, respectively. When comparing QUV-accelerated weathering aging and natural weathering, it was observed that the reduction of flexural strength for WPVC-50 and WPVC-100 was more pronounced for QUV weathering. The flexural properties of WPVC were found to decrease with increasing QUV-accelerated weathering aging and natural weathering, but this was not the case for neat PVC samples. The anti-fungal evaluation indicated that the samples doped with less than 20000 ppm propylene glycol-based HPQM had a more pronounced effect than the ones doped with higher dosages. The release behavior of HPQM in the WPVC matrix was dependent on the type of aging, PVC degradation, and water condensation during the aging process. The change in the anti-fungal per-

formance of WPVC under natural weathering was the same as that under QUV-accelerated weathering aging, but the rate of change was slower.

Acknowledgements

The authors would like to thank the Thailand Research Fund (TRF) for a Senior Research Scholar Grant (RTA 5580009) and a Researchers and Research for Industry Grant (MSD 56I0082). Appreciation is also expressed to the Office of the Higher Education Commission (Thailand) under the National Research Universities program, and to Koventure Co., Ltd. (Thailand), for financial support. The authors are grateful to the College of Industrial Technology, King Mongkut's University of Technology North Bangkok (KMUTNB), for the use of laboratory facilities.

References

[1] Pilarski J. M., Matuana L. M.: Durability of wood flour-plastic composites exposed to accelerated freeze–thaw cycling. Part I. Rigid PVC matrix. Journal of Vinyl and Additive Technology, **11**, 1–8 (2005). DOI: 10.1002/vnl.20029

[2] Pattamasattayasonthi N., Chaochanchaikul K., Rosarpitak V., Sombatsompop N.: Effects of UV weathering and a CeO_2-based coating layer on the mechanical and structural changes of wood/PVC composites. Journal of Vinyl and Additive Technology, **17**, 9–16 (2011). DOI: 10.1002/vnl.20246

[3] Gumargalieva K. Z., Zaikov G. E., Semenov S. A., Zhdanova O. A.: The influence of biodegradation on the loss of a plasticiser from poly(vinyl chloride). Polymer Degradation and Stability, **63**, 111–112 (1999). DOI: 10.1016/S0141-3910(98)00071-8

[4] Dawson-Andoh B., Matuana L. M., Harrison J.: Mold susceptibility of rigid PVC/wood-flour composites. Journal of Vinyl and Additive Technology, **10**, 179–186 (2004). DOI: 10.1002/vnl.20027

[5] Sombatsompop N., Phromchirasuk C.: Effects of acrylic based processing aids on processability, rheology, thermal and structural stability, and mechanical properties of PVC/wood sawdust composites. Journal of Applied Polymer Science, **92**, 782–790 (2004). DOI: 10.1002/app.13641

[6] El-Aghoury A., Vasudeva R. K., Banu D., Elektorowicz M., Feldman D.: Contribution to the study of fungal attack on some plasticized vinyl formulations. Journal of Polymers and the Environment, **14**, 135–147 (2006). DOI: 10.1007/s10924-006-0004-9

[7] Chaochanchaikul K., Sombatsompop N.: Stabilizations of molecular structures and mechanical properties of PVC and wood/PVC composites by Tinuvin and TiO_2 stabilizers. Polymer Engineering and Science, **51**, 1354–1365 (2011). DOI: 10.1002/pen.21893

[8] Faruk O., Bledzki A. K., Fink H-P., Sain M.: Biocomposites reinforced with natural fibers: 2000–2010. Progress in Polymer Science, **37**, 1552–1596 (2012). DOI: 10.1016/j.progpolymsci.2012.04.003

[9] Jeamtrakull S., Kositchaiyong A., Markpin T., Rosarpitak V., Sombatsompop N.: Effects of wood constituents and content, and glass fiber reinforcement on wear behavior of wood/PVC composites. Composites Part B: Engineering, **43**, 2721–2729 (2012). DOI: 10.1016/j.compositesb.2012.04.031

[10] Naumann A., Stephan I., Noll M.: Material resistance of weathered wood-plastic composites against fungal decay. International Biodeterioration and Biodegradation, **75**, 28–35 (2012). DOI: 10.1016/j.ibiod.2012.08.004

[11] Fang Y., Wang Q., Guo C., Song Y., Cooper P. A.: Effect of zinc borate and wood flour on thermal degradation and fire retardancy of polyvinyl chloride (PVC) composites. Journal of Analytical and Applied Pyrolysis, **100**, 230–236 (2013). DOI: 10.1016/j.jaap.2012.12.028

[12] Kırbaş Z., Keskin N., Güner A.: Biodegradation of polyvinylchloride (PVC) by white rot fungi. Toxicology Bulletin of Environmental Contamination, **63**, 335–342 (1999). DOI: 10.1007/s001289900985

[13] Gu J-D.: Microbiological deterioration and degradation of synthetic polymeric materials: Recent research advances. International Biodeterioration and Biodegradation, **52**, 69–91 (2003). DOI: 10.1016/S0964-8305(02)00177-4

[14] Lugauskas A., Levinskaite L., Peciulyte D.: Micromycetes as deterioration agents of polymeric materials. International Biodeterioration and Biodegradation, **52**, 233–242 (2003). DOI: 10.1016/S0964-8305(03)00110-0

[15] Lucas N., Bienaime C., Belloy C., Queneudec M., Silvestre F., Nava-Saucedo J. E.: Polymer biodegradation: Mechanisms and estimation techniques – A review. Chemosphere, **73**, 429–442 (2008). DOI: 10.1016/j.chemosphere.2008.06.064

[16] Lomelí-Ramírez M. G., Ochoa-Ruiz H. G., Fuentes-Talavera F. J., García-Enriquez S., Cerpa-Gallegos M. A., Silva-Guzmán J. A.: Evaluation of accelerated decay of wood plastic composites by *Xylophagus fungi*. International Biodeterioration and Biodegradation, **63**, 1030–1035 (2009). DOI: 10.1016/j.ibiod.2009.08.002

[17] Kaczmarek H., Bajer K.: Biodegradation of plasticized poly(vinyl chloride) containing cellulose. Journal of Polymer Science Part B: Polymer Physics, **45**, 903–919 (2007). DOI: 10.1002/polb.21100

[18] Coulthwaite L., Bayley K., Liauw C., Craig G., Verran J.: The effect of free and encapsulated OIT on the biodeterioration of plasticised PVC during burial in soil for 20 months. International Biodeterioration and Biodegradation, **56**, 86–93 (2005).
DOI: 10.1016/j.ibiod.2005.06.001

[19] Kositchaiyong A., Rosarpitak V., Sombatsompop N.: Antifungal properties and material characteristics of PVC and wood/PVC composites doped with carbamate-based fungicides. Polymer Engineering and Science, **54**, 1248–1259 (2014).
DOI: 10.1002/pen.23672

[20] Abuo-Rahma G. E. A. A., Sarhan H. A., Gad G. F. M.: Design, synthesis, antibacterial activity and physicochemical parameters of novel *N*-4-piperazinyl derivatives of norfloxacin. Bioorganic and Medicinal Chemistry, **17**, 3879–3886 (2009).
DOI: 10.1016/j.bmc.2009.04.027

[21] Zhang Z., Zhou W., Yu A.: Synthesis and antibacterial activity of 7-(Substituted)aminomethyl quinolones. Bioorganic and Medicinal Chemistry Letters, **14**, 393–395 (2004).
DOI: 10.1016/j.bmcl.2003.10.059

[22] Kawahara K., Tsuruda K., Morishita M., Uchida M.: Antibacterial effect of silver-zeolite on oral bacteria under anaerobic conditions. Dental Materials, **16**, 452–455 (2000).
DOI: 10.1016/S0109-5641(00)00050-6

[23] Ikeda Y., Park E. Y., Okuda N.: Bioconversion of waste office paper to gluconic acid in a turbine blade reactor by the filamentous fungus *Aspergillus niger*. Bioresource Technology, **97**, 1030–1035 (2006).
DOI: 10.1016/j.biortech.2005.04.040

[24] Gitchaiwat A., Kositchaiyong A., Sombatsompop K., Prapagdee B., Isarangkura K., Sombatsompop N.: Assessment and characterization of antifungal and antialgal performances for biocide-enhanced linear low-density polyethylene. Journal of Applied Polymer Science, **128**, 371–379 (2013).
DOI: 10.1002/app.37675

[25] Danilov R. A., Ekelund N. G. A.: Comparison of usefulness of three types of artificial substrata (glass, wood and plastic) when studying settlement patterns of periphyton in lakes of different trophic status. Journal of Microbiological Methods, **45**, 167–170 (2001).
DOI: 10.1016/S0167-7012(01)00247-0

[26] Lewin M., Goldstein I. S.: Wood structure and composition. Marcel Dekker, New York (1991).

[27] Matuana M. L., Woodhams T. R., Balatinecz J. J., Park B. C.: Influence of interfacial interactions on the properties of PVC/cellulosic fiber composites. Polymer Composites, **19**, 446–455 (1998).
DOI: 10.1002/pc.10119

[28] George J., Sreekala S. M., Thomas S.: A review on interface modification and characterization of natural fiber reinforced plastic composites. Polymer Engineering and Science, **41**, 1471–1485 (2001).
DOI: 10.1002/pen.10846

[29] Yue P., Chen G., Zhou S.: Improved interfacial bonding of PVC/wood-flour composites by lignin amine modification. Bioresources, **6**, 2022–2034 (2011).
DOI: 10.15376/biores.6.2.2022-2044

[30] Yim H., Kim S. D.: Physical properties of PVC/aminosilane-treated wood flour/organoclay composites. Polymers for Advanced Technologies, **23**, 1441–1445 (2012).
DOI: 10.1002/pat.2065

[31] Prapruddivongs C., Sombatsompop N.: Roles and evidence of wood flour as an antibacterial promoter for triclosan-filled poly(lactic acid). Composites Part B: Engineering, **43**, 2730–2737 (2012).
DOI: 10.1016/j.compositesb.2012.04.032

[32] Sributr A., Yamsaengsung W., Wimolmala E., Kositchaiyong A., Israngkura K., Sombatsompop N.: Effects of solution and solid forms of 2-hydroxypropyl-3-piperazinyl-quinoline carboxylic acid methacrylate on antibacterial, physical and mechanical properties of polypropylene sheeting. Journal of Plastic Film and Sheeting, **31**, 248–268 (2014).
DOI: 10.1177/8756087914561137

[33] Chaochanchaikul K., Rosarpitak V., Sombatsompop N.: Photodegradation profiles of PVC compound and wood/PVC composites under UV weathering. Express Polymer Letters, **7**, 146–160 (2013).
DOI: 10.3144/expresspolymlett.2013.14

[34] Muasher M., Sain M.: The efficacy of photostabilizers on the color change of wood filled plastic composites. Polymer Degradation and Stability, **91**, 1156–1165 (2006).
DOI: 10.1016/j.polymdegradstab.2005.06.024

eXPRESS Polymer Letters Vol.10, No.4 (2016) 302–310
Available online at www.expresspolymlett.com
DOI: 10.3144/expresspolymlett.2016.28

PSt-*b*-PU-*b*-PSt copolymers using tetraphenylethane-urethane macroinitiator through SARA ATRP

P. Chmielarz[1*], *P. Król*[2]

[1]Department of Physical Chemistry, Faculty of Chemistry, Rzeszów University of Technology, Al. Powstańców Warszawy 6, 35-959 Rzeszów, Poland
[2]Department of Polymer Science, Faculty of Chemistry, Rzeszów University of Technology, Al. Powstańców Warszawy 6, 35-959 Rzeszów, Poland

Received 21 August 2015; accepted in revised form 20 October 2015

Abstract. The course of supplemental activator and reducing agent (SARA) atom transfer radical polymerization (ATRP) has been presented in the presence of Cu^0. The novelty of this work is that SARA ATRP has been used for the first time to synthesize polystyrene-*b*-polyurethane-*b*-polystyrene copolymers by using tetraphenylethane-urethane macroinitiator as transitional products reacting with styrene in the presence of $Cu^{II}Br_2$/TPMA catalyst complex. The influence of copper surface area on the polymerization was examined. It was confirmed that in all cases, both the molecular weight of resulting copolymer increases linearly with increasing conversion as well as the value of $\ln([M]_0/[M])$ as a function of polymerization time increases linearly. A successful formation of the urethane-styrene copolymers was confirmed by NMR spectral studies.

Keywords: *polymer synthesis, molecular engineering, SARA ATRP, copolymers, polyurethanes, polystyrene*

1. Introduction

Atom transfer radical polymerization (ATRP) is one of the most rapidly developing areas of polymer science, allowing to obtain effective control over molecular weights (MWs), narrow molecular weight distributions (MWDs), architectures, and well-defined compositions [1–9]. However, normal ATRP has one significant limitation – it requires a large amount of the catalyst, which is sensitive to air and other oxidant. In order to overcome this drawback, Matyjaszewski's group has developed an improved ATRP technique, known as supplemental activator and reducing agent (SARA) [10]. This method provides a continuously controlled polymerization with reduction of the amount of copper-based catalyst complex (<50 ppm) due to constant regeneration of the Cu^I activator species by reducing agent (zerovalent metal – Cu^0), which compensates for any loss of Cu^I by termination [11]. Lowering the concentration of the catalysts not only results in 'greener' polymerization processes but also allows for the synthesis of polymers with high MW and high chain-end functionality [12]. Moreover, SARA ATRP offers simple removal and reuse of unreacted solid Cu^0, control of the polymerization rate by the amount of ligand and the surface area of Cu^0 [13, 14].

SARA ATRP, has Cu^I/Cu^{II} reactions as the major activation/deactivation ones, with Cu^0 acting as a supplemental activator of alkyl halides and a reducing agent for excess Cu^{II}, and limiting disproportionation of Cu^I (Figure 1) [15, 16].

Meanwhile, Percec group has proposed a single electron transfer living radical polymerization (SET-LRP) mechanism [18–22], which postulates Cu^0 as the major activator of alkyl halides, Cu^{II} as the major deactivator and assumes that Cu^I not participating

*Corresponding author, e-mail: p_chmiel@prz.edu.pl

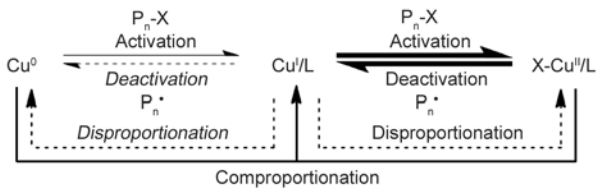

Figure 1. Mechanism of SARA ATRP. Line thickness denotes the contributions of the reactions (bold – major reactions, solid – contributing reactions, and dashed – negligible reactions) [17]

in activation reactions and instead undergoing very rapid disproportionation to Cu^0 and Cu^{II} [19]. Taking into account the Matyjaszewski's researches [17, 23, 24] it can be stated that the SARA ATRP mechanism is correct.

SARA ATRP/SET-LRP was successfully applied to relatively nonpolar monomers (e.g., styrene [25], butyl acrylate [26], methyl acrylate [14, 24, 26, 27], 2-(diisopropylamino) ethyl methacrylate [26, 28], methyl methacrylate [19, 26, 29]), as well as polar monomers (e.g., oligo(ethylene oxide) monomethyl ether acrylate [13], *N*-isopropylacrylamide [30]) for the preparation of a variety of polymeric materials with different structures and architectures, including homopolymers, and well-defined block copolymers.

However, tri-block copolymers have sparked much interest and their potential has been realized in many areas. These block copolymers have been used commercially as thermoplastic elastomers, adhesives, surfactants, hot-melt adhesives, blend compatibilizers, membranes, drug delivery polymers and biodegradable polymers [31]. Block copolymers are an interesting class of materials that possess different and often desirable properties compared to those of each individual homopolymer segments they are composed of [32]. As block length is playing a major role on the properties of the block copolymers, effective control of the block lengths is important and this can easily be achieved using different ATRP methods [31].

Bearing in mind the progress in application of the ATRP methods, it appears to be promising to use the SARA technique for obtaining urethane-styrene copolymers, which have been synthesized so far within a very limited scope by means of the ATRP classical mechanism [33, 34]. Therefore in this article, we have focused on the polymerization of styrene in the presence of tetraphenylethane-urethane macroinitiator (TPE-PU-TPE), $Cu^{II}Br_2$ as a catalyst, and tris(2-pyridylmethyl)amine (TPMA) as a complexing agent. The resulting polystyrene-*b*-polyurethane-*b*-polystyrene (PSt-*b*-PU-*b*-PSt) tri-block copolymers obtained through SARA ATRP are reported now for the first time. It is also worth noticing that urethane-styrene copolymers are already commonly used as adhesives, emulsifiers, modifiers of surface properties and polymer blend compatibilizers [35, 36].

2. Experimental section

2.1. Materials

4,4′-Methylene diphenyl diisocyanate (MDI), dibutyltin dilaurate (DBTDL), and Cu^0 wire (≥99%) were used as received from Sigma-Aldrich, USA. Polyoxytetramethylene glycol of molecular weight 1000 (PTMO; Merck, Germany) was purified by heating at 105 °C under vacuum for 3 h before use. Benzophenone (99%; ABCR GmbH, Germany), $Cu^{II}Br_2$ (99.999%; Sigma-Aldrich, USA) were used without further purification. Tris(2-pyridylmethyl) amine (TPMA) was prepared according to the published procedure [37]. Styrene (St; 99%; Sigma-Aldrich, USA) were passed through a column filled with basic alumina prior to use to remove any inhibitor. Tetraphenylethane-1,2-diol (TPED) was prepared from benzophenone and 2-propanol in the presence of acetic acid as reported in the literature [35]. Tetraphenylethane-urethane macroinitiator (TPE-PU-TPE) was synthesized from PTMG, MDI, and TPED according to the published procedure (M_n = 7600 g/mol) [35]. Acetic acid (99.5%), cyclohexane (99.9%), methanol (99.9%), acetone (99.5%) and 2-propanol (99%) were obtained from Chempur, Poland. Analytical grade *N*,*N*-dimethylformamide (DMF; Sigma-Aldrich, USA) and methyl ethyl ketone (MEK; Sigma-Aldrich, USA), were distilled and the middle portions were used after storing over type 4 Å molecular sieves.

2.2. Characterization techniques

Molecular weights and molecular weight distributions were determined by GPC (Polymer Standards Services (PSS) columns (guard, 10^4, 10^3, and 10^2 Å), with THF eluent at 25 °C, flow rate 1.00 mL/min, and with a differential refractive index (RI) detector (Viscotek, T60A)). The apparent molecular weights and dispersity (M_w/M_n) were determined with a calibration based on PS standards using TRISEC software from Viscotec Corporation. ^1H and ^{13}C NMR spectra of the macroinitiator and copolymers were

recorded on a FT-NMR Bruker Avance 500^{II} spectrometer using DMSO as a solvent and tetramethylsilane (TMS) as an internal standard. Monomer conversion and theoretical number-average molecular weight ($M_{n,th}$) were determined by NMR based on the previous research [31, 35].

2.3. Synthesis of urethane-styrene copolymers through SARA ATRP

The synthesis of tri-block copolymers was conducted, in the presence of 250 ppm of copper catalyst (Figure 2).

TPE-PU-TPE (5.09 g, 0.67 mmol) was placed in a Schlenk flask, and the flask was sealed with a glass stopper. The flask was evacuated and backfilled with nitrogen 5 times. Then, 20 mL of nitrogen purged DMF, 20 mL of N_2 purged St (18.12 g, 174 mmol) were added to the flask placed in an oil bath. Subsequently, 0.67 mL of $Cu^{II}Br_2$/2TPMA stock solution (0.05 M in DMF) was injected into the reaction solution. Next, Cu^0 wire (0.77, 1.69, 2.60 or 3.52 g) was immersed in the reaction solution. To initiate the polymerization reaction mixture was heated to 90 °C. Samples were withdrawn periodically to follow monomer conversion, using ^{1}H NMR. The polymerization was stopped after 46 h by opening the flask and exposing the catalyst to air. The products were purified by precipitation against MeOH, washed with cyclohexane, collected and dried under vacuum. Then the M_n and M_w/M_n were determined by GPC measurements (with PS standard curve).

2.4. Synthesis of urethane-styrene copolymers through radical polymerization

TPE-PU-TPE (5.09 g, 0.67 mmol) was placed in a Schlenk flask, and the flask was sealed with a glass stopper. The flask was evacuated and backfilled with nitrogen 5 times. Then, 20 mL of nitrogen purged DMF, 20 mL of N_2 purged St (18.12 g, 174 mmol) were added to the flask placed in an oil bath. To initiate the polymerization reaction mixture was heated to 90 °C. Samples were withdrawn periodically to follow the monomer conversion and M_n by ^{1}H NMR, and to determine M_w/M_n by GPC measurements with PS standard curve.

3. Results and discussion

In this paper SARA ATRP polymerizations of styrene in the presence of TPE-PU-TPE are reported for the first time. Polymerizations were conducted utilizing copper wire as an in situ reducing agent. The results are summarized in Table 1.

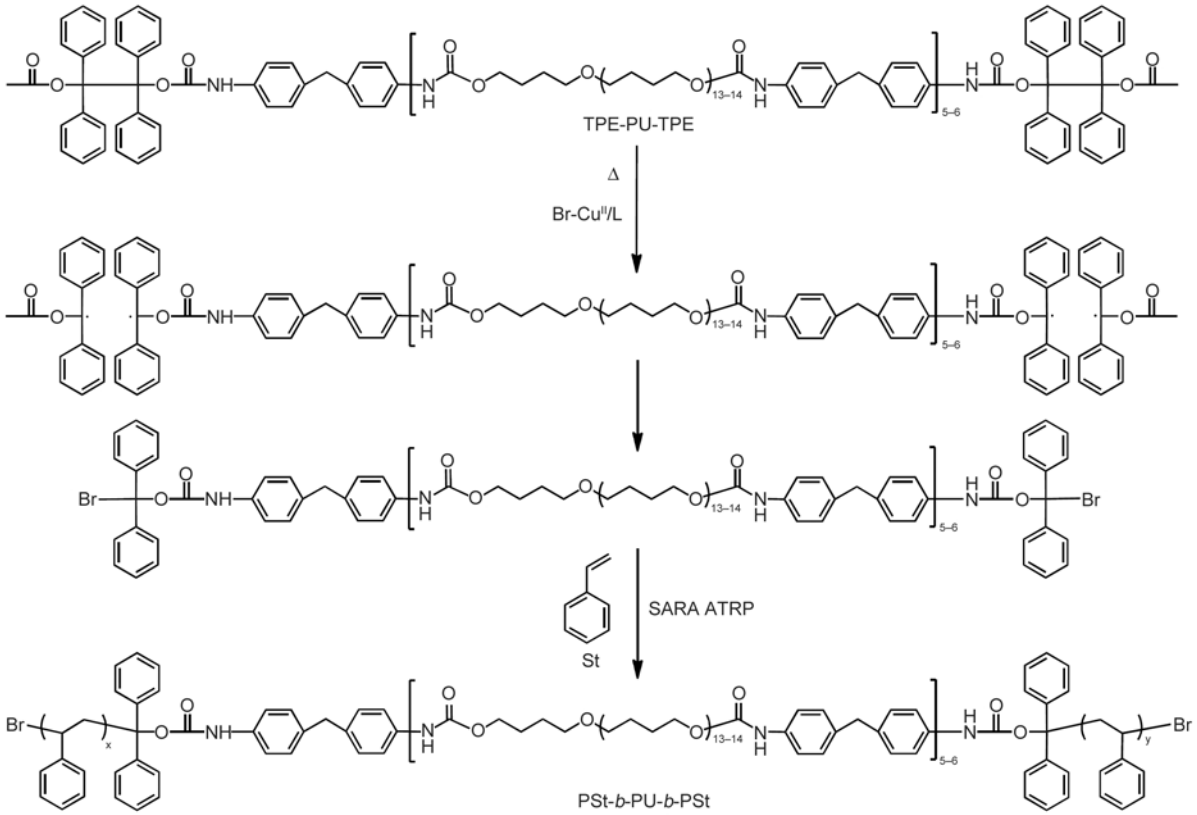

Figure 2. Synthesis of the urethane-styrene copolymers from tetraphenylethane-urethane macroinitiator [35, 38]

Table 1. SARA ATRP of PSt-*b*-PU-*b*-PSt utilizing copper wire

Entry	S/V[a] [cm^{-1}]	k_p^{app}[b] [h^{-1}]	Conv[b] [%]	$M_{n,theo}$[c] ($\cdot 10^{-3}$)	$M_{n,GPC}$[d] ($\cdot 10^{-3}$)	M_w/M_n[d]
1	0.09	0.027	70	26.6	27.0	1.29
2	0.19	0.031	75	27.9	28.8	1.28
3	0.29	0.034	79	28.9	29.6	1.26
4	0.39	0.041	84	30.4	31.0	1.18
5	–	0.003	13	11.1	13.3	2.38

General reaction conditions: $T = 90$ °C; $V_{tot} = 40$ mL, time = 46 h, copper wire ($L = 11$, 24, 37, and 50 cm, $d = 1$ mm); [St]:[TPE-PU-TPE calculated per 2 Br]:[Cu^{II}Br /2TPMA] = 130:1:0.05 (except entry 5: [St]:[TPE-PU-TPE calculated per 2 Br] = 130:1); [TPE-PU-TPE]$_0$ = 16.7 mM; [St]$_0$ = 4.3 M.

[a]Ratio of surface area (S) of Cu^0 to total volume of reaction mixture (V);

[b]Monomer conversion and apparent propagation rate constant (k_p^{app}) were determined by ^{1}H NMR, through the comparison of the integration of one vinyl proton of the remaining styrene at 5.25 ppm with the integration of the region at 7.96 ppm, which contained proton of the DMF;

[c]$M_{n,theo} = ([M]_0/[I]_0)\cdot\text{conversion}\cdot M_{monomer} + M_{macroinitiator}$;

[d]$M_{n,GPC}$ and MWD were determined by GPC with PS standards.

The effect of initiation system on the tri-block copolymer formation was evaluated by comparing radical polymerization and SARA ATRP systems (Table 1, entries 1–4 vs. 5, Figure 3a, 3b vs. Figure 4a, 4b). It was observed that the conventional radical polymerization of styrene was not controlled (Figure 3a, 3b), with broad polydispersity, MWD = 2.38 (Table 1, entry 5). In contrast, in the polymerizations conducted with TPE-PU-TPE/Cu^{II}Br$_2$/2TPMA/Cu$_0$/St system, monomer conversion reached 70–84% and evolution of experimental MW with conversion followed the theoretical prediction (Figure 4a, 4b). In this case, contributions of side reactions are lower, because SARA ATRP initiating system lower the concentration of primary radicals in the initiating step as in the case of normal ATRP. Briefly, a polymerization with TPE-PU-TPE/Cu^{II}Br$_2$/2TPMA/Cu^0/St system were 9–14 times faster (compare k_p^{app}; Table 1, entries 1–4 vs. 5) than with TPE-PU-TPE/St system.

3.1. Influence of the surface area of Cu to volume of reaction mixture ratio (S/V)

Since Cu^0 in the form of a wire (Table 1, entries 1–4) acts as a supplemental, rather than the major activator of alkyl halides [17], four experiments were conducted with varying amounts of Cu^0 surface area to solution volume ratio (S/V), from 0.09, 0.19, 0.29, to 0.39 cm^{-1} (Figure 4a, 4b, 5a–5d, and 6). Figure 4 illustrates the polymerization kinetics and molecular weight evolution with conversion. In this case, as the surface area of Cu^0 was decreased (S/V from 0.39 to 0.09 cm^{-1}), the rate of polymerization declined, k_p^{app} from 0.041 to 0.027 h^{-1}. These results suggest the involvement of Cu^0 in the rate-determining step of the reaction, see Equation (1):

$$R_a = k_p^{app}\left(\frac{S}{V}\right) \quad (1)$$

where R_a is defined as an activation rate of macroinitiator [13]. Moreover, molecular weights increased linearly with conversion (Figure 4b), and were almost identical to theoretical ones. This result comes from maintaining a constant number of chains throughout the polymerization, which requires sufficiently fast initiation (all chains are propagated before the reaction is stopped) and an absence of chain transfer

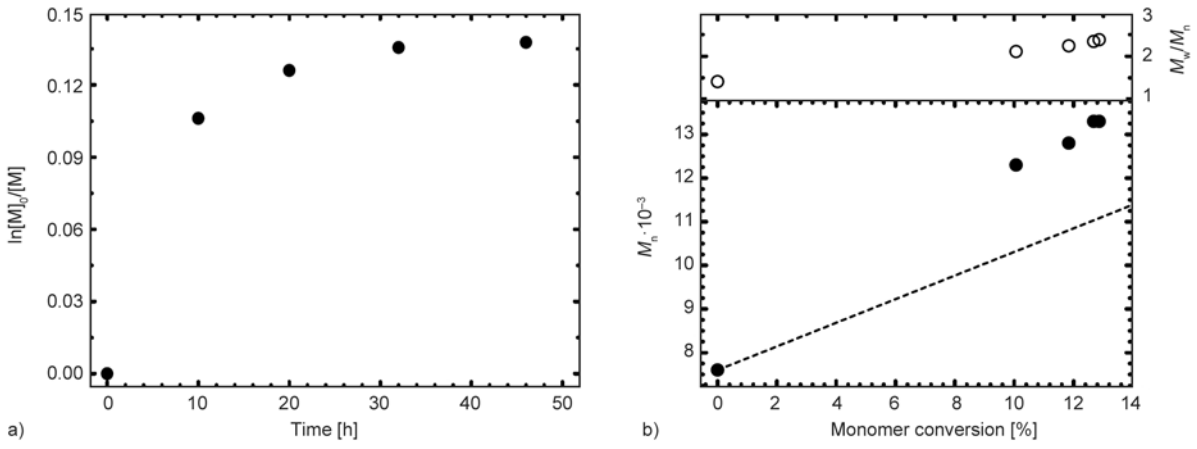

Figure 3. Polymerization of St. (a) First-order kinetic plot, and (b) M_n and M_w/M_n versus monomer conversion. Reaction conditions: [St]:[TPE-PU-TPE calculated per 2 Br] = 130:1; [TPE-PU-TPE]$_0$ = 16.7 mM; [St]$_0$ = 4.3 M, T = 90 °C; V_{tot} = 40 mL.

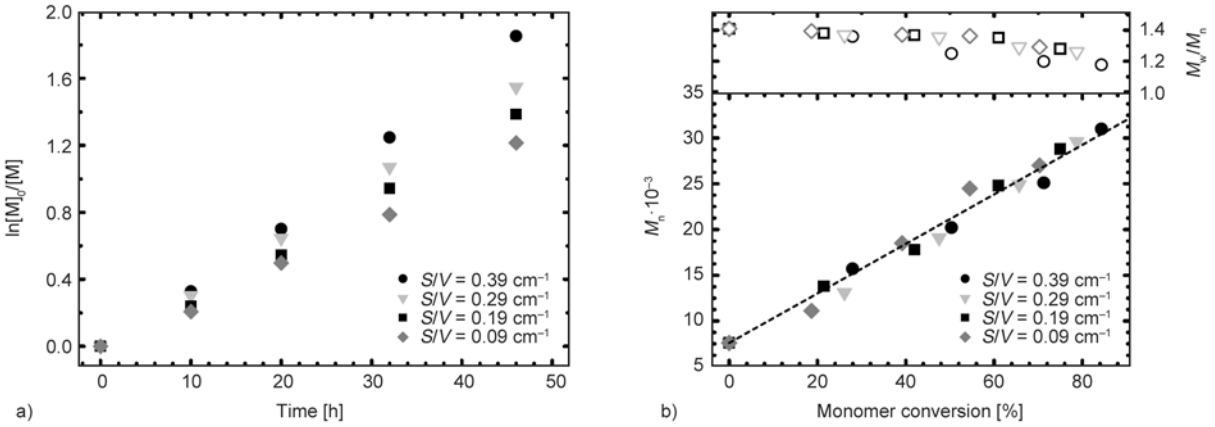

Figure 4. SARA ATRP of St as a function of the ratio of surface area of Cu0 to total volume of reaction solution (S/V = 0.09, 0.19, 0.29, and 0.39 cm^{-1}). (a) First-order kinetic plot of monomer conversion versus time, and (b) M_n and M_w/M_n versus monomer conversion. Reaction conditions: [St]:[TPE-PU-TPE calculated per 2 Br]:[Cu^{II}Br2/2TPMA] = 130:1:0.05; [TPE-PU-TPE]$_0$ = 16.7 mM; [St]$_0$ = 4.3 M, T = 90 °C; V_{tot} = 40 mL.

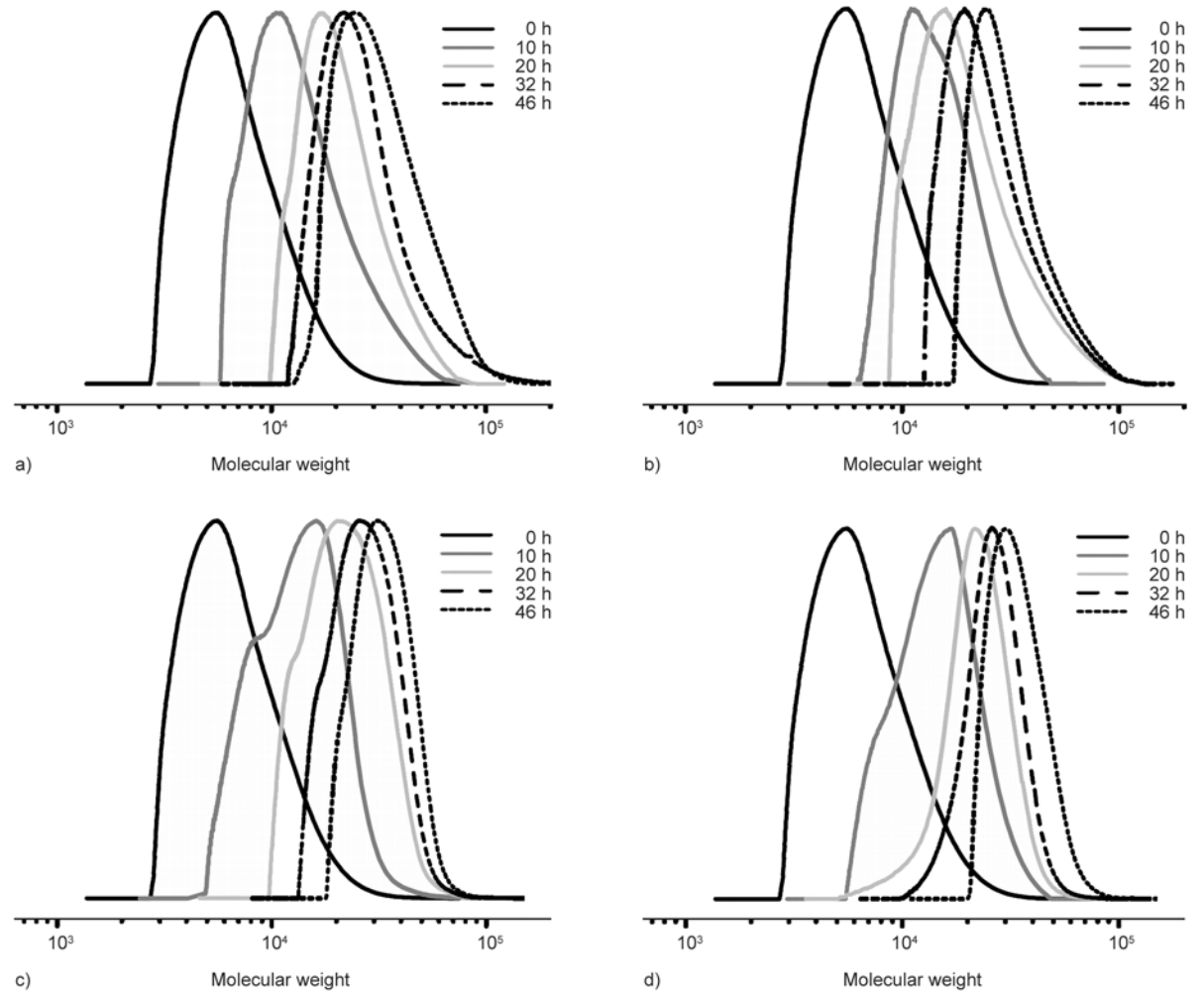

Figure 5. GPC traces during the SARA ATRP of St as a function of the ratio of surface area of Cu(0) reducing agent to total volume of reaction mixture ((a) S/V = 0.9 cm^{-1}, (b) S/V = 0.19 cm^{-1}, (c) S/V = 0.29 cm^{-1} and (d) S/V = 0.39 cm^{-1})

reactions (which increases the total number of chains) [39].

Furthermore, molecular weight distributions were independent of cooper surface area and remained low, with MWD = 1.18 at 84% of monomer conversion (S/V = 0.39 cm^{-1}) (Figure 5d).

Importantly, because the reaction rate was dependent on the Cu^0 surface area to reaction volume ratio

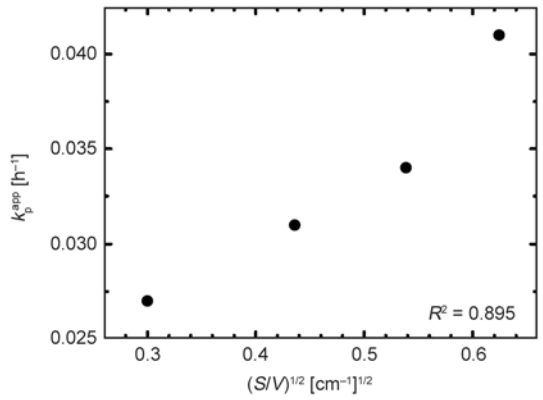

Figure 6. Relationship between the apparent propagation rate constant (k_p^{app}) versus the square root of the surface area of Cu0 to total volume of reaction solution (S/V = 0.09, 0.19, 0.29, and 0.39 cm^{-1}). Reaction conditions: [St]:[TPE-PU-TPE calculated per 2 Br]:[Cu^{II}Br$_2$/2TPMA] = 130:1:0.05; [TPE-PU-TPE]$_0$ = 16.7 mM; [St]$_0$ = 4.3 M, T = 90 °C; V_{tot} = 40 mL.

(S/V) and not on the total amount of cooper used, it also seemed feasible to increase this rate by either increasing the surface area of metallic cooper or decreasing total reaction volume [30]. As expected a linear relationship between the k_p^{app} and the square root of (S/V) was observed [40] (Figure 6), due to the surface uniformity and monodispersity of Cu^0 wire. It was demonstrated that the rate of polymerization (associated with k_p^{app}), scales appropriately with the approximate surface area of Cu^0 utilized.

3.2. Chemical structure of the tri-block copolymers

The chemical structure of the synthesized PSt-*b*-PU-*b*-PSt tri-block copolymer (Table 1, entry 4) was confirmed by ^{1}H NMR and ^{13}C NMR spectroscopy (Figure 7 and 8).

All the peaks corresponding to PU and PSt blocks are present in the ^{1}H and ^{13}C NMR, which is a clear evidence for the formation of tri-block copolymer (Table 1, entry 4). In the ^{1}H NMR spectrum of copolymer (Figure 7), the CH protons of PSt (α) appear at 1.70–1.95 ppm and CH_2 protons of PSt (β) appear at 1.30–1.42 ppm. The phenyl protons of PSt generally appear at 6.20–6.80 ppm (z) and at 6.80–7.30 ppm (z′, z″), to some extent merged with the peak of phenyl protons of MDI. In the ^{13}C NMR spectrum of

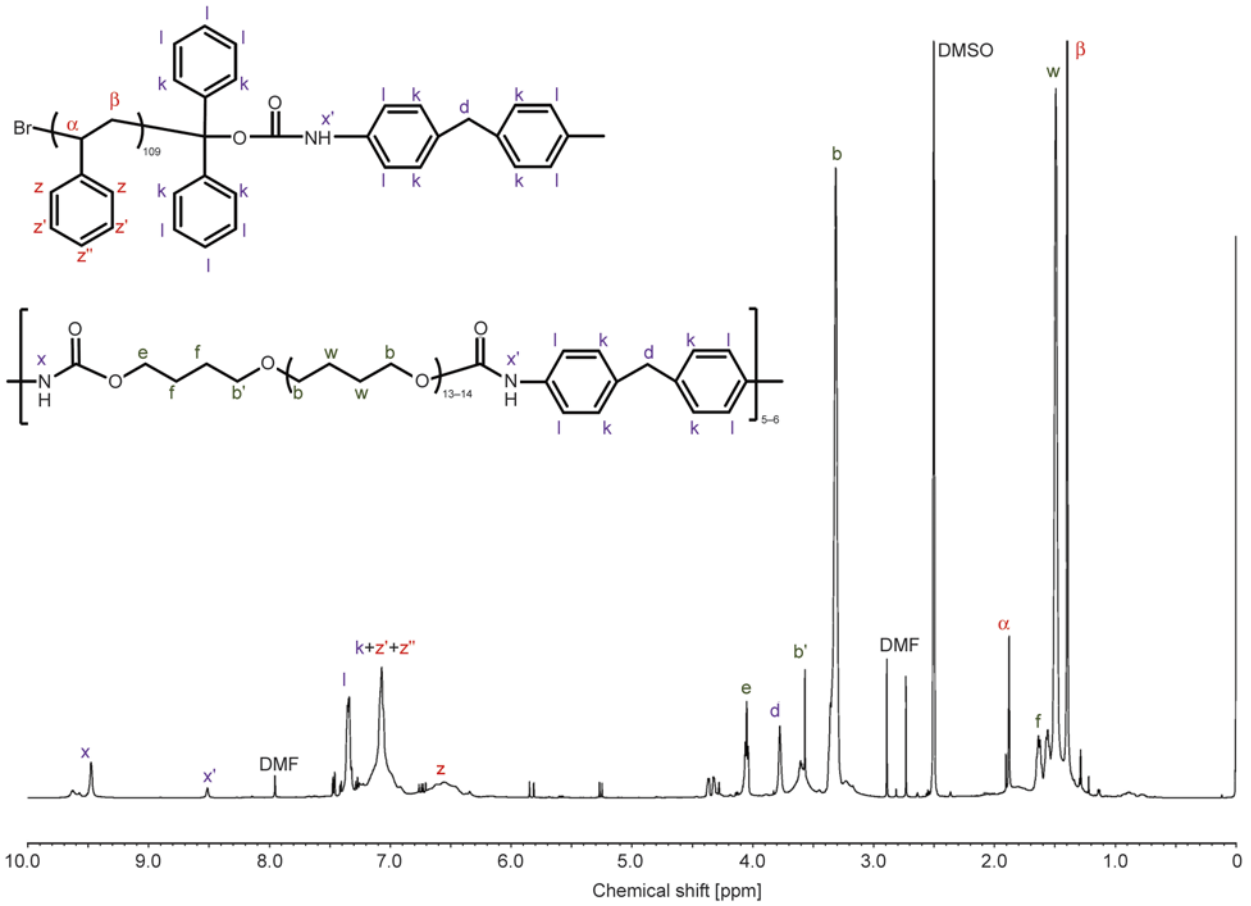

Figure 7. ^{1}H NMR spectrum of PSt-*b*-PU-*b*-PSt copolymers (Table 1, entry 4); M_n = 31 000, $Đ$ = 1.18) after purification (in DMSO)

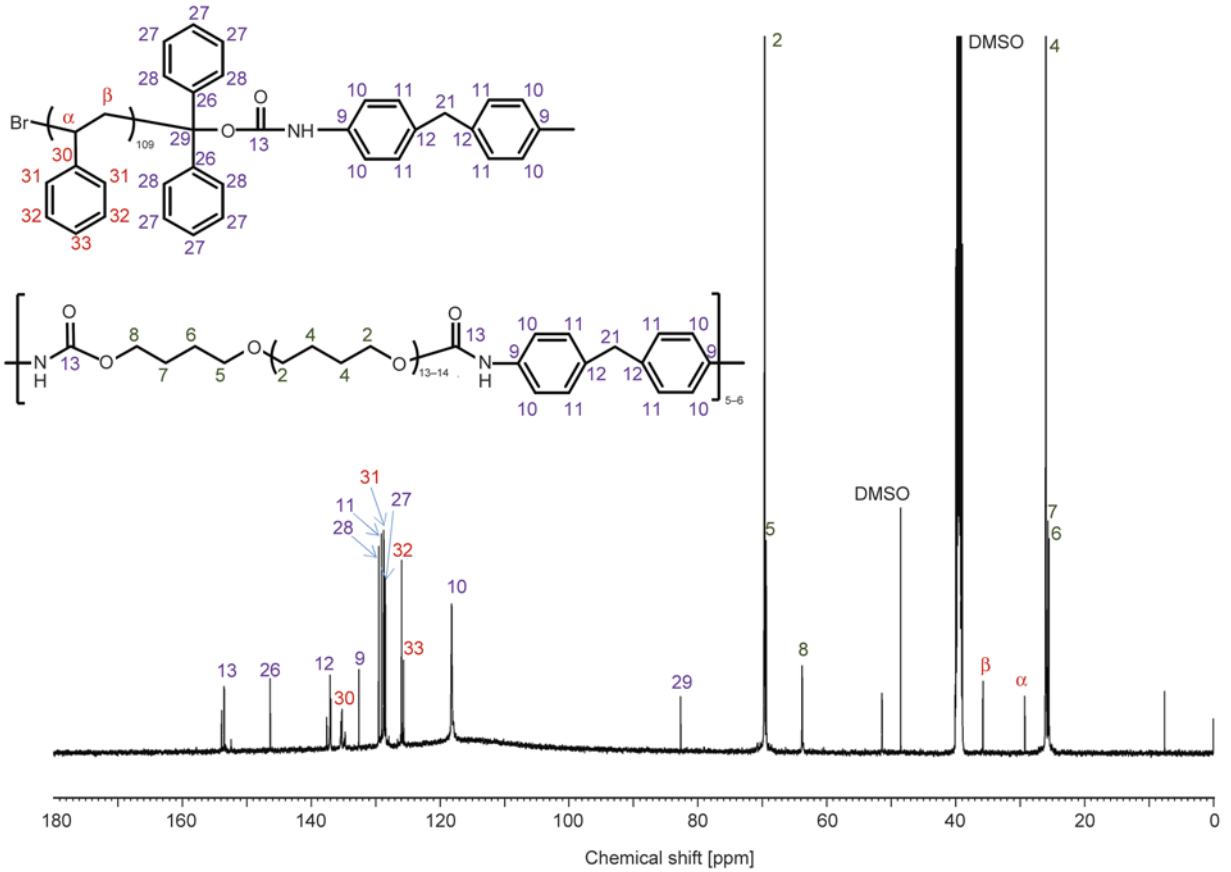

Figure 8. ^{13}C NMR spectrum of PSt-*b*-PU-*b*-PSt copolymers (Table 1, entry 4); M_n = 31 000, $Đ$ = 1.18) after purification (in DMSO)

the urethane-styrene copolymer (Figure 8), the CH carbon atoms of PSt (α) appear at 29.01 ppm and CH_2 protons of PSt (β) appear at 35.89 ppm. The phenyl protons of PSt (30–33) appear at 125.54–135.56 ppm, to some extent merged with the peak of phenyl protons of MDI.

The formation of a tri-block structure can be assumed based on the use of a symmetrical macroinitiator, but obtainment of precisely symmetrical tri-block copolymers cannot be supported by the NMR data.

4. Conclusions

Tetraphenylethane-urethane macroinitiator (TPE-PU-TPE) has been used to synthesize polystyrene-*b*-polyurethane-*b*-polystyrene (PSt-*b*-PU-*b*-PSt) tri-block copolymers through supplemental activator and reducing agent atom transfer radical polymerization (SARA ATRP). The influence of surface area of Cu^0 acting as a supplemental activator of alkyl halides and a reducing agent for excess Cu^{II} on the polymerization was examined. Excess of reducing agent slightly accelerates ATRP but does not interfere with the controlled growth. The DP of the resulting copolymers increased linearly with monomer conversion and semilogarithmic kinetic plots were linear, which confirmed the living nature of the SARA ATRP of styrene. The results from ^1H and ^{13}C NMR spectral studies support the formation of PSt-*b*-PU-*b*-PSt tri-block copolymers. Therefore SARA ATRP – method without pre-disproportionation of Cu^I species provide a powerful tool for the synthesis of a broad range of copolymers with controlled chain length and narrow molecular weight distributions.

Acknowledgements

NMR spectra were recorded in the Laboratory of Spectrometry, Faculty of Chemistry, Rzeszow University of Technology and were financed from DS budget.

References

[1] Wang J-S., Matyjaszewski K.: Controlled/'living' radical polymerization. Atom transfer radical polymerization in the presence of transition-metal complexes. Journal of the American Chemical Society, **117**, 5614–5615 (1995).
DOI: 10.1021/ja00125a035

[2] Hester J. F., Banerjee P., Won Y-Y., Akthakul A., Acar M. H., Mayes A. M.: ATRP of amphiphilic graft copolymers based on PVDF and their use as membrane additives. Macromolecules, **35**, 7652–7661 (2002).
DOI: 10.1021/ma0122270

[3] Ohno K., Morinaga T., Koh K., Tsujii Y., Fukuda T.: Synthesis of monodisperse silica particles coated with well-defined, high-density polymer brushes by surface-initiated atom transfer radical polymerization. Macromolecules, **38**, 2137–2142 (2005).
DOI: 10.1021/ma048011q

[4] Hansen N. M. L., Jankova K., Hvilsted S.: Fluoropolymer materials and architectures prepared by controlled radical polymerizations. European Polymer Journal, **43**, 255–293 (2007).
DOI: 10.1016/j.eurpolymj.2006.11.016

[5] Matyjaszewski K.: Atom transfer radical polymerization (ATRP): Current status and future perspectives. Macromolecules, **45**, 4015–4039 (2012).
DOI: 10.1021/ma3001719

[6] Siegwart D. J., Oh J. K., Matyjaszewski K.: ATRP in the design of functional materials for biomedical applications. Progress in Polymer Science, **37**, 18–37 (2012).
DOI: 10.1016/j.progpolymsci.2011.08.001

[7] He W., Jiang H., Zhang L., Cheng Z., Zhu X.: Atom transfer radical polymerization of hydrophilic monomers and its applications. Polymer Chemistry, **4**, 2919–2938 (2013).
DOI: 10.1039/C3PY00122A

[8] Król P., Chmielarz P.: Recent advances in ATRP methods in relation to the synthesis of copolymer coating materials. Progress in Organic Coatings, **77**, 913–948 (2014).
DOI: 10.1016/j.porgcoat.2014.01.027

[9] Hadasha W., Klumperman B.: Atom transfer radical polymerization as a powerful tool in the synthesis of molecular brushes. Polymer International, **63**, 824–834 (2014).
DOI: 10.1002/pi.4697

[10] Matyjaszewski K., Tsarevsky N. V., Braunecker W. A., Dong H., Huang J., Jakubowski W., Kwak Y., Nicolay R., Tang W., Yoon J. A.: Role of Cu^0 in controlled/'living' radical polymerization. Macromolecules, **40**, 7795–7806 (2007).
DOI: 10.1021/ma0717800

[11] di Lena F., Matyjaszewski K.: Transition metal catalysts for controlled radical polymerization. Progress in Polymer Science, **35**, 959–1021 (2010).
DOI: 10.1016/j.progpolymsci.2010.05.001

[12] Jakubowski W., Kirci-Denizli B., Gil R. R., Matyjaszewski K.: Polystyrene with improved chain-end functionality and higher molecular weight by ARGET ATRP. Macromolecular Chemistry and Physics, **209**, 32–39 (2008).
DOI: 10.1002/macp.200700425

[13] Konkolewicz D., Krys P., Góis J. R., Mendonça P. V., Zhong M., Wang Y., Gennaro A., Isse A. A., Fantin M., Matyjaszewski K.: Aqueous RDRP in the presence of Cu^0: The exceptional activity of Cu^I confirms the SARA ATRP mechanism. Macromolecules, **47**, 560–570 (2014).
DOI: 10.1021/ma4022983

[14] Harrisson S., Nicolas J.: In the (very) long run we are all dead: Activation and termination in SET-LRP/SARA-ATRP. Acs Macro Letters, **3**, 643–647 (2014).
DOI: 10.1021/mz500305j

[15] Zhang Y., Wang Y., Peng C-H., Zhong M., Zhu W., Konkolewicz D., Matyjaszewski K.: Copper-mediated CRP of methyl acrylate in the presence of metallic copper: Effect of ligand structure on reaction kinetics. Macromolecules, **45**, 78–86 (2012).
DOI: 10.1021/ma201963c

[16] Okelo G. O., He L.: Cu(0) as the reaction additive in purge-free ATRP-assisted DNA detection. Biosensors and Bioelectronics, **23**, 588–592 (2007).
DOI: 10.1016/j.bios.2007.06.011

[17] Konkolewicz D., Wang Y., Krys P., Zhong M. J., Isse A. A., Gennaro A., Matyjaszewski K.: SARA ATRP or SET-LRP. End of controversy? Polymer Chemistry, **5**, 4396–4417 (2014).
DOI: 10.1039/C4PY00149D

[18] Percec V., Popov A. V., Ramirez-Castillo E., Monteiro M., Barboiu B., Weichold O., Asansei A. D., Mitchell C. M.: Aqueous room temperature metal-catalyzed living radical polymerization of vinyl chloride. Journal of the American Chemical Society, **124**, 4940–4941 (2002).
DOI: 10.1021/ja0256055

[19] Percec V., Guliashvili T., Ladislaw J. S., Wistrand A., Stjerndahl A., Sienkowska M. J., Monteiro M. J., Sahoo S.: Ultrafast synthesis of ultrahigh molar mass polymers by metal-catalyzed living radical polymerization of acrylates, methacrylates, and vinyl chloride mediated by SET at 25 °C. Journal of the American Chemical Society, **128**, 14156–14165 (2006).
DOI: 10.1021/ja065484z

[20] Rosen B. M., Percec V.: Single-electron transfer and single-electron transfer degenerative chain transfer living radical polymerization. Chemical Reviews, **109**, 5069–5119 (2009).
DOI: 10.1021/cr900024j

[21] Levere M. E., Nguyen N. H., Leng X., Percec V.: Visualization of the crucial step in SET-LRP. Polymer Chemistry, **4**, 1635–1647 (2013).
DOI: 10.1039/c2py21084c

[22] Nguyen N. H., Sun H-J., Levere M. E., Fleischmann S., Percec V.: Where is Cu(0) generated by disproportionation during SET-LRP? Polymer Chemistry, **4**, 1328–1332 (2013).
DOI: 10.1039/c3py21133a

[23] Konkolewicz D., Wang Y., Zhong M., Krys P., Isse A. A., Gennaro A., Matyjaszewski K.: Reversible-deactivation radical polymerization in the presence of metallic copper. A critical assessment of the SARA ATRP and SET-LRP mechanisms. Macromolecules, **46**, 8749–8772 (2013).
DOI: 10.1021/ma401243k

[24] Wang Y., Zhong M., Zhu W., Peng C-H., Zhang Y., Konkolewicz D., Bortolamei N., Isse A. A., Gennaro A., Matyjaszewski K.: Reversible-deactivation radical polymerization in the presence of metallic copper. Comproportionation–disproportionation equilibria and kinetics. Macromolecules, **46**, 3793–3802 (2013).
DOI: 10.1021/ma400149t

[25] Tom J., Hornby B., West A., Harrisson S., Perrier S.: Copper(0)-mediated living radical polymerization of styrene. Polymer Chemistry, **1**, 420–422 (2010).
DOI: 10.1039/b9py00382g

[26] Abreu C. M. R., Serra A. C., Popov A. V., Matyjaszewski K., Guliashvili T., Coelho J. F. J.: Ambient temperature rapid SARA ATRP of acrylates and methacrylates in alcohol–water solutions mediated by a mixed sulfite/Cu(II)Br_2 catalytic system. Polymer Chemistry, **4**, 5629–5636 (2013).
DOI: 10.1039/C3PY00772C

[27] Zhong M., Wang Y., Krys P., Konkolewicz D., Matyjaszewski K.: Reversible-deactivation radical polymerization in the presence of metallic copper. Kinetic simulation. Macromolecules, **46**, 3816–3827 (2013).
DOI: 10.1021/ma4001513

[28] Góis J. R., Rocha N., Popov A. V., Guliashvili T., Matyjaszewski K., Serra A. C., Coelho J. F. J.: Synthesis of well-defined functionalized poly(2-(diisopropylamino) ethyl methacrylate) using ATRP with sodium dithionite as a SARA agent. Polymer Chemistry, **5**, 3919–3928 (2014).
DOI: 10.1039/C4PY00042K

[29] Hornby B. D., West A. G., Tom J. C., Waterson C., Harrisson S., Perrier S.: Copper(0)-mediated living radical polymerization of methyl methacrylate in a non-polar solvent. Macromolecular Rapid Communications, **31**, 1276–1280 (2010).
DOI: 10.1002/marc.201000031

[30] Chmielarz P., Krys P., Park S., Matyjaszewski K.: PEO-*b*-PNIPAM copolymers *via* SARA ATRP and *e*ATRP in aqueous media. Polymer, **71**, 143–147 (2015).
DOI: 10.1016/j.polymer.2015.06.042

[31] Król P., Chmielarz P.: Synthesis of PMMA-*b*-PU-*b*-PMMA tri-block copolymers through ARGET ATRP in the presence of air. Express Polymer Letters, **7**, 249–260 (2013).
DOI: 10.3144/expresspolymlett.2013.23

[32] Mueller L., Jakubowski W., Tang W., Matyjaszewski K.: Successful chain extension of polyacrylate and polystyrene macroinitiators with methacrylates in an ARGET and ICAR ATRP. Macromolecules, **40**, 6464–6472 (2007).
DOI: 10.1021/ma071130w

[33] Verma H., Kannan T.: Atom transfer radical polymerization of methyl methacrylate using telechelic tribromo terminated polyurethane macroinitiator. Journal of Macromolecular Science Part A: Pure and Applied Chemistry, **47**, 407–415 (2010).
DOI: 10.1080/10601321003659671

[34] Nayak S., Verma H., Kannan T.: Synthesis and characterization of amphiphilic and hydrophobic ABA-type tri-block copolymers using telechelic polyurethane as atom transfer radical polymerization macroinitiator. Colloid and Polymer Science, **288**, 181–188 (2010).
DOI: 10.1007/s00396-009-2149-2

[35] Król P., Chmielarz P.: Synthesis of poly(urethane-methacrylate) copolymers using tetraphenylethane-urethane macroinitiator by ARGET ATRP controlled polymerization method. Polimery, **59**, 279–292 (2014).
DOI: 10.14314/polimery.2014.279

[36] Dong H., Matyjaszewski K.: ARGET ATRP of 2-(dimethylamino)ethyl methacrylate as an intrinsic reducing agent. Macromolecules, **41**, 6868–6870 (2008).
DOI: 10.1021/ma8017553

[37] Xia J., Matyjaszewski K.: Controlled/'living' radical polymerization. Atom transfer radical polymerization catalyzed by copper(I) and picolylamine complexes. Macromolecules, **32**, 2434–2437 (1999).
DOI: 10.1021/ma981694n

[38] Verma H., Kannan T.: Synthesis of tri-block copolymers through reverse atom transfer radical polymerization of methyl methacrylate using polyurethane macroiniferter. Express Polymer Letters, **2**, 579–588 (2008).
DOI: 10.3144/expresspolymlett.2008.70

[39] Matyjaszewski K., Xia J.: Atom transfer radical polymerization. Chemical Reviews, **101**, 2921–2990 (2001).
DOI: 10.1021/cr940534g

[40] Nguyen N. H., Rosen B. M., Lligadas G., Percec V.: Surface-dependent kinetics of Cu(0)-wire-catalyzed single-electron transfer living radical polymerization of methyl acrylate in DMSO at 25 °C. Macromolecules, **42**, 2379–2386 (2009).
DOI: 10.1021/ma8028562

eXPRESS Polymer Letters Vol.10, No.4 (2016) 311–323
Available online at www.expresspolymlett.com
DOI: 10.3144/expresspolymlett.2016.29

On the strain-induced fibrillar microstructure of polyethylene: Influence of chemical structure, initial morphology and draw temperature

B. Xiong[1], *O. Lame*[1], *J-M. Chenal*[1], *C. Rochas*[2], *R. Seguela*[1*]

[1]MATEIS, UMR 5510 CNRS - INSA de Lyon, Batiment Blaise Pascal, Campus LyonTech La Doua, 69621 Villeurbanne, France
[2]CERMAV, UPR 5301 CNRS, BP 53, 38041 Grenoble, France

Received 31 July 2015; accepted in revised form 21 October 2015

Abstract. The influence of crystalline microstructure and molecular topology on the strain-induced fibrillar transformation of semi-crystalline polyethylenes having various chemical structures including co-unit content and molecular weight and crystallized under various thermal treatments was studied by *in situ* SAXS at different draw temperatures. The long period of the nascent microfibrils, L_{pf}, proved to be strongly dependent on the draw temperature but non-sensitive to the initial crystallization conditions. L_{pf} was smaller than the initial long period. Both findings have been ascribed to the strain-induced melting-recrystallization process as generally claimed in the literature. The microfibrils diameter, D_f, was shown to depend on the draw temperature and initial microstructure in a different way as L_{pf}. The evolution of D_f was shown to correlate with the interfacial layer thickness that mainly depends on the chemical structure of the chains. It was concluded that, in contrast to L_{pf}, the microfibril diameter should not be directly sensitive to the strain-induced melting-recrystallization. The proposed scenario is that after the generation of the protofibrils by fragmentation of the crystalline lamellae at yielding, the diameter of the microfibril during the course of their stabilization should be governed by the chain-unfolding and subsequent aggregation of the unfolded chains onto the lateral surface of the microfibrils. The morphogenesis of the microfibrils should therefore essentially depend on the chemical structure of the polymer that governs its crystallization ability, its chain topology and subsequently its fragmentation process at yielding. This scenario is summed up in a sketch.

Keywords: *thermal properties, polyethylene, microfibrils, crystallinity, crystalline microstructure*

1. Introduction

A general feature of the morphogenesis of semi-crystalline polymers is the regular stacking of chain-folded lamellar crystals alternating with amorphous layers. This stacking *s* characterized by an intercrystalline long period L_p including the crystalline lamella and amorphous layer thicknesses. The stacking long period is in the range of a few nanometers to a few tens. When crystallization is performed from a quiescent melt, the resulting microstructure is isotropic with a spherulitic arrangement of the lamella stacks as a result of the radial growth of the crystals from a common multiple nucleus often designated as axialite [1]. The size scale of spherulites ranges from a few to several hundred microns.

Upon plastic deformation at large strains, isotropic semicrystalline polymers transform into fibrillar materials that aroused a great interest from both academic and industrial standpoints owing to their remarkable mechanical performances [2–6] to be used as ropes, textile fibers for high performance tissues and fabrics, reinforcing fibers for polymer-based composites, etc.

*Corresponding author, e-mail: roland.seguela@insa-lyon.fr

The so-called fibrillar microstructure occurs via a plastic instability process, accompanied by a more or less pronounced geometric necking. The fibrillar microstructure consists of bundles of microfibrils parallel to the draw direction, each microfibril being made of a succession of crystal blocs and amorphous layers. It is generally admitted that this microstructure originates from the fragmentation of the crystalline lamellae into blocs during the plastic instability phenomenon [7–11]. These blocks rearrange into *strings of pearls* thanks to the molecular interconnections generated by the partial unfolding of chains. From small-angle X-ray scattering (SAXS) experiments, it was shown that the crystal blocs are regularly arranged with a long period, $L_{pf,}$ along the microfibril axis that is different from the long period of original isotropic material. For various kinds of semi-crystalline polymers, L_{pf} proved to be essentially dependent on the draw temperature in a similar way as L_p depends on the temperature of quiescent crystallization from the melt or from solution, i.e. the higher the temperature the greater the long period [7–10]. Considering this complete reconstruction of the stacking long period, many authors claimed that fibrillar transformation necessarily involves a strain-induced melting-recrystallization process [11, 12]. Several phenomena have been proposed for providing physical support to this hypothesis: the chain-unfolding mechanism that necessarily goes through a transitory state of disordered chain segments analogous to the amorphous state, the conversion of plastic work into heat that may generate significant temperature increase at high strain rates, the stress-induced depression of the melting point, etc. It was even suggested by Mandelkern and co-workers that the initial morphology was completely erased by the strain-induced melting-recrystallization [13, 14].

In parallel, a few SAXS studies have been performed for characterizing the microfibril transverse dimension or width thanks to a Guinier analysis of the transverse intensity profile of the characteristic 2-streak of the one-dimensional fibrillar stacking [7, 15–20]. In this analysis framework, the transverse intensity profile is considered to be governed by the form factor of the scattering microfibrils. It turned out that both draw temperature and draw ratio, and subsequent annealing treatment as well, have an influence of the microfibril width. However, no correlations were made with structural features of the initial semi-crystalline morphology.

The above remarks regarding the fibrillar morphology contrast with the numerous studies dealing with the incidence on the elementary mechanisms of plastic deformation of the initial morphology and molecular topological of semi-crystalline polymers, such as crystallinity, crystal thickness, chain entanglement and tie chain densities, etc. together with deformation conditions [21–36]. It was shown in some cases that these structural or experimental factors could have an impact on the mechanism of fragmentation of the crystalline lamella via the local stress distribution on the crystalline lamellae [22, 25, 30]. So that one may foresee some consequences on the microfibril morphology in spite of the melting-recrystallization process.

In a previous paper [37] we reported an *in situ* SAXS study of the fibrillar transformation at room temperature of a series of polyethylene materials covering a wide range of crystallinity $0.48 < X_c < 0.80$ and long period 17 nm $< L_p <$ 37 nm. It was shown that though the fibrillar long period did not depend on the initial morphology, the width of the microfibrils displayed a correlation with the initial semi-crystalline morphology. It was suggested that the microfibril width was related to the average size of the initial crystal fragments via the formation of protofibrils that retaind the memory of the crystallization conditions via the density of tie chains and chain entanglements that might survive the strain-induced melting-recrystallization.

The present study is an extension over a large temperature range of our former work of the post-yield drawing of PE. In contrast to most of the previous works dealing with *ex situ* analysis of fibrillar structure at room temperature, SAXS measurements were carried out *in situ* during drawing in order to prevent eventual post-drawing crystallization and topological rearrangements. This is likely to provide information closely related to the morphogenesis of the microfibrils during drawing and help understanding the mechanical behavior of the drawn materials in relation to their processing and crystallization conditions. The morphological changes that occur during ultra-drawing beyond the fibrillation stage [4] are not discussed in this work.

2. Experiment

2.1. Materials and sample preparation

Four linear polyethylenes with different hexene co-unit contents and very close molecular weights

were provided by Total Petrochemicals (Feluy, Belgium). The molecular characteristics are given in Table 1. It is worth noticing that is spite of their very close M_n and M_w values and similar co-units contents, PE-C and PE-D have significantly different M_z values. This is relevant to the presence of a small amount of very long chains in PE-D that is expected to influence the crystallization behavior [38, 39].

The four polymers have been submitted to three different thermal treatments in order to modify their crystalline microstructure and chain-topology. Quenching is expected to keep the entanglement topology of the melt and generate thin crystals. In contrast, annealing in the solid state and isothermal crystallization from the melt are expected to reduce the entanglement density and generate thick crystals, the latter treatment being more efficient than the former one as evidenced through the data of Table 2. The polymer pellets were compression-molded at 170 °C into 500 μm sheets between aluminum foils in a heating press and then quenched into water at room temperature (RT). These samples were called 'quenched'. Some of the quenched samples were heat treated via two different ways in order to modify the crystalline microstructure. The samples labeled 'annealed' were heated up to the temperature T_c = 122 °C for 15 hours and subsequently slowly cooled down to RT (see T_c determination below). The samples called 'isotherm' were melted at 170 °C and then cooled in a thermostatic oil bath at the temperature T_c and held at this temperature for 15 hours. More details on the sample preparation are given elsewhere [37, 40].

2.2. Differential scanning calorimetry (DSC)

Thermal analysis was conducted on a DSC7 apparatus from Perkin-Elmer using samples of 5–7 mg. The temperature and heat flow scales were calibrated using high purity indium. The heating and cooling scans were recorded at a rate of 10 °C/min. The crystal weight fraction, X_c, was computed from the melting enthalpy of the samples, using the value ΔH_m° = 290 J/g for the heat of fusion of perfectly crystalline PE [41]. The standard deviation of X_c data is about 1%.

Table 1. Molecular characteristics of the row PE materials

Material	Co-unit [mol%]	M_n [kg/mol]	M_w [kg/mol]	M_z [kg/mol]
PE-A	1.8	14.3	231	2770
PE-B	0.8	15.8	187	1770
PE-C	0.1	15.4	216	2770
PE-D	0.1	15.0	229	4100

2.3. SAXS measurements

Small-angle X-ray scattering (SAXS) experiments were performed on the BM02 beamline of the European Synchrotron Radiation Facility (Grenoble, France) using a wavelength λ = 0.154 nm. The 2D-SAXS patterns were recorded on a CCD camera from Princeton Instruments (Trenton NJ, USA) which was set at sample-detector distance of 158 cm. *In situ* recording of SAXS patterns during uniaxial tensile testing was performed using a home-made tensile stage allowing symmetric stretching of the sample. This ensured that all data were recorded from the same location on the sample during deformation. The dumbbell-shaped samples were 11 mm in gauge length, 4 mm in width and 0.5 mm in thickness. The nominal or engineering strain is defined as $\varepsilon = (L - L_0)/L_0$ with L_0 and L the sample gauge length before and during tensile drawing. The strain rate was $6.4 \cdot 10^{-4}$ s^{-1} to make sure that the strain increment was less than 0.1% during the 5 s time for every pattern recording. The experiments were performed at several draw temperatures in the range 25 °C < T_d < 100 °C for each sample.

The Lorentz-corrected intensity profiles of the isotropic samples prior to straining were obtained by azimuthal integration of the 2D patterns according to Equation (1):

$$I(q) = q_2 \int_0^{2\pi} I(q,\varphi)\mathrm{d}\varphi \tag{1}$$

where φ is the azimuthal angle. The average long period of the lamellar stacking, L_p, was then determined from the Bragg's relation (Equation (2)):

$$L_p = \frac{2\pi}{q_{max}} \tag{2}$$

where q_{max} is the scattering vector at the maximum of the correlation peak as determined by a Gaussian fitting. The standard deviation of the L_p data does not exceed 1.0 nm.

The crystal thickness, L_c, of the isotropic samples was computed from Equation (3):

$$L_c = L_p X_c \frac{\rho}{\rho_c} \tag{3}$$

where ρ_c = 1.00 g/cm^3 is the density of the crystalline phase. This relation assumes much larger length and width of the crystalline lamellae as compared with thickness.

Regarding the drawn samples displaying the characteristic two-streak meridian pattern, the one-dimension intensity profile along the meridian was obtained by projection on the meridian of the 2D-pattern according to Stribeck's method [19]. Then the long period along the draw axis, L_{pf}, was estimated by using Equation (2).

The structural data of all isotropic PE samples at RT are reported in Table 2. Also are reported the weight fraction of interfacial zone between crystal and amorphous regions as assessed from Raman spectroscopy, X_i, the concentration of stress transmitters [*ST*] according to Brown-Huang's theoretical approach, and the natural draw ratio at RT, λ_N, as already determined in a previous study via *in situ* mechanical testing [38, 42].

A convenient way for quantifying the microfibril width is to analyze the transverse intensity profile of the lobes of the 2-streak SAXS patterns. The scattering objects were supposed to be individually embedded in a medium of lower electron density consisting of amorphous chains and cavities, without interference between them. The corresponding model consists of either elongated cylinders or discs. In both instance, the analysis of the transverse intensity profile of the streak-like lobes can be performed via Guinier's approximation of the form factor leading to an estimation of the transverse dimension of the scattering elements. In the case of scattering cylinders, the relevant Guinier's approximation function is given by Equation (4) [43]:

$$I(q) = I_0 \exp\left(-\frac{q^2 D_f^2}{4} \right) \quad (4)$$

where D_f is the cylinder diameter with $D_f = 2R_f$ where R_f is the radius of gyration. Fitting the experimental intensity data with Equation (4) enabled computing only one diameter value for each sample as demonstrated in the previous study [37]. The standard deviation of the D_f data was about 1.0 nm or less.

3. Results

All the SAXS data regarding the fibrillar structure of the materials in the present work are relevant to samples drawn at the same engineering strain ε = 1.3. At this strain level the fibrillar transformation has not reached the whole sample length but the necking process is stabilized at the so-called *natural draw ratio*, λ_N, and propagates along the sample [44, 45]. This enables to study the *nascent fibrillar structure* of each material, irrespective of its macroscopic behavior.

Firstly, it is to be noticed that the λ_N data of Table 2 vary over a very large range and do not display correlation with either X_c or L_p. On the other hand, the λ_N data depend on the thermal treatment for every PE type. This is an evidence that the microfibrillar structure does depend on the initial crystalline microstructure is not thoroughly erased by the strain-induced melting recrystallization process. This strong correlation enabled using λ_N as an indicator of the long-term mechanical properties via the correlation with the initial molecular topology [46, 47].

Figure 1 shows the typical shape of a SAXS pattern recorded from the quenched PE-A after necking at

Table 2. Structural and physical characteristics of the isotropic PE samples at RT

Materials		X_c [%]	[*ST*]	X_i [%]	λ_N	L_p [nm]	L_c [nm]
PE-A	quenched	48	0.24	13	3.5	17	8
	annealed	52	0.17	14	4.0	23	11
	isotherm	53	0.15	11	4.7	24	12
PE-B	quenched	54	0.19	8	4.2	19	9
	annealed	62	0.14	8	4.7	22	13
	isotherm	65	0.09	4	5.5	26	16
PE-C	quenched	65	0.19	5	4.5	20	12
	annealed	73	0.08	5	6.0	30	21
	isotherm	75	0.03	5	7.5	36	26
PE-D	quenched	69	0.17	3	5.0	22	14
	annealed	77	0.08	5	5.7	30	22
	isotherm	80	0.03	–	7.0	37	29

T_d = 50 °C. This figure schematically shows the methodology of calculation of the microfibril long period L_{pf} and diameter D_f. The strong central scattering extending in equatorial direction arises from interfibrillar cavities or low density regions [19]. The electron density contrast between these regions and the microfibrils is so high that this scattering can turn extremely intense and merge onto the streak-like scattering, particularly for high crystallinity materials. In this instance, the analysis of the structural characteristics of the microfibrils is prohibited. However increasing the draw temperature reduces the propensity for cavitation or interfibrillar density fluctuations [48] so that more samples can be investigated during drawing at elevated temperature than in the case of the drawing at RT. This is one of the major benefits from the present study compared to our previous one [37].

Figure 2 shows the evolution of the meridian intensity profile of quenched PE-A as a function of strain at two different T_d. The SAXS patterns change from isotropic to highly anisotropic patterns with two streak-like scattering patterns during the elongation of samples.

The central SAXS patterns of Figures 2a and 2b show the SAXS patterns about the onset of the streak-like reflections characteristic of the fibrillar structure, for both T_d. The actual strain onset decreases

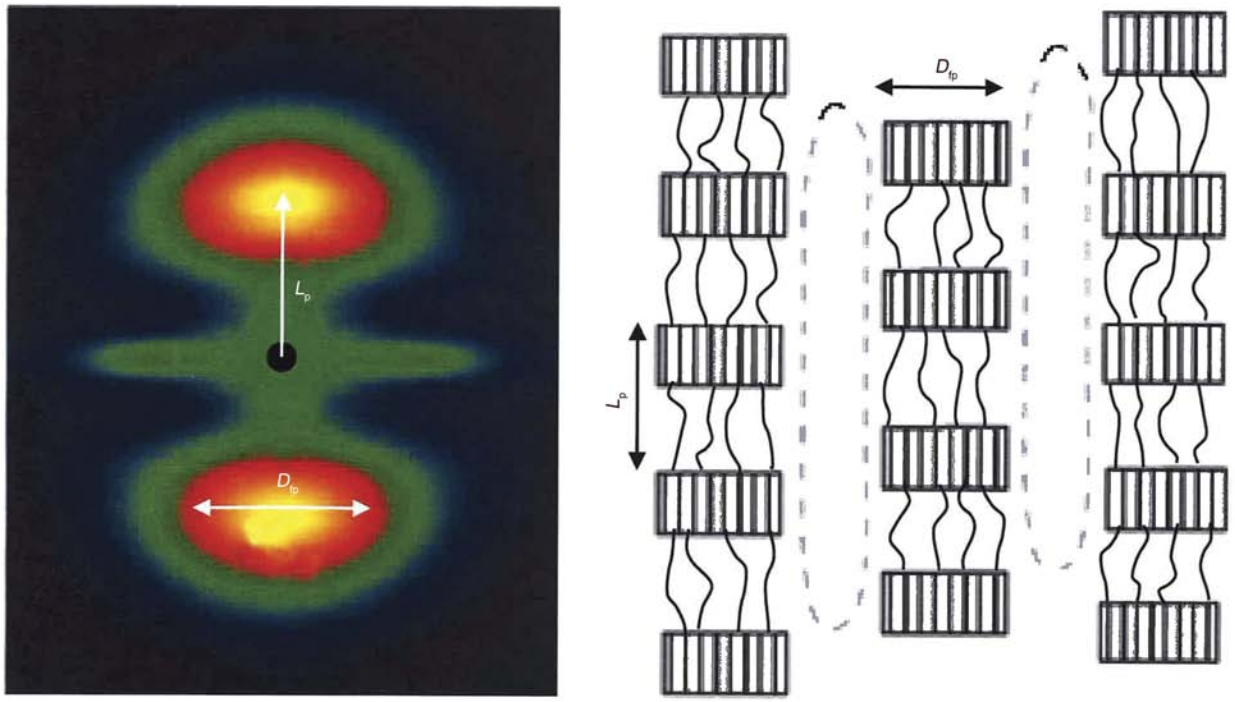

Figure 1. Schematic SAXS pattern and molecular model of the fibrillar microstructure (borrowed from Stribeck ref. 19)

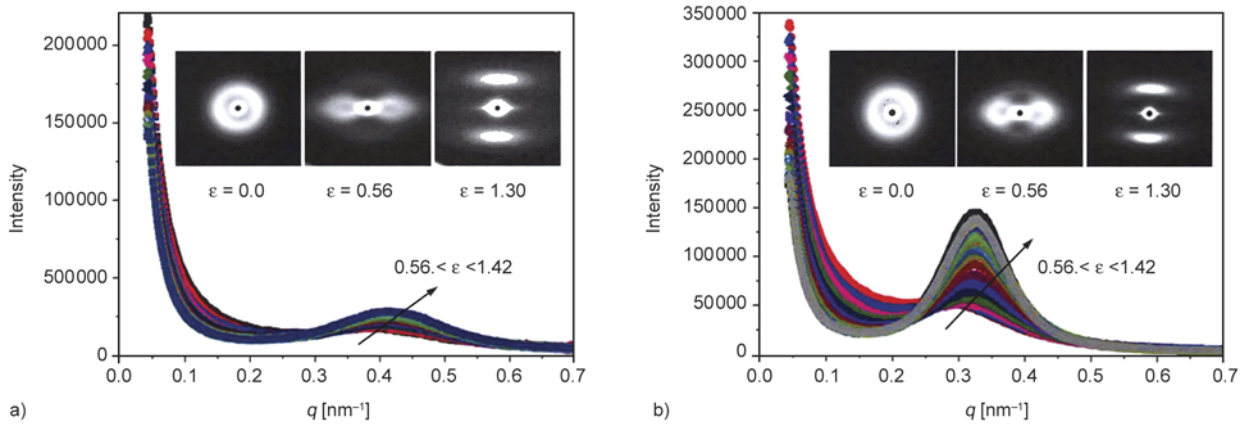

Figure 2. SAXS patterns and meridian intensity profile of quenched PE-A as a function of strain : (a) T_d = 50 °C; (b) T_d =100 °C

with increasing T_d suggesting that the fully orientated structure forms faster at higher T_d. The generation of microfibrils from the crystalline lamella fragmentation should indeed be strongly promoted at higher T_d due to the temperature dependence of the crystal stiffness in the temperature domain of the crystal mechanical relaxation. Besides, at a given T_d, the streak-like scattering intensity strongly increases during elongation due to the gradual conversion of lamellae into microfibrils, and the gradual improvement of orientation as well.

Figure 3 shows L_{pf} as a function of initial L_p for all samples at different T_d. At low T_d, annealed and isotherm samples could not be quantitatively analyzed due to the merging of the intense void scattering onto the microfibrillar scattering. However, more L_{pf} data could be obtained when elevating T_d due to the reduced propensity of the samples for cavitation, as judged from the significant decrease of the scattering about the beamstop (Figure 2).

Figure 3a shows that L_{pf} is generally smaller than the initial L_p indicating dramatic reconstruction of the periodic stacking of amorphous and crystalline phases as a result of the plastic deformation. If considering the SAXS intensity profiles of Figure 2, this phenomenon seems to be rather gradual as a function of increasing strain. In addition, L_{pf} increases with increasing T_d. These findings are in perfect agreement with the melting-recrystallization concept already observed for various semi-crystalline polymers [49–51].

The roughly linear increase of L_{pf} as a function of initial L_p, for every T_d value, may be assigned to the crystallization potential of the various PEs, i.e. a chemical structure dependence including counit content and molecular weight. The chemical structure of the chains indeed governs in a similar way the generation of L_p from the quiescent crystallization in the melt and that of L_{pf} from the strain-induced recrystallization upon drawing.

It appears from Figure 3a that the L_{pf} data at RT (black symbols) are surprisingly close to and even overlap the L_{pf} data at 50 °C (blue symbols). This apparent insensitivity of the fibrillar long period to the draw temperature in the range 25 °C < T_d < 50 °C has been formerly reported by Peterlin and Balta-Calleja for PE materials covering a similar X_c range as the present one and for a similar T_d domain [22]. These authors conjectured that the roughly invariant behavior of L_{pf} for T_d < 50 °C can be assigned to the super-cooling effect consecutive to the strain-induced self-heating and melting of the fibrillated material in the destruction zone during the course of the fibrillar transformation. The reason would be that the crystallization rate turns so high with decreasing temperature that recrystallization of the molten material is almost complete before the actual temperature of the sample reaches the experimental T_d value. It results that L_{pf} gradually turns T_d-independent with decreasing T_d.

Regarding Figure 3b, samples of the same PE material with different crystalline microstructures generated by thermal treatments exhibit very small difference in L_{pf} at given T_d, in the range of experimental accuracy. This finding is an additional evidence of the strain-induced melting-recrystallization process

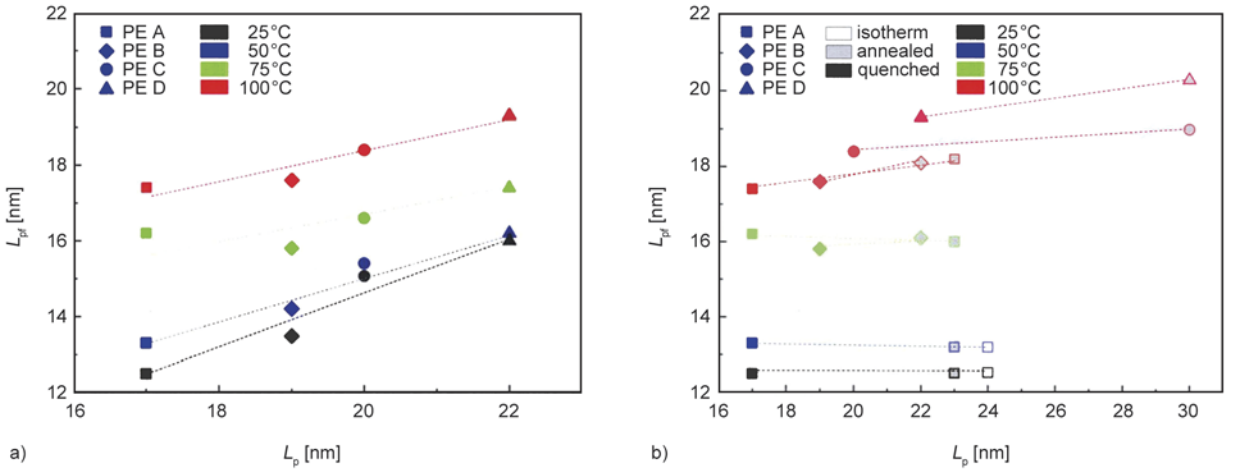

Figure 3. Microfibril long period versus initial L_p at various T_d: (a) influence of chemical structure for quenched samples; (b) influence of thermal treatment (full colors refer to draw temperatures; symbol shapes refer to the various polymers, declining tint of every color refers to thermal treatments)

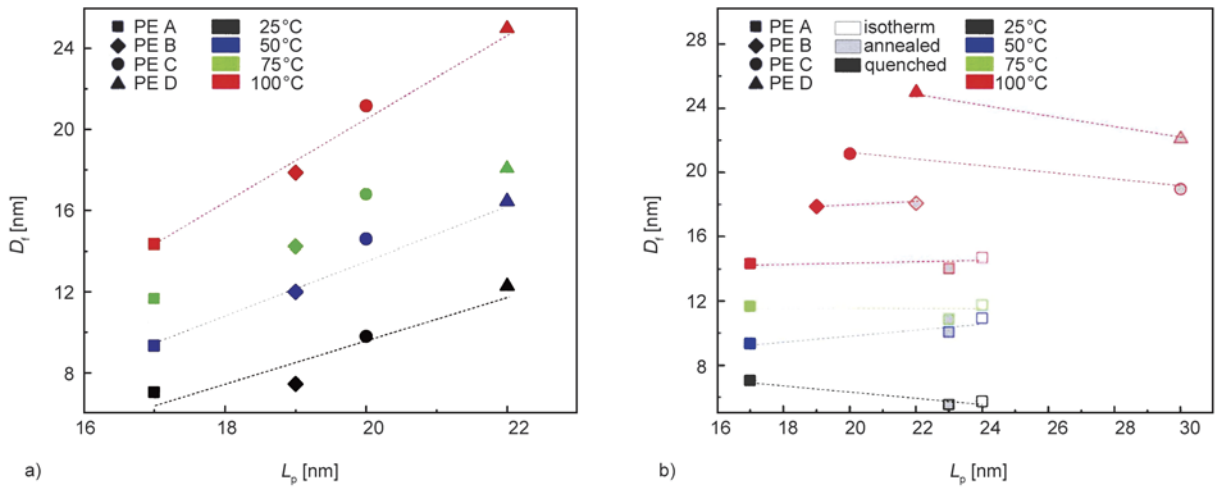

Figure 4. Microfibril diameter versus stacking long period: (a) influence of chemical structure for the quenched samples; (b) influence of thermal treatment

that completely erases the initial crystalline microstructure, from the standpoint of crystal stacking in the microfibrils.

Figure 4 shows the microfibril diameter as a function of long period at different T_d. Similar trends could be obtained if using D_f versus L_p. The D_f values perfectly agree with transmission electron microscopy measurements by Tarin and Thomas for high density PE crystallized from the melt under similar conditions [45]. Furthermore, the D_f data of Figure 4a exhibit a linear variation with L_p at a given T_d, that is an evidence of a chemical structure dependence of D_f similar to that of L_{pf}.

Regarding the D_f evolution with thermal treatment in Figure 4b for a given PE type and for a given T_d, it appears a faint increase with increasing L_p, i.e. from quenched to annealed and isotherm sample. The above observations suggest that D_f is slightly correlated to the initial crystalline microstructure. But the most striking feature of Figure 4 is that D_f is temperature-dependent over the whole T_d range, in contrast to L_{pf} that no longer depends on temperature for $T_d \leq 50$ °C. This latter finding lets us foreseeing that D_f is influenced by the melting-recrystallization process in the same way as L_{pf} is. Notwithstanding no global correlation appears between D_f and L_p which is a parameter characteristic of the initial microstructure.

So an attempt has been made to correlate D_f to a parameter characteristic of the chain topology. Figure 5 shows D_f as a function of the natural draw ratio λ_N which is a macroscopic indicator of the concentration of stress transmitters [*ST*] as deduced from Brown-Huang's model [40, 42]. The reason for

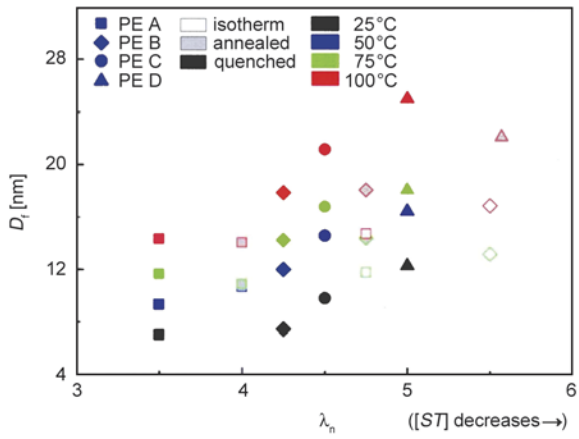

Figure 5. Microfibril diameter versus natural draw ratio at different temperatures

choosing a macroscopic indicator λ_N instead of the actual molecular parameter [*ST*] is that the occurrence of large scale chain rearrangements such as chain reeling together with regular chain-folding during crystallization at high temperature of highly crystalline PEs likely decreases the occurrence of tie chains and chain entanglements. This phenomenon is not taken into account in the [*ST*] computation that is performed in the framework of Fischer's model assuming that the global chain coil conformation of the molten state is preserved in the solid state. This point will be further argued in the *Concluding Discussion*. In contrast, λ_N is an experimental parameter that does account for the topological modifications occurring during crystallization. So only the variation direction of [*ST*] is shown on the *x*-axis of Figure 5 for the sake of the discussion.

Figure 5 shows that, at a given temperature, the D_f data for the samples having the same thermal treat-

ment linearly increase with increasing λ_N and decreasing [*ST*]. This is again in agreement with the chemical structure dependence. Quenched samples exhibit smaller D_f than annealed and isothermal samples. However, D_f shows little if any dependence on thermal treatment for a given PE material. There is again no global correlation between D_f and the topological parameter, λ_N or [*ST*], as it was the case for the structural parameter L_p.

Alternatively, we have tried a mixed correlation with crystalline microstructure and chain topology by using Nitta's parameter, $L_c/[ST]^{0.5}$ [52]. Nitta's approach considers yielding as a fragmentation process, the size of the crystal fragment being basically determined by the average distance between tie chains. These topological features are the locus of stress concentration that initiates the lamella fragmentation. From a mechanical standpoint, the L_c factor in this parameter can be seen as featuring the shear stress to which it is roughly proportional according to the dislocation theory at the onset of the lamellae fragmentation [23]. The $1/[ST]^{0.5}$ factor accounts for the distribution of stress on the lamella surface via the density of the stress transmitters. The unreported data displayed no clear correlation between D_f and $L_c/[ST]^{0.5}$ for the various T_d values of the present experiments. This is in agreement with our previous findings at RT.

Finally a correlation was attempted with the interfacial layer thickness which worked fairly well at RT [37]. Figure 6 shows the D_f versus X_i plots at various T_d. For a given T_d value, all the D_f data fall on the same curve, irrespective of the thermal treatment. Moreover, this finding applies to every temperature, each curve being shifted upward with increasing T_d.

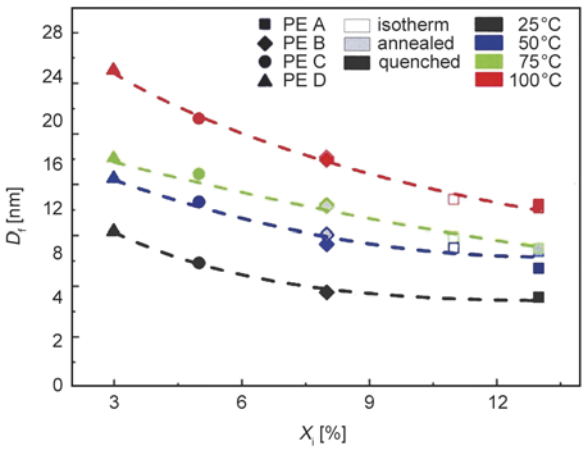

Figure 6. Microfibril diameter versus interfacial layer thickness at different draw temperatures

Worth noticing is that X_i is not much dependent on the thermal treatment, but rather on the chemical structure of the polymer. So that it is not clear whether D_f actually depends on the initial crystalline microstructure and chain topology of the samples via X_i or depends on the chemical structure of the polymer in a similar way as X_i (see Table 1).

4. Conclusions

Two major findings have been disclosed regarding the microfibril structure. First, D_f depends on T_d over the whole temperature range 25 °C < T_d < 100 °C, in strong contrast with L_{pf} that levels off for $T_d \leq 50$ °C. This can be taken as an evidence that the microfibril diameter and long period do not depend in a similar way on the strain-induced melting-recrystallization process. Second, D_f obeys a unique correlation with X_i at every T_d value. This suggests that D_f mainly depends on the mechanism of lamella fragmentation at the onset of yielding, the correlation with X_i being the footprint of the chain topology on the lamella fragmentation process.

However, it is quite surprising that D_f steadily increases with decreasing X_i in parallel to an increase of λ_N as observed in Figure 5. Indeed a greater λ_N value is indicative of a greater drawability of the microfibrils, namely a high potentiality for chain-unfolding. Two mechanisms may be proposed in consideration that high crystallinity PEs develop regular chain-folding during crystallization from the quiescent melt due to the reeling phenomenon. In the case of samples having low X_i that goes along with high crystallinity (Table 2), lamellae may initially break into smaller crystal fragments owing to the high rate of regular chain-folding so that the microfibrils could develop to greater length according to Peterlin's *string of pearls* model. Thereby, their diameter should gradually be reduced at constant crystal volume fraction. Alternatively, the crystal fragments in the protofibrils may display greater capability for chain-unfolding resulting in reduced D_f in the final microfibrils. Both these issues should in principle result in a reduction of D_f which contrasts with the observed increase of D_f.

For reconciling the concomitant increases of D_f and λ_N, one may assume that the chains unfolded during the generation of the microfibrils are able to aggregate onto the lateral surface of the protofibrils. By this process, the final D_f of the microfibrils may grow significantly bigger that the initial D_f of the proto-

fibrils extracted for the fragmented lamellae. Moreover, this process should be more effective for highly crystalline PEs having small co-unit content and high ability for chain unfolding.

This explanation also applies to the observation that D_f increases with increasing T_d at a given X_i value (Figure 6): indeed, the increase of chain mobility with increasing temperature in the present T_d range should promote the gathering of unfolded chains onto the lateral surface of the microfibrils resulting in bigger D_f.

To sum up, the morphogenesis of the microfibrils should be essentially dependent on the chemical structure of the polymer that governs its initial crystallization ability and its chain topology and the various stages of the microfibril construction.

At the light of the present data, Peterlin's scenario for the fibrillar transformation may be modified regarding the morphogenesis of the microfibrils as shown in Figure 7, disregarding the classical plastic processes in the crystal such as crystal shear, phase transition and twinning:

– stage 1: protofibrils are generated like *string of pearls* via fragmentation of lamella stacks and subsequent extraction of the crystal fragments via chain-unfolding from the fracture surfaces of the crystal lamellae. The remaining chain-folded crystal fragments undergo a gradual strain-induced melting owing to the self-heating generated by the plastic work or energy delivered by the partial destruction of the crystals via chain-unfolding. The presence of these remaining chain-folded crystal fragments is due to the more or less irregular chain-topology at the crystal/amorphous interface (X_i) that prevents or at least hinders chain-unfolding. These topologically coherent entities are the ones that preserve the protofibril integrity in spite of strain-induced melting. The protofibril should not be as perfectly oriented as shown on the picture and their uniaxial orientation must develop gradually during the protofibril buildup.
– stage 2: benefiting from the self-heating, the partly molten protofibrils undergo elongation and thinning down thanks to further chain-unfolding up to the natural draw ratio. Then, the chain-unfolding potential of the topologically coherent entities is exhausted. The concomitant strain-hardening entails the stopping of plastic deformation. Self-heating stops and the local drop of temperature enables recrystallization of the protofibrils into incipient microfibrils with new long period. At this stage, incipient microfibrils and protofibrils may coexist for a while.
– stage 3: the completion of recrystallization within the microfibrils together with aggregation and additional crystallization of unfolded chains along the microfibrils finally leads to wider and stable microfibrils. The diameter of the stable microfibrils strongly depends on the material and T_d: the higher are the crystallization potential and T_d, the higher is D_f. An interfibrillar amorphous phase consisting of non-crystallizable unfolded chains should remain due to topological defects such as entanglements and chain defects such as co-units that both prevent the chains to set up in crystallographic register despite good alignment with the microfibrils. This conclusion is consistent with the fact that thermal treatments do not significantly affect D_f.

The question of the long period evolution is somewhat more complex. Figure 3a shows that the fibrillar long period, L_{pf}, is always lower than the initial long period, L_p, in the limits of experimental accuracy. For annealed and isothermal samples, this finding may be rationalized in consideration that the draw temperature, 25 °C < T_d < 100 °C, is always lower than the temperature of thermal treatment, T_c = 122 °C, so that one should expect $L_{pf} < L_p$ after melting-recrystallization (Figure 3b). However, for quenched samples (Figure 3a), it is hardly believable that the structural transformation could occur at a local temperature T_d^* lower than the quenching temperature. This is especially true for T_d = 100 °C. Moreover, self-heating is liable to increase the local temperature T_d^* above the T_d value. Thereby,T_d^* is likely to exceed the T_c of quenched samples so that melting-recrystallization cannot account for the finding $L_{pf} < L_p$.

One may thus propose a complementary mechanism to that of the model of Figure 7. One may consider that the melting point could not be reached during the transformation process, so that crystal *destruction-recrystallization* should be more appropriate than *melting-recrystallization* [11]. This implies that only a part of the crystalline phase should be only concerned by the phenomenon. This part should depend on the sample initial crystalline microstructure and chain topology, and experimental conditions as well.

Figure 8 shows a scenario of microfibril generation based on partial strain-induced crystal destruction-

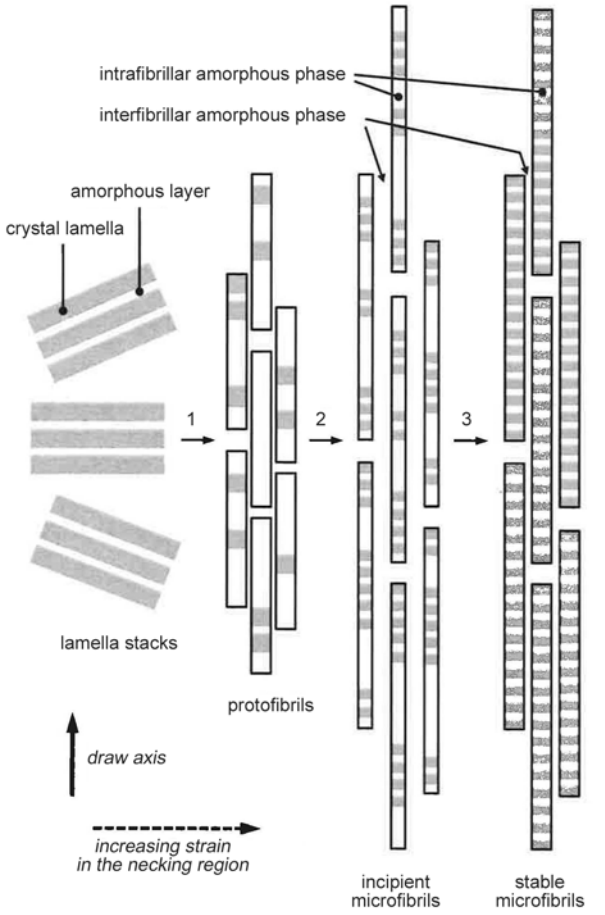

Figure 7. Schematic of the fibrillar transformation upon uniaxial drawing of polyethylene based on Peterlin's model including data from the present study (see text for details)

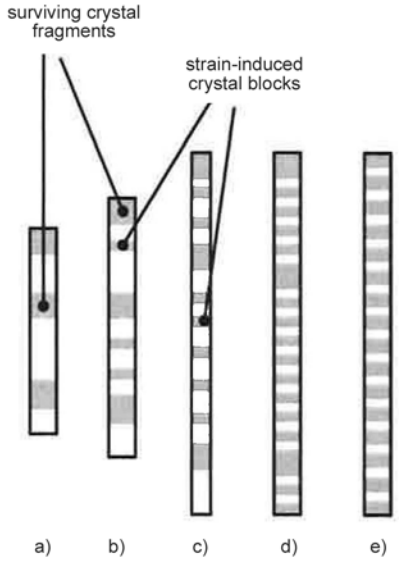

Figure 8. Alternative mechanism of microfibril generation in case of partial strain-induced melting (see text for detail)

recrystallization. This model borrows from Thomas and coworkers observations [45, 53] regarding the fibrillar transformation of high density PE in relation to the chain topology, and the correlation with the natural draw ratio. Protofibrils (a) are first formed by fragmentation of the crystalline lamellae stacks. Then the stretched chains between the crystal fragments (b) in the protofibrils are prone to gradually crystallize benefiting from the strain-induced chain orientation. Then, stretching and self-heating promote chain unfolding and thinning down of the protofibrils (c) that gradually turn into microfibrils thanks to further crystallization and aggregation of unfolded chains (d). By this way, the final average L_{pf} value may be lower than the initial L_p value, although the local T_d^* could be higher than T_c. Besides, the amount of new crystal blocks grown under strain is likely to be lower for high T_d than for low T_d owing to lesser density of critical nuclei. This could explain that L_{pf} is higher at high T_d.

The presence of surviving crystal fragments with different crystal thickness than the strain-induced crystal blocks should disrupt the regular stacking in the microfibrils. As a matter of fact, none of the drawn samples displayed harmonics on the 2-streak SAXS patterns.

The amount of surviving crystal fragments may depend on both the sample initial crystalline microstructure and experimental conditions. High T_d and low initial X_c or L_p are favorable to crystal destruction owing to better chain relaxation in the crystalline phase. However, this quantity is hardly accessible to experiments.

The later refinement of the proposed fibrillar transformation model is perfectly consistent with the observation that L_{pf} turns roughly constant for $T_d \leq 50\,°C$. Indeed, below the temperature of the crystal relaxation, molecular motions in the crystal are prohibited at usual tensile strain rates. Besides, considering that the β-relaxation in high density PE occurs at about –40 °C and the glass transition temperature at –120 °C [54], the molecular motions in the amorphous phase are little affected in the range $-40\,°C < T_d < 50\,°C$. Therefore, the fibrillar transformation process should be practically insensitive to temperature in this T_d range.

Acknowledgements

The authors are indebted to Total-Petrochemicals (Feluy, Belgium) for supplying the polymers and their molecular characteristics. The authors are also grateful to the European Synchrotron Radiation Facility (Grenoble, France) for time allocation on the BM02 beamline.

References

[1] Geil P. H.: Polymer single crystals. Wiley, New York (1973).

[2] Bigg D. M.: A review of techniques for processing ultra-high modulus polymers. Polymer Engineering and Science, **16**, 725–734 (1976).
DOI: 10.1002/pen.760161103

[3] Zachariades A. E., Porter R. S.: The strength and stiffness of polymers. Marcel Dekker, New York (1983).

[4] Ward I. M.: The preparation, structure and properties of ultra-high modulus flexible polymers. Advances in Polymer Science, **10**, 1–70 (1985).
DOI: 10.1007/3-540-15481-7_7

[5] Lewis P. R.: High performance polymer fibres. Rapra, Shawburry (1997).

[6] Eichhorn S., Hearle J. W. S., Jaffe M., Kikutani M. E.: Handbook of textile fibre structure, Vol.1: Fundamentals and manufactured polymer fibres. Woodhead, Cambridge (2009).

[7] Statton W. O.: Polymer texture: The arrangement of crystallites. Journal of Polymer Science Part A: Polymer Chemistry, **41**, 143–155 (1959).
DOI: 10.1002/pol.1959.1204113811

[8] Peterlin A.: Folded chain model of highly drawn polyethylene. Polymer Engineering and Science, **9**, 172–181 (1969).
DOI: 10.1002/pen.760090305

[9] Baltá-Calleja F-J., Peterlin A.: Plastic deformation of polypropylene. Part 2 The influence of temperature and draw-ratio on the axial long period. Journal of Materials Science, **4**, 722–729 (1969).
DOI: 10.1007/BF00742429

[10] Sakaoku K., Morosoff N., Peterlin A.: Drawing of nylon 6 fibers (bristles). Journal of Polymer Science Part B: Polymer Physics, **11**, 31–42 (1973).
DOI: 10.1002/pol.1973.180110104

[11] Peterlin A.: Drawing and extrusion of semi-crystalline polymers. Colloid and Polymer Science, **265**, 357–382 (1987).
DOI: 10.1007/BF01412215

[12] Séguéla R.: Plasticity of semi-crystalline polymers: Crystal slip versus melting-recrystallization. e-Polymers, no.32 (2007).

[13] Wu W., Wignall G. D., Mandelkern L.: A SANS study of the plastic deformation mechanism in polyethylene. Polymer, **33**, 4137–4140 (1992).
DOI: 10.1016/0032-3861(92)90617-6

[14] Annis B. K., Strizak J., Wignall G. D., Alamo R. G., Mandelkern L.: A small-angle neutron scattering study of the plastic deformation of linear polyethylene. Polymer, **37**, 137–140 (1996).
DOI: 10.1016/0032-3861(96)81608-9

[15] Baer R. S., Bolduan O. E. A.: Diffraction by cylindrical bodies with periodic axial structure. Acta Crystallographica, **3**, 236–241 (1950).
DOI: 10.1107/S0365110X50000586

[16] Alexander L. E.: X-ray diffraction methods in polymer science. Wiley-Interscience, New York (1970).

[17] Murthy N. S., Bednarczyk C., Moore R. A. F., Grubb D. T.: Analysis of small-angle X-ray scattering from fibers: Structural changes in nylon 6 upon drawing and annealing. Journal of Polymer Science Part B: Polymer Physics, **34**, 821–835 (1996).
DOI: 10.1002/(SICI)1099-0488(19960415)34:5<821::AID-POLB1>3.0.CO;2-P

[18] Samon J. M., Schultz J. M., Hsiao B. S.: Study of the cold drawing of nylon 6 fiber by in-situ simultaneous small- and wide-angle X-ray scattering techniques. Polymer, **41**, 2169–2182 (2000).
DOI: 10.1016/S0032-3861(99)00378-X

[19] Stribeck N.: Analysis of SAXS fiber patterns by means of projections. in 'Scattering from polymers' (eds.: Cebe P., Hsiao B. S., Lohs D. J.) ACS Symposium Series, Washington Vol 739, 41–56 (2000).
DOI: 10.1021/bk-2000-0739.ch003

[20] Ibanes C., David L., de Boissieu M., Séguéla R., Epicier T., Robert G.: Structure and mechanical behavior of nylon-6 fibers filled with organic and mineral nanoparticles. I. Microstructure of spun and drawn fibers. Journal of Polymer Science Part B: Polymer Physics, **42**, 3876–3892 (2004).
DOI: 10.1002/polb.20217

[21] Peterlin A., Corneliussen A.: Small-angle X-ray diffraction studies of plastically deformed polyethylene. II. Influence of draw temperature, draw ratio, annealing temperature, and time. Journal of Polymer Science Part B: Polymer Physics, **6**, 1273–1282 (1968).
DOI: 10.1002/pol.1968.160060706

[22] Peterlin A., Baltá-Calleja F-J.: Diffraction studies of plastically deformed polyethylene. Kolloid-Zeitschrift und Zeitschrift für Polymere, **242**, 1093–1102 (1970).
DOI: 10.1007/BF02084715

[23] Young R. J.: Dislocation model for yield in polyethylene. Philosophical Magazine, **30**, 85–94 (1974).
DOI: 10.1080/14786439808206535

[24] Bowden P. B., Young R. J.: Deformation mechanisms in crystalline polymers. Journal of Materials Science, **9**, 2034–2051 (1974).
DOI: 10.1007/BF00540553

[25] Kajiyama T., Okada T., Takayanagi M.: The role of mosaic block structure on onset of deformation and fatigue of bulk crystallized polyethylene. Journal of Macromolecular Science Part B: Physics, **9**, 35–69 (1974).
DOI: 10.1080/00222347408204539

[26] Lin L., Argon A. S.: Structure and plastic deformation of polyethylene. Journal of Materials Science, **29**, 294–323 (1994).
DOI: 10.1007/BF01162485

[27] Butler M. F., Donald A. M., Ryan A. J.: Time resolved simultaneous small- and wide-angle X-ray scattering during polyethylene deformation: 1. Cold drawing of ethylene-α-olefin copolymers. Polymer, **38**, 5521–5538 (1997).
DOI: 10.1016/S0032-3861(97)00111-0

[28] Butler M. F., Donald A. M., Ryan A. J.: Time resolved simultaneous small- and wide-angle X-ray scattering during polyethylene deformation – II. Cold drawing of linear polyethylene. Polymer, **39**, 39–52 (1998).
DOI: 10.1016/S0032-3861(97)00226-7

[29] Hiss R., Hobeika S., Lynn C., Strobl G.: Network stretching, slip processes, and fragmentation of crystallites during uniaxial drawing of polyethylene and related copolymers. A comparative study. Macromolecules, **32**, 4390–4403 (1999).
DOI: 10.1021/ma981776b

[30] Nitta K-H., Takayanagi M.: Role of tie molecules in the yielding deformation of isotactic polypropylene. Journal of Polymer Science Part B: Polymer Physics, **37**, 357–368 (1999).
DOI: 10.1002/(SICI)1099-0488(19990215)37:4<357::AID-POLB9>3.3.CO;2-9

[31] Galeski A.: Strength and toughness of crystalline polymer systems. Progress in Polymer Science, **28**, 1643–1699 (2003).
DOI: 10.1016/j.progpolymsci.2003.09.003

[32] Plummer C. J. G.: Microdeformation and fracture in bulk polyolefins. Advances in Polymer Science, **169**, 75–119 (2004).
DOI: 10.1007/b13520

[33] Pawlak A., Galeski A.: Plastic deformation of crystalline polymers: The role of cavitation and crystal plasticity. Macromolecules, **38**, 9688–9697 (2005).
DOI: 10.1021/ma050842o

[34] Séguéla R.: On the natural draw ratio of semi-crystalline polymers: Review of the mechanical, physical and molecular aspects. Macromolecular Materials and Engineering, **292**, 235–244 (2007).
DOI: 10.1002/mame.200600389

[35] Li Y., Iwakura Y., Shimizu H.: Polymer crystallites with few tie molecules from a miscible polymer blend. Macromolecules, **41**, 3396–3400 (2008).
DOI: 10.1021/ma800148x

[36] Schneider K.: Investigation of structural changes in semi-crystalline polymers during deformation by synchrotron X-ray scattering. Journal of Polymer Science Part B: Polymer Physics, **48**, 1574–1586 (2010).
DOI: 10.1002/polb.21971

[37] Humbert S., Lame O., Chenal J-M., Séguéla R., Vigier G.: Memory effect of the molecular topology of lamellar polyethylene on the strain-induced fibrillar structure. European Polymer Journal, **48**, 1093–1100 (2012).
DOI: 10.1016/j.eurpolymj.2012.03.010

[38] Shroff R., Prasad A., Lee C.: Effect of molecular structure on rheological and crystallization properties of polyethylenes. Journal of Polymer Science Part B: Polymer Physics, **34**, 2317–2333 (1996).
DOI: 10.1002/(SICI)1099-0488(199610)34:14<2317::AID-POLB3>3.0.CO;2-T

[39] Hubert L., David L., Séguéla R., Vigier G., Degoulet C., Germain Y.: Physical and mechanical properties of polyethylene for pipes in relation to molecular architecture. I. Microstructure and crystallisation kinetics. Polymer, **42**, 8425–8434 (2001).
DOI: 10.1016/S0032-3861(01)00351-2

[40] Xiong B., Lame O., Chenal J-M., Rochas C., Séguéla R., Vigier G.: Amorphous phase modulus and micro–macro scale relationship in polyethylene *via in situ* SAXS and WAXS. Macromolecules, **48**, 2149–2160 (2015).
DOI: 10.1021/acs.macromol.5b00181

[41] Wunderlich B.: Macromolecular physics, Vol.1: Crystal structure, morphology, defects. Academic Press, New York (1973).

[42] Humbert S., Lame O., Vigier G.: Polyethylene yielding behaviour: What is behind the correlation between yield stress and crystallinity? Polymer, **50**, 3755–3761 (2009).
DOI: 10.1016/j.polymer.2009.05.017

[43] Guinier A., Fournet G.: Small-angle scattering of X-rays. Wiley, New York (1955).

[44] Ward I. M.: Mechanical properties of solid polymers. Wiley Interscience, New York (1980).

[45] Tarin P. M., Thomas E. L.: The role of inter- and intra-links in the transformation of folded chain lamellae into microfibrils. Polymer Engineering and Science, **19**, 1017–1022 (1979).
DOI: 10.1002/pen.760191409

[46] Cazenave J., Séguéla R., Sixou B., Germain Y.: Short-term mechanical and structural approaches for the evaluation of polyethylene stress crack resistance. Polymer, **47**, 3904-3914 (2006).
DOI: 10.1016/j.polymer.2006.03.094

[47] Deblieck R. A. C., van Beek D. J. M., Ramerie K., Ward I. M.: Failure mechanisms in polyolefines: The role of crazing, shear yielding and the entanglement network. Polymer, **52**, 2979–2990 (2011).
DOI: 10.1016/j.polymer.2011.03.055

[48] Xiong B., Lame O., Chenal J. M., Rochas C., Séguéla R., Vigier G.: *In-situ* SAXS study and modeling of the cavitation/crystal-shear competition in semi-crystalline polymers: Influence of temperature and microstructure in polyethylene. Polymer, **54**, 5408–5418 (2013).
DOI: 10.1016/j.polymer.2013.07.055

[49] Men Y., Rieger J., Strobl G.: Role of the entangled amorphous network in tensile deformation of semicrystalline polymers. Physical Review Letters, **91**, 095502/1–095502/4 (2003).
DOI: 10.1103/PhysRevLett.91.095502

[50] Wang Y., Jiang Z., Wu Z., Men Y.: Tensile deformation of polybutene-1 with stable form I at elevated temperature. Macromolecules, **46**, 518–522 (2013).
DOI: 10.1021/ma302389j

[51] Lu Y., Wang Y., Fu L., Jiang Z., Men Y.: Crystallization, recrystallization, and melting lines in syndiotactic polypropylene crystallized from quiescent melt and semicrystalline state due to stress-induced localized melting and recrystallization. Journal of Physical Chemistry, **118**, 13019–13023 (2014).
DOI: 10.1021/jp5093702

[52] Nitta K-H., Takayanagi M.: Tensile yield of isotactic polypropylene in terms of a lamellar-cluster model. Journal of Polymer Science Part B: Polymer Physics, **38**, 1037–1044 (2000).
DOI: 10.1002/(SICI)1099-0488(20000415)38:8<1037::AID-POLB4>3.0.CO;2-R

[53] Adams W. W., Yang D., Thomas E. L.: Direct visualization of microstructural deformation processes in polyethylene. Journal of Materials Science, **21**, 2239–2253 (1986).
DOI: 10.1007/BF01114262

[54] Stehling F. C., Mandelkern L.: The glass temperature of linear polyethylene. Macromolecules, **3**, 242-252 (1970).
DOI: 10.1021/ma60014a023

eXPRESS Polymer Letters Vol.10, No.4 (2016) 324–336
Available online at www.expresspolymlett.com
DOI: 10.3144/expresspolymlett.2016.30

Segmented linear shape memory polyurethanes with thermoreversible Diels-Alder coupling: Effects of polycaprolactone molecular weight and diisocyanate type

Cs. Lakatos[1], *K. Czifrák*[1], *R. Papp*[1], *J. Karger-Kocsis*[2,3], *M. Zsuga*[1], *S. Kéki*[1*]

[1]Department of Applied Chemistry, University of Debrecen, Egyetem tér 1, H-4032 Debrecen, Hungary
[2]Department of Polymer Engineering, Budapest University of Technology and Economics, Műegyetem rkp. 3, H-1111 Budapest, Hungary
[3]MTA–BME Research Group for Composite Science and Technology, Műegyetem rkp. 3, H-1111 Budapest, Hungary

Received 7 September 2015; accepted in revised form 29 October 2015

Abstract. Segmented linear polyurethanes (PUs) containing Diels-Alder (DA) adduct were synthesized in toluene solution from poly(ε-caprolactone) (PCL, M_n = 10, 25 and 50 kg/mol), diisocyanate (methylene diphenyl diisocyanate (MDI), 2,4-toluene diisocyanate (TDI), 1,6-hexamethylenediisocyanate, (HDI)), furfurylamine (FA) and bismaleimide (BMI). The order of the segments in the PUs was -PCL-MDI-FA-BMI-. The PUs were characterized by size-exclusion chromatography (SEC), different spectroscopic (^{1}H-NMR, attenuated total reflectance Fourier-transform infrared, AT-FTIR), thermal and mechanical analysis (differential scanning calorimetry, DSC, dynamical mechanical analysis, DMA). The DA and retro-DA reactions were identified by ^{1}H-NMR for both the synthesized PU and the coupling components (i.e. FA and BMI). Tensile mechanical and shape memory (SM) properties of the PUs were also determined. The DA coupling in the PU was improved by heat treatment above the melting temperature (T_m) of PCL. DMA traces showed a plateau-like region above T_m of PCL confirming the presence of a physical network the netpoints of which are given by the hard segments including the DA couplers. This feature suggested good SM behavior that was confirmed both qualitatively and quantitatively.

Keywords: *smart polymers, polyurethanes, Diels-Alder adduct, mechanical properties, thermal properties*

1. Introduction

Nowadays, thermoplastic or linear polyurethanes (PUs) are produced in large quantities for different applications, such as linear elastomers and foams [1, 2]. Their market penetration is due to their physico-mechanical properties, which can be tailored upon request via their chemical synthesis. Due to their outstanding properties, PUs are widely used in automotive (instrument panel, belt, seals), electric/electronic (cable jacketing, mobile phones), transportation (conveyor belt, tyres), footwear (shoe and shoe sole), medical (catheters) fields, sporting goods, leisure articles (grips) etc. [3–8]. Linear PUs are traditionally produced by reacting diisocyanates (hard segments), long-chain diols of polyesters and/or polyethers (soft segments) and with short-chain diols (so-called chain extenders). These covalently bonded segmented chains undergo phase separation upon cooling from the melt [9]. The resulting morphology is characteristic for traditional thermoplastic elastomers which are 'physically crosslinked'. Moreover, this structure meets the requirements of shape memory polymers (SMPs). SMPs contain 'net points' accounting for shape fixing and reversible 'switches' via which the temporary shaping occurs [10]. In segmented PUs the hard domains form the net points,

*Corresponding author, e-mail: keki.sandor@science.unideb.hu

whereas the soft segment may overtake the switch function. The reversible switch is linked either with the glass transition (T_g) or with the melting temperature (T_m) depending whether the long-chain soft segments are amorphous or semicrystalline [11]. The SM behavior of segmented PUs was early recognized thereby credit should be given to Tobushi *et al*. [12].

Nowadays, already a large body of works addressed the preparation and characterization of shape memory PUs (SMPUs) [13–16]. Research strategies focus now on the creation of multifunctional polymers [17, 18]. As far as SM concerns, attempts are in progress to combine it with self-healing [19]. For self-healing different concepts have been introduced and followed [20]. One of them exploits thermoreversible Diels-Alder (DA) reactions [21, 22]. Due to the thermal reversibility and mild reaction conditions of the Diels-Alder (DA) reaction widely used in the polymer syntheses. The other advantages of this reaction are as follows: both DA and retro-DA (rDA) reaction undergo without catalyst and no byproducts forms. The DA adducts form by the reaction of a conjugated diene and a dienophile at a temperature range from 20 to 90 °C and can be cleaved via rDA reaction above 120 °C [23–27]. The retro reaction, i.e. break-up of the DA adduct, has a very promising additional benefit for linear PUs, namely reduction of the melt viscosity. Low melt viscosity is essential for molded parts having fine surface pattern, long flow routes, or the like. In addition, through DA adducts the degradation behavior of PUs may also be tuned. Therefore, it is of great interest to study the effect of DA adducts in the segmented chain of PUs on their mechanical and shape memory behavior.

This work is aimed at synthesizing various segmented linear PUs containing DA couplings in the main chains and studying their basic mechanical, shape memory and thermomechanical behaviors. Based on our former works [28] poly(ε-caprolactone) (PCL) with different high molecular weights proved to act as an excellent 'switch' in SMPUs [29]. Therefore, for the syntheses of shape memory PUs PCLs with high molecular weights served as diols. As diisocyanates aliphatic and aromatic types have been selected. DA adducts in the main chain were produced by furan-maleimide reaction [23].

2. Experimental section

2.1. Materials

For synthesis of the obtained PUs the following materials were used. As diols PCL (M_n = 10 kg/mol, Sigma-Aldrich Chemical Co (Chemie GmbH, Germany); CAPA® 6250, M_n = 25 kg/mol; CAPA® 6500, M_n = 50 kg/mol, Perstorp Holding AB, Malmö, Sweden) were selected. For the hard segment formation 4,4′-methylene diphenyl diisocyanate (MDI), 2,4-toluene diisocyanate (TDI), 1,6-hexamethylene diisocyanate (HDI) (reagent grades, Sigma-Aldrich Chemical Co (Chemie GmbH, Germany)) served. Furfurylamine (FA) and 1,1′-(methylene di-4,1-phenylene)bismaleimide (BMI) (reagent grade) was purchased from Sigma-Aldrich Chemical Co (Chemie GmbH, Germany). Toluene (analytical grade of Lab-Scan Analytical Sciences, Gliwice, Poland) was distilled over P_2O_5 and stored on sodium wire until use.

2.2. Synthesis of PUs

The PUs differed in the M_n of PCL, type of the diisocyanates and ratio of the components used for their synthesis. PU 1 was produced as described below.

Typical procedure for the synthesis of PU 1: 5.0 g PCL ($5 \cdot 10^{-4}$ mol, M_n = 10 kg/mol) was dissolved in hot toluene 60–80 °C (50 mL) under a nitrogen atmosphere in a 250 mL four-neck flask (equipped with mechanical stirrer, dropping funnel, condenser and nitrogen inlet). Tin(II) ethylhexanoate (reagent grade, Sigma-Aldrich) in 2 mol% amount was used as catalyst. To prepare the prepolymer with isocyanate end groups 0.375 g MDI ($1.5 \cdot 10^{-3}$ mol/5 mL toluene, 3 equiv.) was added to the mixture and reacted for 2–3 hour [h] at 100–110 °C. To form the DA adduct, 0.05 g (49 μL) FA ($1 \cdot 10^{-3}$ mol, 2 equiv.) was added to the isocyanate ended pre-polymer in one portion at 20 °C and heated to 80 °C and kept there for 0.5 h. It was followed by the addition of 0.18 g BMI ($5 \cdot 10^{-4}$ mol, 1 equiv.) at the same temperature and heated at 100–110 °C for 1 h. Accordingly, the composition of this PU 1 is PCL(10)-MDI-FA-BMI/1:3:2:1, where (10) refers to the M_n of PCL in kg/mol unit.

PU 2–PU 10 were synthesized according to the procedure described above except that the amounts of BMI were doubled. The PUs were prepared using the

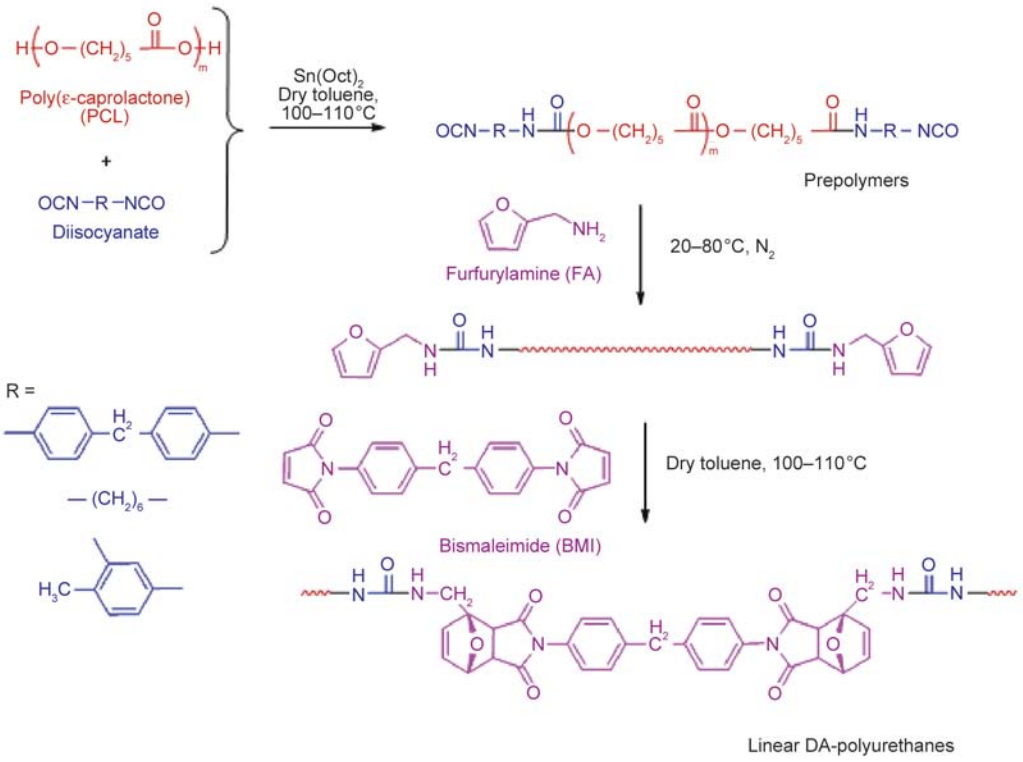

Figure 1. Synthetic pathway for the preparation of DA-adduct containing linear polyurethanes

following compositions: PCL (different M_n)-diisocyanate (MDI, TDI, HDI)-FA-BMI/1:3:2:2. The synthetic pathway of the PUs is summarized in Figure 1.

It is the right place to mention that the above composition ratios were selected according to our experience. During the related works it turned out that the OH/NCO ratio for the prepolymer formation should be preferentially 1:3 [28], corresponding to the above molar ratio, viz. 1:3. During the syntheses the M_n of PCL and the type of the diisocyanate were systematically changed to examine their effects on the properties of the resulting PUs.

Diels-Alder adducts were obtained through the reaction between furan and maleimide groups. The former was obtained by reacting the isocyanate functionalized prepolymer with FA. Coupling of FA end-functionalized polymers with BMI resulted in the formation of DA adducts. Note that no additional chain extending diol was involved in the synthesis. For the syntheses of PU 2 to PU 10 the molar ratio of BMI was raised from 1 to 2, which yielded improved mechanical properties. Yield of the synthesis of the PUs varied between 85 and 98% for this PU series.

The solutions containing the final linear PUs were poured onto Teflon® plates and dried in air resulting in yellow elastic films. Their coding, composition, M_n and Shore A hardness data are listed in Table 1.

2.3. Characterization

Size-exclusion chromatography (SEC) was used to determine the number- and weight-average molecular weight (M_n and M_w, respectively) and thus the polydispersity (M_w/M_n) of the linear PUs prepared. SEC chromatograms were recorded in tetrahydrofuran (THF) at a flow rate of 0.5 mL/min with a Waters chromatograph equipped with four gel columns (4.6×300 mm, 5 μm Styragel columns: HR 0.5, 1, 2 and 4), Waters Alliance e2695 HPLC pump, and with a Waters 2414 refractive index detector, Waters Corp., Milford, MA, USA). SEC was calibrated with polystyrene standards.

^{1}H-NMR spectra were recorded with a Bruker AM 360 (360/90 MHz for ^{1}H/^{13}C) spectrometer (Bruker, Karlsruhe, Germany). Deuterated chloroform was used as solvent. Chemical shifts were referenced to the ^{1}H signal of Me_4Si, that was used as standard. FA and BMI were reacted separately at different temperatures in toluene and their ^{1}H–NMR spectra recorded and analyzed in order to support the proper assignments of the ^{1}H signals of DA adducts in the ^{1}H-NMR spectra of the PUs.

Attenuated total reflectance (ATR) Fourier-transform infrared (AT-FTIR) spectra were recorded on a Perkin Elmer Instruments Spectrum One FTIR spectrometer equipped with a Universal ATR Sampling Accessory (PerkinElmer Inc. Waltham, MA, USA).

The polymer was irradiated by IR beam through a special diamond-zinc-selenium composite prism. The average film thickness of the specimens was ca. 0.5 mm. Four scans were taken for each sample. The spectra were evaluated by Spectrum ES 5.0 program.

Heat treatment of polymers was carried out by hot pressing using 20 bar pressure at 90 °C for 45 min. This treatment was expected to improve the DA coupling in the main chain.

Shore A hardness was measured according to the EN ISO 868 standard with a Zorn type instrument.

Tensile tests were carried out according to the EN ISO 527-1 standard. Computer-controlled Instron 4302 type tensile testing machine (Instron, Darmstadt, Germany), equipped with a 1 kN load cell, was used. At least three dumbbell specimens were cut (clamped length 60 mm) and tensile loaded at a crosshead speed of 50 mm/min. The thickness of the specimens varied between 0.3–1.1 mm.

The thermal properties of the synthesized PUs were examined by Differential Scanning Calorimetry (DSC). DSC tests were carried out in a DSC Q2000 (TA Instruments, Newcastle, DE, USA) equipment operating at 10 °C/min heating rate. Nitrogen flushing was used as protective atmosphere. The weight percentage of the crystalline PCL (C_r) was calculated by Equation (1) [30]:

$$C_r = \frac{\Delta H_m}{\chi_A \cdot \Delta H_m^\circ} \cdot 100 \quad (1)$$

where ΔH_m is the heat of fusion of the investigated PU, χ_A is the weight fraction of PCL in the corresponding PU, ΔH_m° is the heat of fusion of the pure 100% crystalline PCL. For the latter 135.31 J/g has been taken [31].

Dynamic mechanical analysis (DMA) testing of the PUs was carried out in DMA Q800 device of TA Instruments (Newcastle, DE, USA). DMA traces were monitored in tension mode (dimension of the specimens: length: 25 mm, clamped length: 12 mm, width: 7 mm, thickness: ca. 0.5 mm) at an oscillation amplitude of 0.2% setting a frequency of 1 Hz and a static load of 1 N. The temperature was varied between –10 and 130 °C with a heating rate of 3 °C/min.

Shape memory properties were evaluated in tensile mode using the above DMA device. The specimens (clamped length×width×thickness = ca. 12×7×0.5 mm) were stretched after 10 min holding at 80 °C at a strain rate of 40%/min, followed by cooling quickly the specimen to 20 °C. The stress was then released and the shape fixity (R_f) determined. Shape recovery (R_r) was measured at 0.1 N loading of the specimens (quasi free recovery) by reheating the specimens at 1 °C/min heating rate from 20 to 80 °C and holding there for 10 min. The shape fixity (R_f) and shape recovery ratios (R_r) are defined as by Equations (2) and (3):

$$R_f[\%] = \frac{l_d - l_0}{l_{80\%} - l_0} \cdot 100 \quad (2)$$

$$R_r[\%] = \frac{l_d - l_f}{l_d - l_0} \cdot 100 \quad (3)$$

where l_d – the sample length after removal of the tensile load during shape fixing at 20 °C, l_0 – the clamped length of the sample at 20 °C, $l_{80\%}$ – the length after tensile stretching for 80%, and l_f – the final recovered length of the stretched specimen.

3. Results and discussion

3.1. Molecular characteristics of the linear PUs

According to Figure 1, linear segmented PUs, composed of soft segment PCL with varying M_n, hard segment diisocyanate (MDI, HDI, TDI) and the DA coupling (by reacting the furan of FA and BMI), were produced. The compositions of PUs synthesized PU 1 to PU 10 are listed in Table 1. All PUs were highly ductile materials with rather high Shore A hardness.

The SEC traces of the starting PCLs and the synthesized linear PUs 1–10 are shown in Figure 2. The SEC traces of the synthesized PUs appeared at lower retention volumes (i.e., at higher M_n) than those of the starting PCLs, supporting a successful coupling.

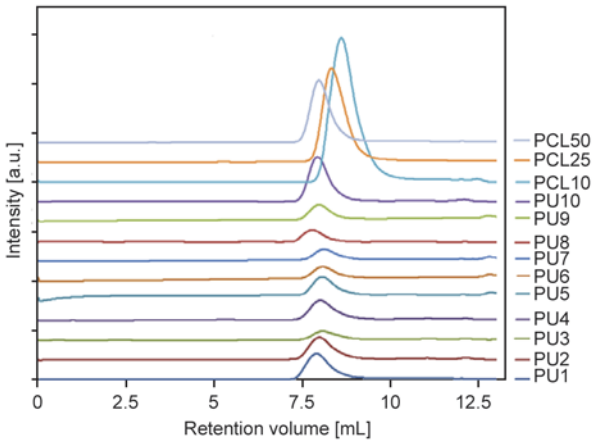

Figure 2. SEC traces of starting PCLs and the synthesized PUs 1–10

Table 1. Composition and basic molecular characteristics of the linear PUs synthesized

Code	Composition/monomer ratio	M_n [kg/mol]	M_w/M_n	Shore A hardness
	PCL(10)	10.4	1.60	–
	PCL(25)	23.2	1.80	–
	PCL(50)	51.9	1.80	–
PU 1	PCL(10)-MDI-FA-BMI/1:3:2:1	76.0	1.95	94
PU 2	PCL(10)-MDI-FA-BMI/1:3:2:2	66.4	1.90	95
PU 3	PCL(10)-HDI-FA-BMI/1:3:2:2	53.6	1.90	81
PU 4	PCL(10)-TDI-FA-BMI/1:3:2:2	57.0	2.00	84
PU 5	PCL(25)-MDI-FA-BMI/1:3:2:2	67.3	1.60	96
PU 6	PCL(25)-HDI-FA-BMI/1:3:2:2	67.2	1.60	94
PU 7	PCL(25)-TDI-FA-BMI/1:3:2:2	61.6	1.60	90
PU 8	PCL(50)-MDI-FA-BMI/1:3:2:2	116.7	1.60	92
PU 9	PCL(50)-HDI-FA-BMI/1:3:2:2	95.9	1.50	94
PU 10	PCL(50)-TDI-FA-BMI/1:3:2:2	85.8	1.70	90

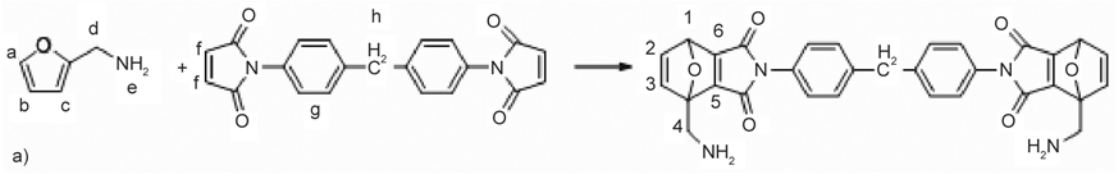

a)

Compound	Protons	δ [ppm] in $CDCl_3$
FA	a	7.35
	b	6.31
	c	6.12
	d	3.82
	e	1.45
BMI	f	6.84
	g	7.31–7.26
	h	4.03
DA adduct	1 endo	5.36
	1 exo	4.53
	2.3 exo, endo	6.58–6.22
	4 endo, exo + h	4.01–3.90
	endo exo	
	5 endo	3.33
	6 endo + 5 exo	3.15–3.00
	6 exo	2.65

b)

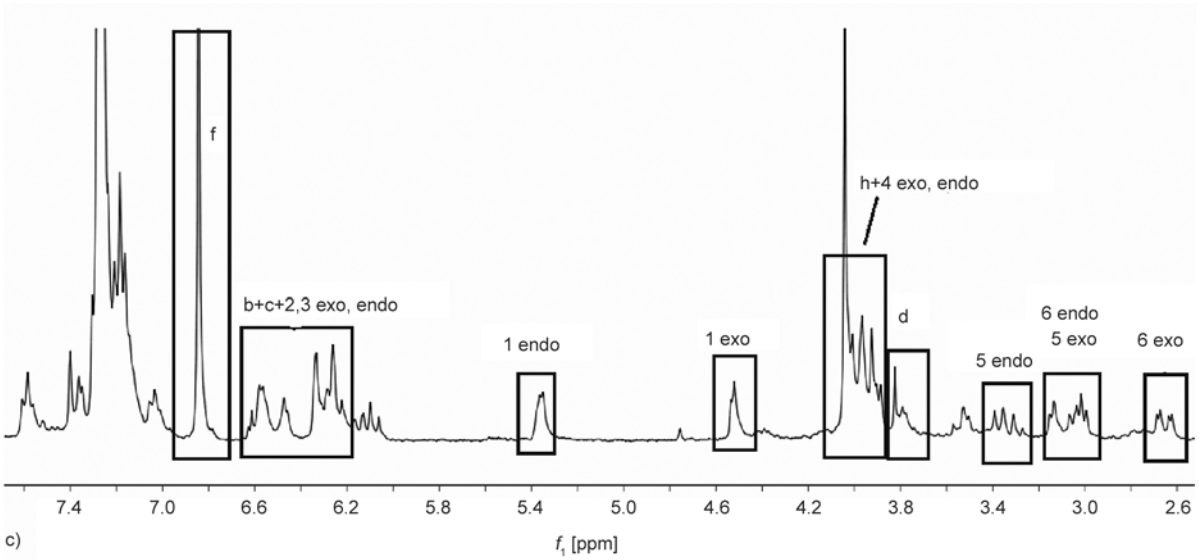

c)

Figure 3. Proton assignments of FA, BMI and the corresponding DA adduct (a, b) and a representative ^{1}H-NMR spectrum of DA reaction between FA and BMI at 25 °C (c)

The M_n and polydispersity (M_w/M_n) values, obtained from SEC measurements, are compiled in Table 1. M_n values of the DA adduct containing linear PUs with PCL of M_n = 10 kg/mol (PUs 1–4) are between 53.6 and 76 kg/mol. This suggests the formation of PU chains containing 5–7 PCL units. In contrary, PUs 5–7 with PCL of M_n = 25 kg/mol includes 2 PCL units based on the measured M_n values (61.6–67.3 kg/mol). Similar amount (i.e. 2 units) of PCL (according to the measured M_n values (85.8–116.7)) may be incorporated in PUs 8–10 containing PCL of M_n = 50 kg/mol. The polydispersity changed within a narrow range (cf. Table 1).

Comparing PUs 5–7 and PUs 8–10, where the coupling diisocyanates were different the M_n decreased according to the order MDI > HDI > TDI. This tendency is more pronounced for the PUs containing PCL with the highest M_n (PU 8–10) than for the series with M_n = 25 kg/mol PCL (PU 5–7). However, incorporation of HDI resulted in the lowest M_n value (53.6 kg/mol) for PUs 2–4. In addition, as general trend it can be established that MDI provided PUs with the highest M_n.

To identify the proton signals of the DA adducts in the ^{1}H-NMR spectra of linear PUs, first the reaction of unprotected FA and BMI was studied as model reaction. FA and BMI were reacted at 25, 60, 100 and 120 °C for up to 23 h in dry toluene. Figure 3 illustrates the composition of the reaction mixture after 1 hour at 25 °C. The distinct peaks at δ = 6.84, 4.03 ppm are assigned to protons **f** and **h** of BMI while peak at 3.82 ppm belongs to proton **d** of FA. New chemical shifts at δ = 6.58–6.22, 5.36, 4.53, 4.01–3.90, 4.33 and 2.65 ppm can be assigned to the protons 1–6 of DA adduct. Considering the nature of DA reaction *exo*- and *endo*-adducts may be formed, the ratio of *exo*- to *endo*-adducts changed with the temperature and the reaction time.

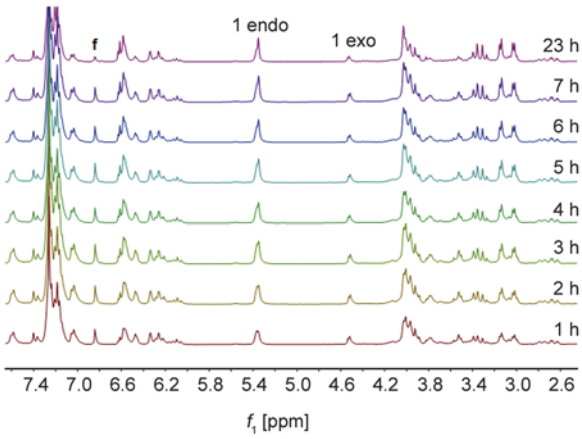

Figure 4. Superimposed ^{1}H-NMR spectra of DA reaction between FA and BMI at 60 °C

Figure 4 shows the superimposed proton NMR spectra of FA, BMI and the DA adduct formed from them at 60 °C. As seen in Figure 4 the amount of the *endo* to that of *exo* DA adduct increases with conversion. The data of Table 2 show the effects of reaction temperature and time on the formation of the DA adducts (*endo*+*exo*; unreacted). Based on the integrals of protons **f** and 1 after 23 h the conversion was 84%, while at 100 °C after 23 h the reaction almost completed. As it can be seen from these results, the DA addition reaction takes place already at room temperature with moderate conversion: i.e. the amount of the DA adducts is 54% after 23 h at ambient temperature. Upon raising the reaction temperature the conversion increases. Further increase in the temperature (120 °C) induces the rDA reaction since proton signals of the starting materials reappear in the ^{1}H-NMR spectra.

To support the proposed structure presented in Figure 1, the ^{1}H-NMR spectrum of PU 5 will be shown

Table 2. Composition of the reaction mixture at 25, 60, 80, 100 and 120 °C based on ^{1}H-NMR spectra

Temperature [°C]	Starting material							
	% (1h)	% (2h)	% (3h)	% (4h)	% (5h)	% (6h)	% (7h)	% (23h)
25	83	85	87	85	84	81	80	45
60	31	30	28	27	28	26	21	16
80	36	36	37	37	36	36	35	30
100	29	28	25	29	28	26	32	2
120	13	13	22	16	24	23	21	5
	Product							
	% (1h)	% (2h)	% (3h)	% (4h)	% (5h)	% (6h)	% (7h)	% (23h)
25	17	14	12	14	15	19	19	54
60	68	69	71	73	71	74	78	84
80	64	64	64	64	64	64	65	69
100	71	72	75	71	72	74	68	98
120	88	70	78	84	76	77	79	95

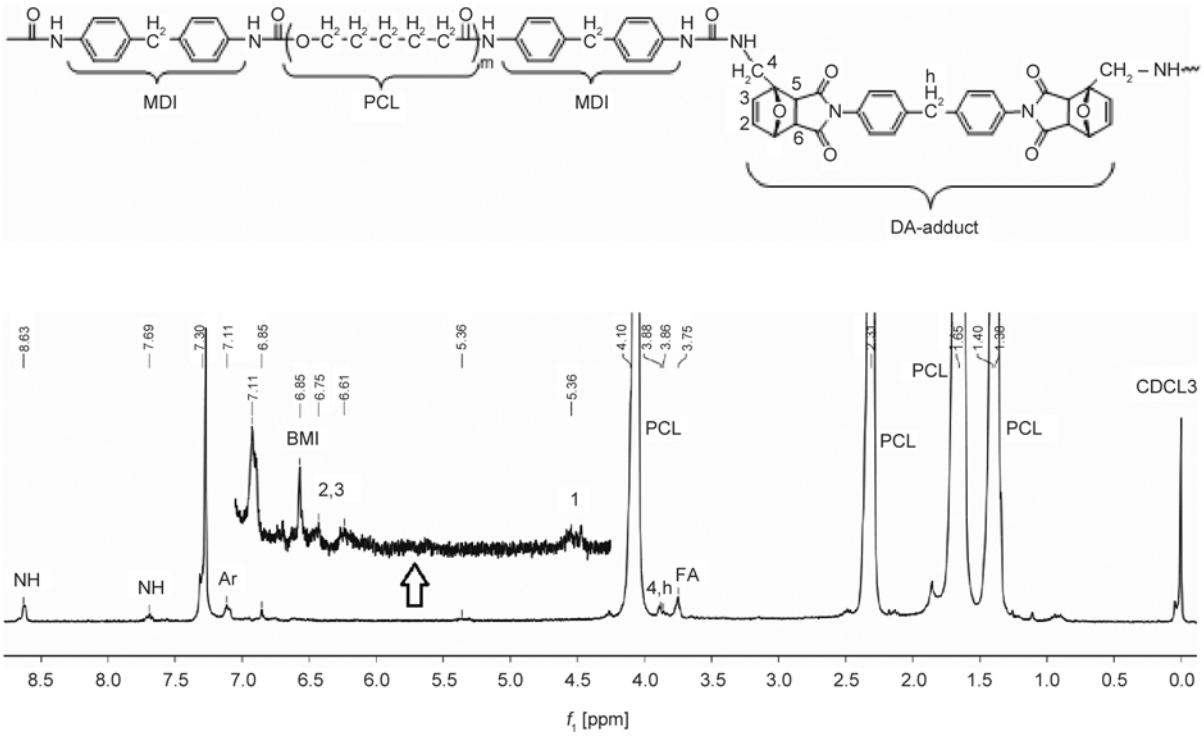

Figure 5. Structure and ^{1}H-NMR spectrum of PU 5

and analyzed next. The amide, urethane or urea NH protons (**f**) of PU-5 appear in Figure 4 at 8.63, 7.69 ppm, while the aromatic signals (MDI) are visible at 7.30, 7.11 ppm. The protons (**f** and **d**), which belongs to the components of DA adduct, can be found at 6.85 (BMI) and 3.75 (FA) ppm, respectively. The low intensity peaks of the adduct (1–3) are visible in the magnified insets at 6.75, 6.61 and 5.36 ppm. The CH_2 proton signals of PCL are around 4.06, 2.31, 1.72-1.62 and 1.38 ppm (cf. Figure 5).

The DA and rDA reactions were also studied by ^{1}H-NMR spectroscopy (PU 1, Figure 6). The DA reaction was induced at 100 °C by addition FA and BMI (2) to the isocyanate terminated prepolymer (1), while the cleavage of the DA adduct was followed at 125 °C for 2 h (3). The peaks at 6.85, 3.88 ppm belong to FA and BMI, while those at 6.73 and 6.57 ppm are assigned to CH protons of the DA adduct. In the ^{1}H-NMR spectrum (3) the peaks of BMI and the DA adduct are not visible, only the low intensity peaks (6.31, 6.23 ppm) of FA appear at 3.68 ppm (Figure 6).

In order to study how the heat treatment influences the properties of the PUs via completion of the DA reaction PU 2 was heated at 90 °C for 45 min in a hot press. The corresponding ^{1}H-NMR spectra are shown in Figure 7.

The increasing intensities of the signals related to the DA adduct at 6.72, 6.55, 5.36, 3.13 and 3.02 ppm,

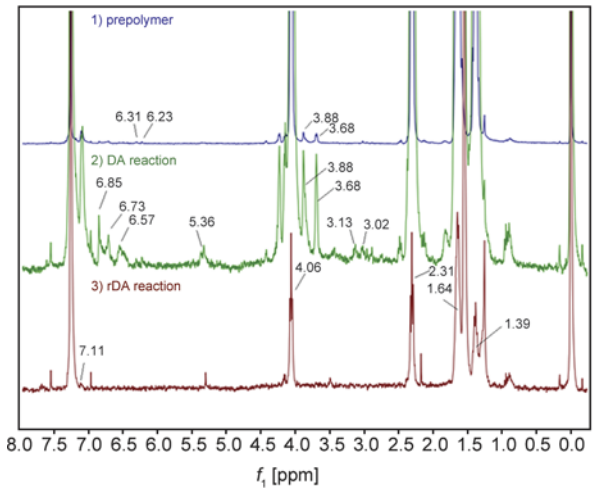

Figure 6. Investigation of the DA and rDA reaction by ^{1}H-NMR spectroscopy in the case of PU 1

confirm that the additional thermal treatment improved DA coupling.

Further information on the chemical structure of the linear PUs was expected from AT-FTIR measurements. Figure 8 shows the IR spectra of PUs 2, 5–8. The absorption bands belonging to amide bonds –NH and amide II, are not visible in the FTIR spectra of PUs. The absorption bands at 2860, 2935 cm^{-1}, associated with –CH_2 vibrations, are well identifiable. Nevertheless, no absorption band could be resolved around 2230 cm^{-1}, indicating the complete reaction

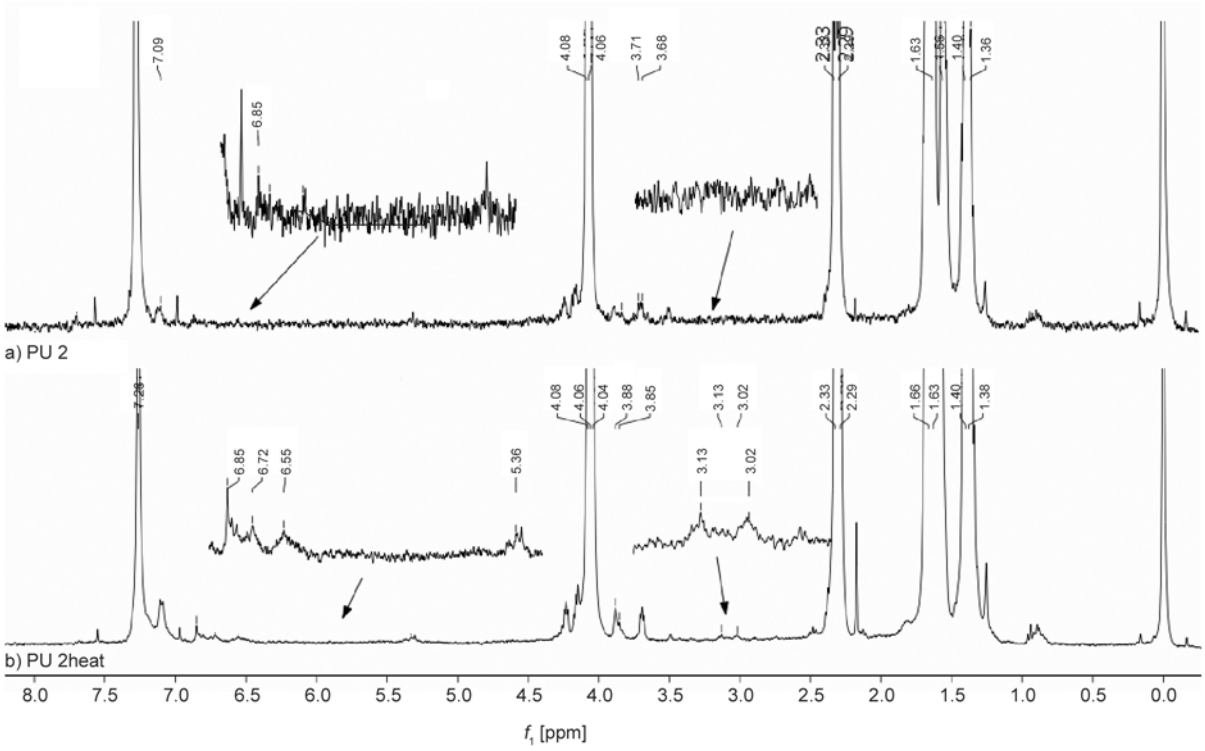

Figure 7. [1]H-NMR spectra of PU 2 with heat treatment at 90 °C for 45 min (b) and without heat treatment (a)

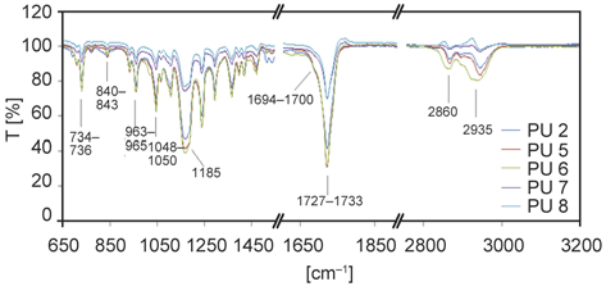

Figure 8. AT-FTIR spectra of PUs 2 and 5–8

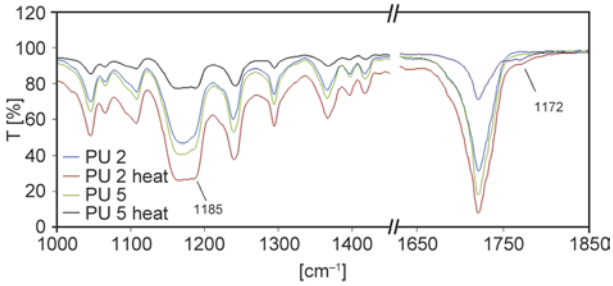

Figure 9. Comparison of the AT-FTIR spectra of PU 2 and 5 with and without thermal treatment at 90 °C for 45 min

of the NCO functional groups. The band appearing at 1185 cm^{-1} can be assigned to =C–O and –C–O–C– groups (Figure 8). In the structures of segmented PUs the urethane and amide NH groups act as H-bond donors, while the C=O groups in the PCL segments and urethane bonds overtake the role of H-bond acceptors [32, 33]. The H-bonded structure may influence numerous properties of the PU including e.g. the crystallization process. The presence of bond –N–H···O=C can be demonstrated by AT-FTIR. As seen in the enlargement of C=O band (Figure 8), the free C=O band reflecting the ester (PCL) and urethane C=O appears around 1727–1733 cm^{-1}, whereas the H-bonded C=O is reflected by a weak shoulder between 1694–1700 cm^{-1}. The PUs 2 and 5 were also investigated by IR spectroscopy before and after heat treatment. Our observations confirm also that additional DA reaction takes place upon heating, which is in good agreement with [1]H-NMR results (see Figure 7). So, the applied heat treatment supported additional DA adduct formation.

Figure 9 reveals the FTIR spectra of PU 2 and 5 with and without additional heat treatment. In the IR spectra of heat treated PUs a band is visible at 1772 cm^{-1} (C=O) and the increasing intensity of peak at 1185 cm^{-1} refers to an additional formation of DA-adduct [33]. The results of [1]H-NMR and AT-FTIR investigations indicate that the DA reaction in the case of high molecular weight PUs takes place at lower conversion than in the model reaction between FA and BMI. However, the DA conversion can be further enhanced by heat treatment.

3.2. Tensile mechanical behavior

The mechanical properties were examined by tensile measurements and the results are summarized in Table 3. Comparing PU 1 and 2 one can recognize that increasing the BMI amount in the composition was accompanied with decreasing the stiffness (*E*-modulus), strength (maximum and stress at break, σ_m and σ_R, respectively) and ductility (elongation at maximum stress and ultimate elongation, ε_m and ε_R, respectively) characteristics.

PCL (10 kg/mol) combined with MDI showed good mechanical properties (PUs 1 and 2), the tensile strength (σ_R) 18 and 19 MPa. Applying HDI and TDI instead of MDI (PU 3, 4), PUs with poorer mechanical properties were obtained, which can be attributed to the decreasing molecular weight of the corresponding PUs (see Table 1.) In the series of PUs 5–10 containing PCL of M_n = 25 and 50 kg/mol (PUs 6 and 9) PCLs resulted in polymers with the highest tensile strength (σ_R) 22 and 25 MPa and elongation (ε_R) 619 and 580%. This may be due to the higher flexibility provided by HDI. However, it should be noted that the *E*-modulus increased, which may be linked with a higher secondary bond (H-bonds, Van der Waals interactions) density. Considering the HDI containing PU series, i.e., PUs 3, 6 and 9, one can observe that the stiffness, strength and ductility data steeply increase with increasing molecular weight of the PCL from M_n = 10 kg/mol to 25 kg/mol. However, incorporation of PCL with M_n = 50 kg/mol resulted in a small drop in each of the above mechanical parameters. In contrast, for the TDI series a different scenario can be observed. Unlike PUs 4 and 10 having the lowest and highest M_n of PCL incorporated into the chain, poor mechanical data were found for PU 7 containing PCL with M_n = 25 kg/mol. The best mechanical performance can be attributed to the MDI series of the PUs (PU 2, 5 and 8), especially when they contained PCLs with M_n = 10 and 25 kg/mol as soft segments (PU 2 and 5). Therefore, these polymers were studied with respect to shape-memory properties.

Table 3. Tensile mechanical properties of the PUs (PUs 1–10). Designations: *E*-elastic modulus (Young's modulus), σ_m – maximum stress, ε_m – elongation at the maximum stress, ε_R – is the ultimate elongation, and σ_R – is the stress at break

Code	*E* [MPa]	ε_m [%]	σ_m [MPa]	ε_R [%]	σ_R [MPa]
PU 1	360±9	490±4	18±0.6	490±4	18±0.6
PU 2	179±22	778±9	19±0.7	778±9	19±0.7
PU 3	113±15	165±76	9±0.5	165±76	9±0.5
PU 4	162±11	175±55	9±1.0	175±55	9±1.0
PU 5	179±36	695±107	15±4.0	695±107	15±4.0
PU 6	383±21	619±23	25±0.4	619±23	25±0.4
PU 7	145±66	16±5	6±2.0	26±8	5±0.6
PU 8	174±34	75±45	9±0.7	160±45	10±2.0
PU 9	285±26	580±63	22±0.1	580±63	22±0.1
PU 10	235±41	102±30	13±1.0	102±30	13±1.0

3.3. Thermal, thermo-mechanical and shape memory behavior

DA adduct formation provides a reversible linkage between the PCL-based prepolymers thereby enhancing the molecular weight of the resulting PU. Longer chains participate in more molecular entanglements and affect the final morphology (physical crosslink structure), which may be associated with better SM performance. Furthermore, DA adducts may overtake the role of reversible 'switch' in SMPUs, as well. However, as underlined before, the reversible main 'switch' function of this series of SMPUs is due to the melting and crystallization of the PCL segments. On the other hand, the DA bonding between the furan and maleimide may influence the crystallization of PCL and thus affect the shape memory properties. For this reasons, the crystallization behavior of PCL in selected PUs (PUs 1–3, 5, 6, 8 and 9) was investigated by DSC (see Figure 10). The data obtained from the DSC curves and the calculated crystallinity values are summarized in Table 4.

As shown in Figure 10 only the melting peaks of PCL were detected by DSC measurements. No thermal effects belonging to the DA adducts appeared in the DSC curves. The latter, might be hidden by the PCL melting. Furthermore, the crystallinity of polyurethanes can be influenced by the length of the soft segment and the amount of hard segment [34]. Considering PUs 1 and 2 the higher BMI amount seems

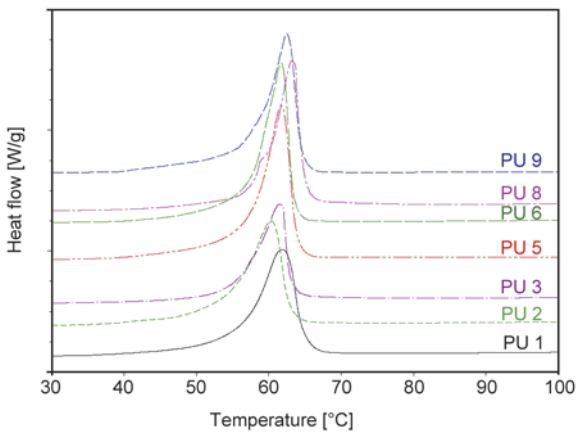

Figure 10. DSC curves of PUs 1–3, 5, 6 ,8 and 9

Table 4. Melting temperature (T_m), melting enthalpy (ΔH_m) and crystallinity values obtained from DSC measurements

Code	PCL M_n [kg/mol]	T_m [°C]	PCL [wt%]	ΔH_m [J/g]	Crystallinity [%]
PU 1	10	61.8	88.5	74.6	62.0
PU 2	10	60.3	86.0	65.6	56.5
PU 3	10	61.4	90.0	49.9	41.0
PU 5	25	61.6	94.0	85.8	68.0
PU 6	25	61.8	95.0	78.7	61.5
PU 8	50	63.1	97.0	66.7	51.0
PU 9	50	62.5	97.0	81.2	62.0

to reduce the crystallinity thereby lowering T_m, as well. With the increasing M_n of PCL, the PCL crystallinity shows maximum for the MDI series (cf. PU 2, 5, and 8 in Table 4). Based on these results PU 5 has the highest crystallinity, which may explain the better shape memory properties. No change in the crystallinity was detected, when the M_n of PCL was increased for the HDI containing PUs (cf. PU 6 and 9 in Table 4). However, the crystallinity of the PU decreased, when the main segment was PCL with M_n = 10 kDa (PU 3). The reason for this may be linked with the flexibility of HDI.

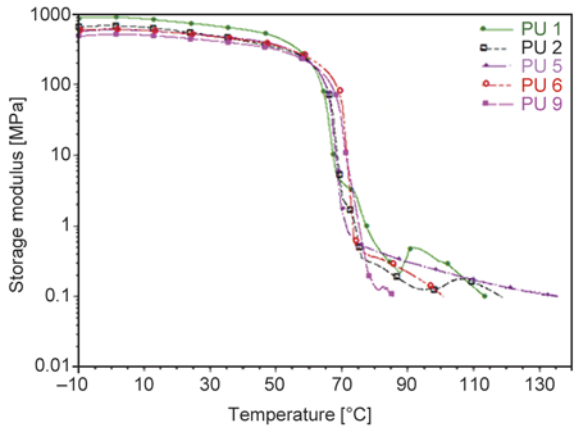

Figure 11. Storage modulus as a function of temperature for PUs 1, 2, 5, 6 and 9

Thermal stability and shape memory properties of PUs were analyzed by dynamic mechanical analysis (DMA) using tensile mode. Storage modulus of PUs 1, 2, 5, 6 and 9 as a function of temperature are shown in Figure 11. The DMA curves exhibit rubbery-like plateau above T_m of the PCL for PU 1, 2, 5 and 6. No such feature could be detected for PU 9. The term rubbery-like is used due to some analogy with the rubbery plateau in crosslinked polymers. The fact that it is declining with increasing temperature is a confirmation for the presence of a segregated morphology in the physically networked thermoplastic PUs. Nevertheless, the presence of this plateau is an excellent tool for SM programming [35]. In the DMA traces of PUs 1 and 2, containing PCL of M_n = 10 kg/mol, additional peaks can be found in this rubber-like plateau region. These additional peaks may be due to the microstructure of the PUs and/or to the advancement of the DA coupling which was also confirmed by ^{1}H-NMR and AT-FTIR spectroscopy. PUs 2 and 5 showing well developed rubbery-like plateaus were subjected to SM tests. First thin strips cut of PU 2 and 5 were tested for shape memory performance (Figure 12). The samples were deformed at 70 °C (i.e. above the melting temperature of PCL block) in water bath and then cooled to room temperature to set the temporary shape. Its re-immersion in the warm water bath resulted in the expected shape recovery.

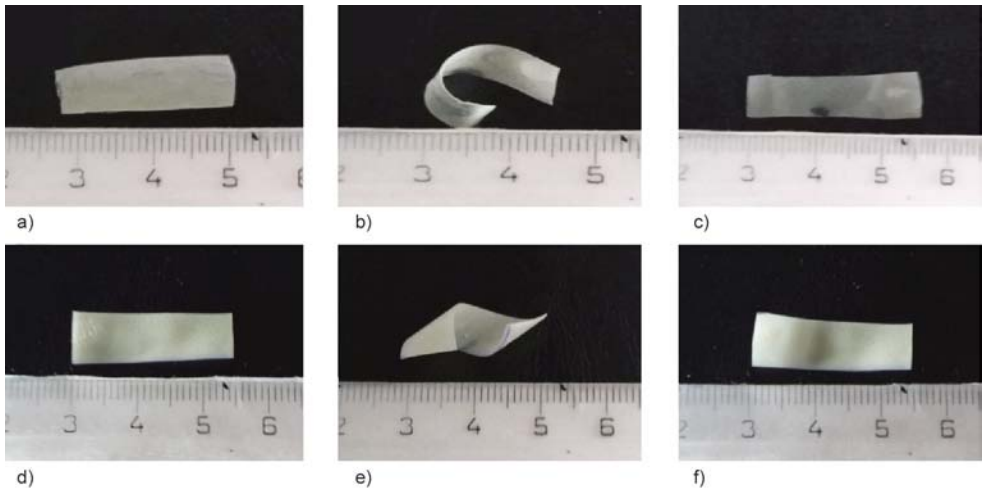

Figure 12. Illustration of the shape memory behavior for PU 2 (a–c) and PU 5 (d–f): a, d) permanent, b, e) temporary, c, f) recovered shape

The SM behavior was quantified in tensile loading using the DMA device. PUs 2 and 5 had similar shape fixities (R_f = 99 and 100%, respectively) after deformation at 80 °C for 80% strain. The shape recovery of PU 5 at 80 °C (R_r = 56%) was higher than the PU 2 version containing PCL with M_n = 10 kg/mol (R_r = 43%). The reason for this is most likely linked with the difference in the main segments' molecular weights, viz. PCLs with 25 and 10 kg/mol. Thus PU 2 has lower crystallinity and reduced elasticity which affect negatively the shape recovery. It is supposed, however, that R_r changes as a function of the shape programming, i.e. temperature and strain values. It is noteworthy that due to rubber-like behavior and the thermoreversible feature of the DA coupling, these PUs may show shape memory assisted self healing [36, 37] that will be checked next.

4. Conclusions

DA reaction was applied for the preparation of thermoreversible bond containing linear segmented polyurethanes (PUs). The soft segments composed of poly(ε-caprolactone) (PCL) with different molecular weights (M_n = 10, 25 and 50 kg/mol), while the hard segments were three types of diisocyanates (4,4′-methylene diphenyl diisocyanate (MDI), 2,4-toluene diisocyanate (TDI), 1,6-hexamethylene diisocyanate (HDI)), furfurylamine (FA) and 1,1′-(methylene di-4,1-phenylene)bismaleimide (BMI). The molecular weight of the linear PUs was determined by size-exclusion chromatography (SEC) and varied from 53.6 to 116.7 kg/mol. It was demonstrated that heat treatment close to the melting temperature (T_m) of PCL supported the DA reaction. The PCL-related crystallinity of the PUs changed slightly as a function of PCL molecular weight and diisocyanate type. This was attributed to the effects of H-bonding and characteristics of the hard segments formed. MDI and HDI outperformed the TDI-containing PUs with respect to the mechanical performance irrespective of the PCL molecular weight. The stiff molecular structure of MDI proved to be beneficial for the mechanical performance of PUs with PCL of 10 kg/mol molecular weight, while the more flexible HDI worked well in the PUs with higher molecular weight PCL (50 kg/mol). Above T_m of the PCL a well-developed rubber-like plateau was found attesting the efficient physical networking via the hard segments composed of isocyanates and DA adducts. This plateau range allows to set different programming for shape memory function that was shown on selected examples. The good recovery along with the thermoreversible feature of the DA adducts are prerequisites of shape memory assisted self-healing which, however, still has to be confirmed.

Acknowledgements

The work reported here was supported by the TÁMOP-4.2.2.A-11/1/KONV-2012-0036 project, co-financed by the European Union and the European Social Fund, and by a grant of the Hungarian Research Funds (OTKA SNN 114547). This work was also supported by the European Union and the State of Hungary, co-financed by the European Social Fund in the framework of TÁMOP-4.2.4.A/ 2-11/1-2012-0001 'National Excellence Program' (S. K.).

References

[1] Sonnenschein M. F.: Polyurethanes-science, technology, markets, and trends. Whiley, New York (2015).

[2] Smirnova N. N., Kandeev K. V., Markin A. V., Bykova T. A., Kulagina T. G., Fainleib A. M.: Thermodynamics of linear polyurethanes on basis of 1,4-diisocyanatobutane with 1,4-butanediol and 1,6-hexanediol in the range from $T \rightarrow 0$ to 490 K. Thermochimica Acta, **445**, 7–18 (2006).
DOI: 10.1016/j.tca.2006.03.017

[3] Chattopadhyay D. K., Raju K. V. S. N.: Structural engineering of polyurethane coatings for high performance applications. Progress in Polymer Science, **32**, 352–418 (2007).
DOI: 10.1016/j.progpolymsci.2006.05.003

[4] Shmidt R. S.: NASA pressure-relieving foam technology is keeping the leading innerspring mattress firms awake at night. Technovation, **29**, 181–191 (2009).
DOI: 10.1016/j.technovation.2008.06.004

[5] Ippili R. K., Davies P., Bajaj A. K., Hagenmeyer L.: Nonlinear multi-body dynamic modeling of seat–occupant system with polyurethane seat and H-point prediction. International Journal of Industrial Ergonomics, **38**, 368–383 (2008).
DOI: 10.1016/j.ergon.2007.08.014

[6] Korodi T., Marcu N.: Polyurethane microcellular elastomers: 1. Effect of chemical composition on tensile strength and elongation at break of poly(ethylene-butylene adipate) based systems. Polymer, **24**, 1321–1326 (1983).
DOI: 10.1016/0032-3861(83)90067-8

[7] Ashton J. H., Mertz J. A. M., Harper J. L., Slepian M. J., Mills J. L., McGrath D. V., Van de Geest J. P.: Polymeric endoaortic paving: Mechanical, thermoforming, and degradation properties of polycaprolactone/polyurethane blends for cardiovascular applications. Acta Biomaterialia, **7**, 287–294 (2011).
DOI: 10.1016/j.actbio.2010.09.004

[8] Arena G., Friedrich K., Acierno D., Padenko E., Russo P., Filippone G., Wagner J.: Solid particle erosion and viscoelastic properties of thermoplastic polyurethanes. Express Polymer Letters, **9**, 166–176 (2015). DOI: 10.3144/expresspolymlett.2015.18

[9] Tian Q., Almásy L., Yan G., Sun G., Zhou X., Liu J., Krakovsky I., Veres M., Rosta L., Chen B.: Small-angle neutron scattering investigation of polyurethane aged in dry and wet air. Express Polymer Letters, **8**, 345–351 (2014). DOI: 10.3144/expresspolymlett.2014.38

[10] Karger-Kocsis J., Kéki S.: Biodegradable polyester-based shape memory polymers: concepts of (supra)molecular architecturing. Express Polymer Letters, **8**, 397–412 (2014). DOI: 10.3144/expresspolymlett.2014.44

[11] Xiao R., Nguyen T. D.: Thermo-mechanics of amorphous shape-memory polymers. Procedia IUTAM, **12**, 154–161 (2015). DOI: 10.1016/j.piutam.2014.12.017

[12] Tobushi H., Okumura K., Hayashi S., Ito N.: Thermomechanical constitutive model of shape memory polymer. Mechanics of Materials, **33**, 545–554 (2001). DOI: 10.1016/S0167-6636(01)00075-8

[13] Hu J., Zhu Y., Huang H., Lu J.: Recent advances in shape–memory polymers: Structure, mechanism, functionality, modeling and applications. Progress in Polymer Science, **37**, 1720–1763 (2012). DOI: 10.1016/j.progpolymsci.2012.06.001

[14] Ratna D., Karger-Kocsis J.: Recent advances in shape memory polymers and composites: A review. Journal of Materials Science, **43**, 254–269 (2008). DOI: 10.1007/s10853-007-2176-7

[15] Meng H., Li G.: A review of stimuli-responsive shape memory polymer composites. Polymer, **54**, 2199–2221 (2013). DOI: 10.1016/j.polymer.2013.02.023

[16] Berg G. J., McBride M. K., Wang C., Bowman C. N.: New directions in the chemistry of shape memory polymers. Polymer, **55**, 5849–5872 (2014). DOI: 10.1016/j.polymer.2014.07.052

[17] Ramoa S. D. A. S., Barra G. M. O., Merlini C., Livi S., Soares B. G., Pegoretti A.: Novel electrically conductive polyurethane/montmorillonite-polypyrrole nanocomposites. Express Polymer Letters, **9**, 945–958 (2015). DOI: 10.3144/expresspolymlett.2015.85

[18] Karger-Kocsis J., Kéki S.: Recent advances in shape memory epoxy resins and composites. in 'Multifunctionality of polymer composites' (eds.: Friedrich K., Breuer U.) William Andrew, Oxford, 822–841 (2015) DOI: 10.1016/B978-0-323-26434-1.00027-1

[19] Hager M. D., Bode S., Weber C., Schubert U. S.: Shape memory polymers: Past, present and future developments. Progress in Polymer Science, **49–50**, 3–33 (2015). DOI: 10.1016/j.progpolymsci.2015.04.002

[20] Hillewaere X. K. D., Du Prez F. E.: Fifteen chemistries for autonomous external self-healing polymers and composites. Progress in Polymer Science, **49–50**, 121–153 (2015). DOI: 10.1016/j.progpolymsci.2015.04.004

[21] Liu Y-L., Hsieh C-Y., Chen Y-W.: Thermally reversible cross-linked polyamides and thermo-responsive gels by means of Diels–Alder reaction. Polymer, **47**, 2581–2586 (2006). DOI: 10.1016/j.polymer.2006.02.057

[22] Araya-Hermosilla R., Broekhuis A. A., Picchioni F.: Reversible polymer networks containing covalent and hydrogen bonding interactions. European Polymer Journal, **50**, 127–134 (2014). DOI: 10.1016/j.eurpolymj.2013.10.014

[23] Laita H., Boufi S., Gandini A.: The application of the Diels-Alder reaction to polymers bearing furan moieties. 1. Reactions with maleimides. European Polymer Journal, **33**, 1203–1211 (1997). DOI: 10.1016/S0014-3057(97)00009-8

[24] Henschel H., Kirsch N., Hedin-Dahlström J., Whitcombe M. J., Wikman S., Nicholls I. A.: Effect of the cross-linker on the general performance and temperature dependent behaviour of a molecularly imprinted polymer catalyst of a Diels–Alder reaction. Journal of Molecular Catalysis B: Enzymatic, **72**, 199–205 (2011). DOI: 10.1016/j.molcatb.2011.06.006

[25] Heo Y., Sodano H. A.: Self-healing polyurethanes with shape recovery. Advanced Functional Materials, **24**, 5261–5268 (2014). DOI: 10.1002/adfm.201400299

[26] Bose R. K., Kötteritzsch J., Garcia S. J., Hager M. D., Schubert U. S., van der Zwaag S.: A rheological and spectroscopic study on the kinetics of self-healing in a single-component Diels–Alder copolymer and its underlying chemical reaction. Journal of Polymer Science Part A: Polymer Chemistry, **52**, 1669–1675 (2014). DOI: 10.1002/pola.27164

[27] Chen X., Dam M. A., Ono K., Mal A., Schen H., Nutt S. R., Sheran K., Wudl F.: A thermally re-mendable cross-linked polymeric material. Science, **295**, 1698–1702 (2002). DOI: 10.1126/science.1065879

[28] Czifrák K., Karger-Kocsis J., Daróczi L., Zsuga M., Kéki S.: Poly(ε-caprolactone) and pluronic diol-containing segmented polyurethanes for shape memory performance. Macromolecular Chemistry and Physics, **215**, 1897–1907 (2014). DOI: 10.1002/macp.201400237

[29] Lendlein A., Schmidt M. A., Langer R.: AB-polymer networks based on oligo(ε-caprolactone) segments showing shape-memory properties. Proceeding of the National Academy of Sciences of the United States of America, **98**, 842–847 (2001). DOI: 10.1073/pnas.031571398

[30] Jiang S., Ji X., An L., Jiang B.: Crystallization behavior of PCL in hybrid confined environment. Polymer, **42**, 3901–3907 (2001).
DOI: 10.1016/S0032-3861(00)00565-6

[31] Crescenzi V., Manzini G., Calzolari G., Borri C.: Thermodynamics of fusion of poly-β-propiolactone and poly-ε-caprolactone. comparative analysis of the melting of aliphatic polylactone and polyester chains. European Polymer Journal, **8**, 449–463 (1972).
DOI: 10.1016/0014-3057(72)90109-7

[32] Ren Z-Y., Wu H-P., Ma J-M., Ma D-Z.: FTIR studies on the model polyurethane hard segments based on a new waterborne chain extender dimethylol butanoic acid (DMBA). Chinese Journal of Polymer Science, **22**, 225–230 (2004).

[33] Adachi K., Achimuthu A. K., Chujo Y.: Synthesis of organic–inorganic polymer hybrids controlled by Diels–Alder reaction. Macromolecules, **37**, 9793–9797 (2004).
DOI: 10.1021/ma0400618

[34] Li F., Hou J., Zhu W., Zhang X., Xu M., Luo X., Ma D., Kim B. K.: Crystallinity and morphology of segmented polyurethanes with different soft-segment length. Journal of Applied Polymer Science, **62**, 631–638 (1996).
DOI: 10.1002/(SICI)1097-4628(19961024)62:4<631::AID-APP6>3.0.CO;2-U

[35] Yakacki C. M., Nguyen T. D., Likos R., Lamell R., Guigou D., Gall K.: Impact of shape-memory programming on mechanically-driven recovery in polymers. Polymer, **52**, 4947–4954 (2011).
DOI: 10.1016/j.polymer.2011.08.027

[36] Rodriguez E. D., Luo X., Mather P. T.: Linear/network poly(ε-caprolactone) blends exhibiting shape memory assisted self-healing (SMASH). Applied Materials and Interfaces, **3**, 152–161 (2011).
DOI: 10.1021/am101012c

[37] Karger-Kocsis J., Mahmood H., Pegoretti A.: Recent advances in fiber/matrix interphase engineering for polymer composites. Progress in Materials Science, **73**, 1–43 (2015).
DOI: 10.1016/j.pmatsci.2015.02.003

eXPRESS Polymer Letters Vol.10, No.4 (2016) 337–348
Available online at www.expresspolymlett.com
DOI: 10.3144/expresspolymlett.2016.31

Self-healing of low-velocity impact and mode-I delamination damage in polymer composites *via* microchannels

M. U. Saeed[1], *B. B. Li*[1], *Z. F. Chen*[1*], *S. Cui*[2]

[1]College of Material Science and Technology, Nanjing University of Aeronautics and Astronautics, 29 Yudao Street, 210016 Nanjing, PR China
[2]College of Materials Science and Engineering, Nanjing University of Technology, 211800 Nanjing, PR China

Received 1 September 2015; accepted in revised form 9 November 2015

Abstract. Microchannels embedded polymer composites were fabricated by resin infusion process using carbon fabric, epoxy resin and hollow glass tubes (HGTs). The effect of a range of low-velocity impact (LVI) and mode-I delamination (M1D) damage on the flexural strength of microchanneled carbon- epoxy composites was studied. A self-healing approach was also employed to recover their lost flexural strength due to these damages. Moreover, influence of LVI, M1D damage and healing on the failure behavior of microchanneled carbon- epoxy composites was also investigated. The results of flexural after impact (FAI) and flexural after delamination (FAD) showed that LVI has more deleterious effect on the flexural strength of carbon- epoxy composites than M1D damage. The loss in flexural strength increased linearly with increase in both impact (by higher impact energies) and delamination damage (by longer delamination lengths). Scanning electron microscopic (SEM) study revealed that self-healing agent (SHA), stored in HGTs placed within carbon- epoxy composites, effectively healed both LVI and M1D damage with excellent healing efficiencies.

Keywords: *smart polymers, self-healing, low-velocity impact, delamination, polymer composites*

1. Introduction

Due to their superior specific strength, stiffness and design flexibility, fiber reinforced polymeric (FRP) composites are widely used in numerous aerospace and engineering applications. However, their poor out-of-plane mechanical properties make them susceptible to various damages like impact, inter-ply delamination and interlaminar shear that result in performance degradation of composite structures [1–3]. Moreover, in most cases, these damages lie beneath the surface or barely visible and a lot of non-destructive (NDT) inspections are necessarily performed to seek their presence and prevent catastrophic failure of structure [4, 5]. Consequently, large factors of safety are incorporated in design to ensure their safety and reliability, which lead to composite structures with higher weight and thicker sections. However, mimic to self-healing capabilities of biological organisms, recent development of self-healing FRP composites that can heal themselves upon damage has proved to be an excellent solution to these problems [6–8].

In FRP composites, self-healing capabilities can be achieved using modified self-healable matrices, SHA-filled microcapsules and SHA-filled microchannels. In modified healable matrix systems [9–11], weak chemical bonds are created within matrix that preferentially breakdown upon damage and reform on heating. Microcapsule-filled healing systems [12–15] contain monomer-filled microcapsules along with solid-phase catalyst throughout the matrix, while microchannel-based healing systems [16–18] comprise SHA-filled vascular channels set-in at different locations in the structure. Upon dam-

*Corresponding author, e-mail: zhaofeng_chen@163.com

age, these chemicals react with each other to repair the damage. Among them, healing through SHA-filled microchannels are getting more and more attentions these days due to additional benefits, such as multifunctional uses for self-sensing [19], enhanced damage visualization [18, 20], active-cooling [21], continuous supply of SHA for higher number of damage-repair cycles [22, 23], autonomous self-healing [24] and accelerated self-healing [25].

In the last decade or so, researchers have employed a variety of manufacturing techniques to vascularize polymeric composites [26] and have studied the effect of different damages on their mechanical properties, their healing via microvascules and restoration of strength under different loading conditions. Among them, Bleay *et al*. [27] placed 5 μm internal diameter, hollow glass fiber (HGFs) plies within a composite laminate and then infused them with SHA for self-healing (in the cured laminate). Compression after LVI testing of their composite panels indicated limited healing due to partial access of resin to the damage area. To improve the healing efficiency, Bond and co-workers utilized 60 μm HGFs and a two part epoxy resin as SHA (separately loaded). However, instead of LVI, they carried out pseudo impacts followed by flexural testing to evaluate the strength restoration after self-repair and found it significant (~97%) [20, 28]. Following same methodology, William *et al*. [29] produced self-healing carbon fiber reinforced composites (CFRC) and conducted flexural test after quasi-static impact and compression test after LVI [30] and in both cases got >90% healing efficiency. Similarly, using millimeter scale HGFs, Zainuddin *et al*. [31] researched the multiple LVI properties of e-glass/epoxy composites and reported good recovery in multiple LVI properties. Moving a step ahead, Norris *et al*. [24] employed an autonomous healing approach (self-sense and self-heal) on CFRC and achieved ~94% recovery in compression after LVI strength. Likewise, Yue *et al*. [32] used SHA-filled capillaries for self-healing, but they also monitored the click chemistry in real time in an elastomer composite by dynamic mechanical analyses. They found their approach quick and versatile in restoring the storage modulus of composite. So far, researchers have either used compression test after drop-weight impact or flexural test after pseudo impact (indentation) to assess the restoration of strength due to self-healing. However, only Kling and Czigány [33] studied the self-healing in HGF reinforced composites through LVI (drop-weight) and three point bend test, but they used HGF fabric. Besides, these studies on healing and restoration of mechanical strength after impact, Kessler and White [34] have studied the healing of delamination damage via restoration of mode-I fracture toughness. However, instead of SHA-filled microchannels, they either directly injected the SHA in the delamination crack or employed SHA-filled microcapsules [35]. Whereas, Patrick *et al*. [36] have studied the restoration of mode-I fracture toughness through healing of delamination damage via vascular network. Therefore, more research is needed to evaluate the effect and healing of LVI (by drop-weight) and delamination damage (by mode-I loading) on CFRC under different loading conditions.

This study investigates the self-healing of LVI (by drop-weight) and delamination damage (by mode-I loading) in microchanneled carbon-epoxy composites by employing four-point-flexural after impact/delamination protocol and SHA-filled microchannels. The effect of healing on the flexural failure of undamaged, LVI-damaged and M1D-damaged microchanneled carbon-epoxy composites is also studied. In this research a novel scheme has also been devised and adopted for the self-activation of self-healing upon mode-1 delamination damage. Microchanneled carbon-epoxy composites samples for M1D were designed and manufactured in such a way that HGTs with variable lengths were carefully placed at specific distances from the Polytetrafluoroethylene (PTFE) film. So, when a mode-I tensile load was applied on the sample, the M1D was generated and during its growth at the specific distance, it hit the circular edge of SHA-filled HGT to release SHA for self-healing.

2. Experimental

2.1. Materials

Carbon fabric (CF3011) used in this study was produced by Weihai Tuozhan Fiber Co. Ltd, China and two-part epoxy resin (Resin-GCC135/Hardener-W93) were purchased from Kunshan Chemicals, China. Whereas, Hollow glass tubes (HGTs) were obtained from Huaxi University, China. Carbon fabric was used as reinforcement and two-part epoxy resin was used as matrix as well as SHA with 100:30; Resin-Hardener ratio. The carbon fibers were PAN based having 3550 MPa tensile strength, 230 GPa tensile modulus, 3000 filaments in one

bundle. Carbon fabric was plain weaved having 200 g·m^{-2} aerial weight. The epoxy resin was Bisphenolic-A based with a viscosity of 700–1100 mPa·s and curing cycle of 24 hours at 25 °C. HGTs with 0.9 mm internal diameter were inserted in carbon-epoxy composites to create microchannels.

2.2. Preparation of microchanneled carbon-epoxy composites

A dry layered-preform was prepared by placing an array of HGTs in the longitudinal direction (with sealed ends) at the mid-plane of carbon fabric layers upon a polished mold surface. Then peel ply, flow media, spiral tubing and resin in-out pipes were positioned accordingly and whole assembly was sealed using Capron film and tacky tape. A vacuum pump was then connected through reservoir to suck-out all the air present inside the bag and among layers. Room temperature cured, low-viscosity epoxy resin was then infused to fill up the vacuum cavities among carbon fabric layers. After curing, microchanneled carbon-epoxy composite laminate was de-molded, peel ply was removed and laminate edges were trimmed to expose the edge faces of HGTs. Schematic diagram of the process is shown in Figure 1.

Two similar composite sheets with HGTs were prepared, one for flexural after LVI (FAI) and other for flexural after M1D (FAD) testing. The second sheet was slightly different from the first. In it, a 15 μm thick PTFE film was used at the mid-plane to generate the starter crack. Additionally, HGTs with lengths 60, 65, 70 and 75 mm were carefully placed at 20, 15, 10 and 5 mm distances from the PTFE film respectively to generate four different sets of samples. Piano hinges were bonded to the samples for load transmission. The thin and long edges of the samples were coated with white corrector fluid and scaled for every 2.5 mm length to visually observe and measure the delamination crack length [37]. Nominal dimensions of M1D samples were; length l = 150 mm, width b = 25 mm and starter crack length a_0 = 50 mm. While dimensions of FAD, LVI and FAI samples were length l = 80 mm, width b = 25 mm as shown in Figure 2. Samples for LVI, M1D and FAD were cut from their respective laminate sheets. Separate sample IDs of FAI4, FAI6, FAI9, FAI11 and FAD5, FAD10, FAD15, FAD20 were assigned to each set of samples. Where FAI represented flexural after impact, 4, 6, 9, 11 were the impact energies with 4, 6, 9, 11 J, FAD for flexural after delam-

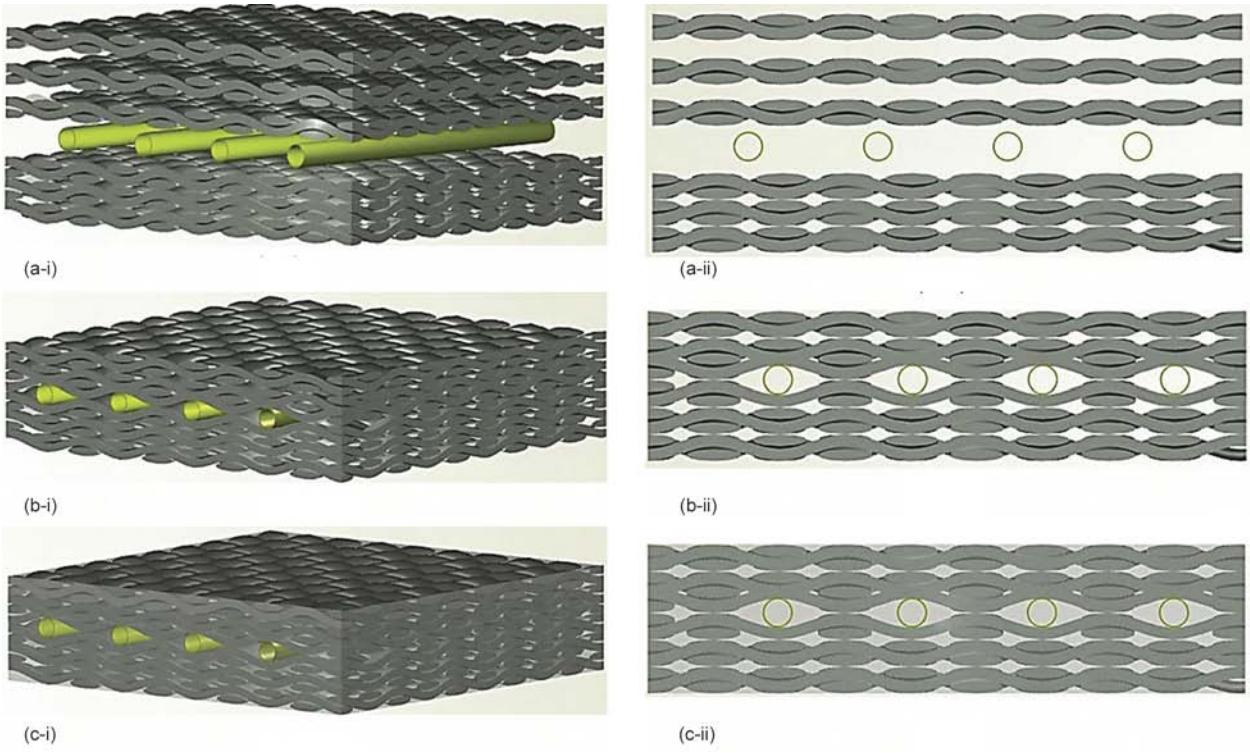

Figure 1. Preparation of microchanneled carbon- epoxy composites; (a-i and a-ii) placement of HGTs between dry fabric layers, (b-i and b-ii) composite processing by resin infusion and (c-i and c-ii) cured microchanneled carbon/epoxy composite

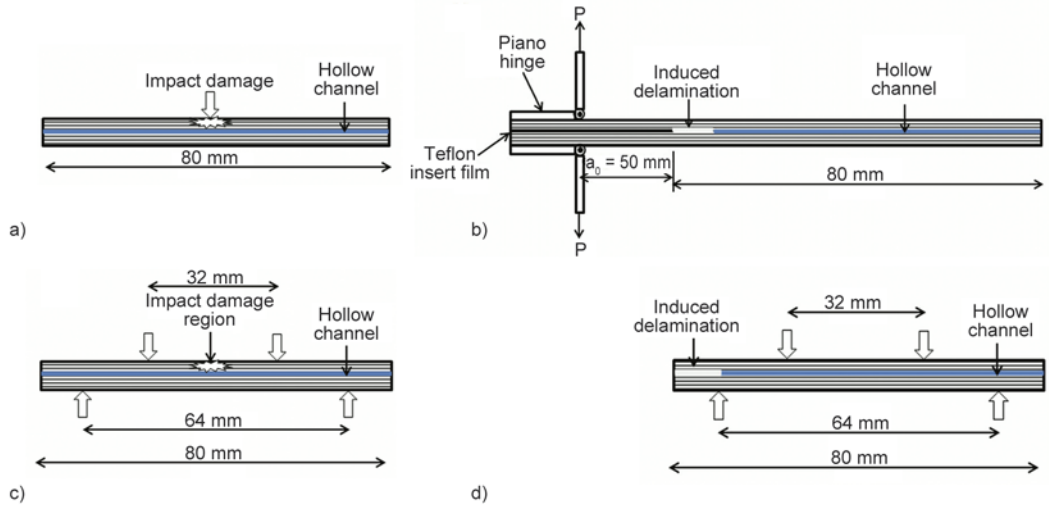

Figure 2. Schematics of samples for (a) LVI, (b) M1D, (c) FAI and (d) FAD

ination and 5, 10, 15, 20 were the delamination lengths in 5, 10, 15, 20 mm

2.3. Characterization

Microchanneled carbon-epoxy samples were infused with SHA with help of vacuum and both ends of microchannels were sealed using commercially available quick-set steel-putty, before they were subjected to LVI drop-weight and mode-I delamination test.

Impact damage was induced by dropping a steel hammer of weight 4.62±0.12 kg with 12±0.1 mm punch diameter from varying heights on the flat surface of each sample with rubber pad supported back face. The weight was dropped from variable heights to get four specific impact energies (4.62, 6.93, 9.24 and 11.55 J) which resulted in impact damage of variable intensities in separate sets of samples. These impact energies were carefully selected so as to induce only slight damage in embedded microchannels (to release SHA) and composite samples and not to cause the complete failure of composite samples.

M1D damage was generated by applying a tensile load to the piano hinges bonded to each sample. Mode-I tests were carried out on a tensile testing machine (CMT-5105, SANS, China) at 1.5 mm·min^{-1} crosshead speed. The growth of M1D front was observed visually and tests were terminated after producing four specific mode-I delaminations (5, 10, 15 and 20 mm) in four different sets of samples. The mode-I delaminations lengths were selected in such a manner that they hit the circular edge of microchannels (to release SHA).

Upon impact and delamination damage, the SHA in the microchannels was released to fill the damage and the samples were allowed to self-heal. The subsequent flexural testing was performed to investigate the efficiency of self-healing for LVI and M1D damage. Four-point bending tests were also carried out on CMT5105 testing machine using test fixtures, as described in ASTM D6272 [38]. The support spans were kept at 32 and 64 mm and crosshead speed was set as 2 mm·min^{-1}. The average value of the flexural strength was calculated by five individual measurements

Surface morphologies of the LVI, M1D damaged, FAI, FAD and healed samples were characterized by scanning electron microscope (SEM, Hitachi SU8010, Japan).

3. Results and discussion

3.1. Impact damage

The damage that appeared on the impact face surface of each sample by LVI with energies 4.62, 6.93, 9.24 and 11.55 J was roughly elliptical and is shown in Figure 3. The minor axis of the impression was aligned with the long axis of the samples due to higher bending stiffness of the laminate in this direction. No significant difference in impact damage was found between three groups of microchanneled carbon-epoxy samples, with (I) microchannels, (II) SHA-filled microchannels and (III) healed samples.

3.2. Delamination damage

The mode-I delamination damage produced was rectangular in shape and located at the mid-plane of the sample with no visible damage onto the front or back

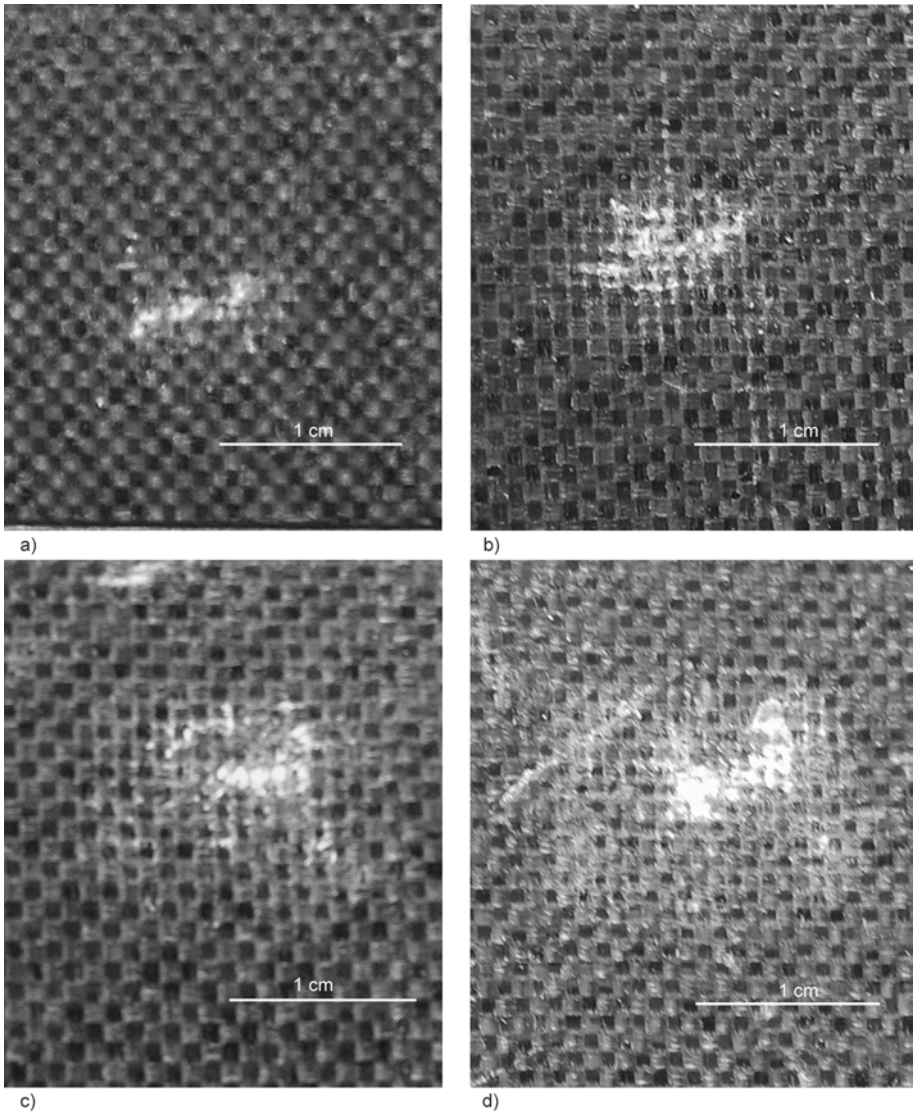

Figure 3. Digital photographs of impact damage at the impact face of microchanneled carbon- epoxy samples due to impact energy (a) 4.62 J, (b) 6.93 J, (c) 9.24 J and (d) 11.55 J

surface of the laminate. The length of the delamination was aligned with the long axis of the sample. No significant damage was observed on the fiber's surface and the delamination was caused only due to failure of matrix. The mode-I delamination damage in assorted samples is presented in Figure 4.

3.3. Four-point-flexural strength

The four-point-flexural strength of undamaged, LVI damaged, M1D damaged and healed microchanneled carbon-epoxy composites were calculated using the following Equation (1) as described in ASTM D6272 [38]:

$$\sigma = \frac{3PL}{4bd^2} \tag{1}$$

where σ is the flexural strength [MPa], P is the load [N], L is the support span [mm], b is the width of sample [mm] and d is the depth of sample [mm]. The healing efficiency [39] was calculated by Equations (2) and (3):

$$\eta_{\mathrm{FAI}} = \frac{\sigma^{\mathrm{Healed}}}{\sigma^{\mathrm{Undamaged}}} \cdot 100 \tag{2}$$

$$\eta_{\mathrm{FAD}} = \frac{\sigma^{\mathrm{Healed}}}{\sigma^{\mathrm{Undamaged}}} \cdot 100 \tag{3}$$

where σ^{Healed} is the flexural strength of the healed sample after impact/delamination damage and $\sigma^{\mathrm{Undamaged}}$ is the flexural strength of undamaged sample. The four-point-flexural strength of undamaged, LVI damaged, M1D damaged and healed microchan-

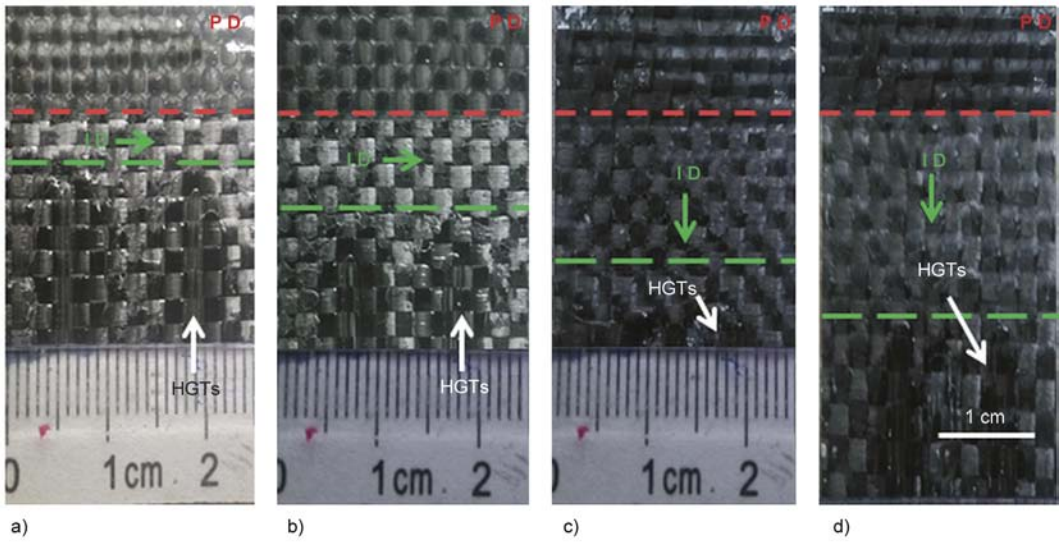

Figure 4. Digital photographs of delamination damage at the mid-plane of microchanneled carbon-epoxy samples with mode-I delamination length (a) 5 mm, (b) 10 mm, (c) 15 mm, (d) 20 mm, where 'PD' is prefabricated delamination and 'ID' is induced delamination

neled carbon-epoxy composites are summarized in Figure 5.

3.4. Effect of LVI damage on flexural strength

The LVI with impact energies in the range of (4.62–11.55 J) reduced the flexural strength of microchanneled carbon- epoxy composites. It is clear from Figure 5 that the loss in flexural strength due to LVI increased steadily with impact energies. The amount of energy absorbed due to 11.55 J (impact energy) was approximately 3 times higher than the energy absorbed due to 4.62 J, so was its effect. The flexural strength decreased 16.77% due to 4.62 J and 28.69% due to 11.55 J, which was almost twice than due to 4.62 J. This decrease in flexural strength due to LVI was directly related to the breakage of carbon fibers in the damage region and widely spread matrix cracks and delaminations, shown in the SEM micrograph in Figure 6, obtained from the region of LVI of microchanneled composite sample.

3.5. Effect of LVI damage on flexural failure

When a four-point-bending load was applied to a LVI damaged microchanneled carbon-epoxy composite sample, initially it was taken-up by top ply carbon fibers, but subsequently it was shifted to the remaining plies through fiber/ resin interface. With increasing load the sample started bending, but the ruptured fibers and matrix microcracks (Figure 6) at the LVI damaged zone acted as stress concentration points and caused the sample to fail at much lower loading value. Final failure of the sample occurred

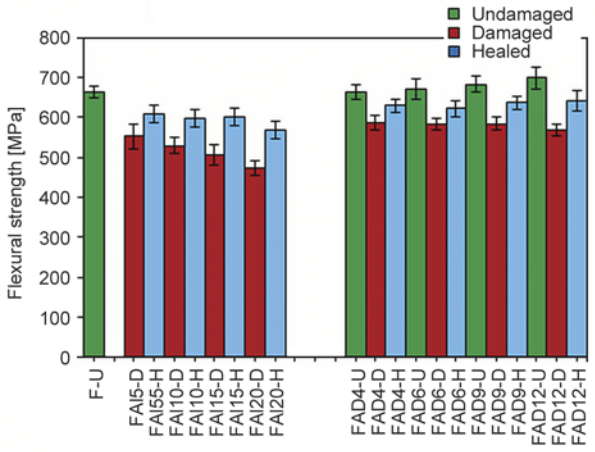

Figure 5. Flexural strength of undamaged, LVI damaged, M1D damaged and healed microchanneled carbon-epoxy composites

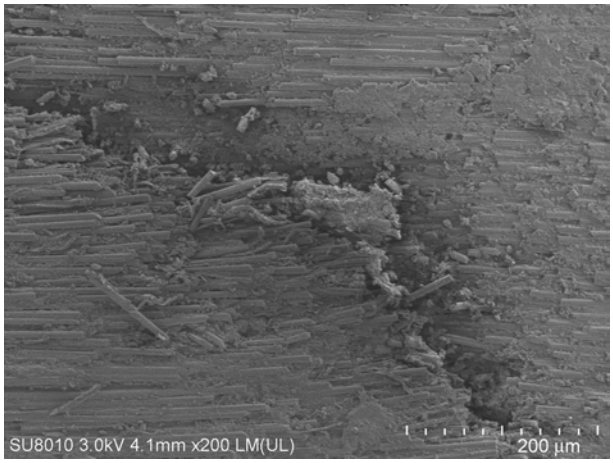

Figure 6. SEM micrograph of LVI damaged microchanneled carbon-epoxy composite sample, showing fiber damage and matrix microcracks in the impact region

Figure 7. Digital photograph of FAI failed microchanneled carbon-epoxy composite sample

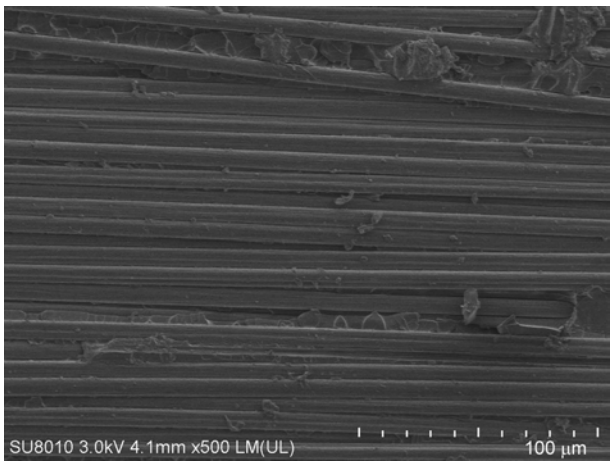

Figure 8. SEM micrographs of Four-point-bend flexural failure of LVI damaged microchanneled carbon-epoxy composite sample before healing, showing interlaminar shear marks; Hackles

with the breakage of top ply carbon fibers under compression and bottom ply carbon fibers under tension (Figure 7).

In addition to breakage of carbon fibers of top and bottom plies a very minute shearing among laminate plies was also found during SEM of the FAI failed microchanneled carbon-epoxy composite samples, as shown in the SEM micrograph in Figure 8.

3.6. Restoration of flexural strength after LVI

The flexural strength of microchanneled carbon-epoxy composites which were not subjected to any external damage (LVI) was 663.85 MPa. However, when these samples were subjected to LVI, the impact energy penetrated into the composite sample and ruptured some fibers at the point of impact along with some microcracks and delaminations in matrix (shown in Figure 6). Furthermore, the LVI also produced fissures in the SHA-filled HGTs and caused the SHA to release, reach the damage zone and fill the microcracks. This release of SHA through cracked HGT is shown in Figure 9a and healing by SHA is shown in Figure 9b.

Figure 9 contains the SEM micrographs of the fracture surfaces, obtained from the region of LVI and four-point-bend flexural failed sample after healing. After 48 hours at room temperature, SHA was fully cured and caused the LVI damage samples to restore their flexural strength (~90%). This healing behavior of LVI-damaged microchanneled carbon-epoxy composite sample is presented in Figure 10.

Figure 11 presents the healing efficiencies of microchanneled carbon-epoxy composite samples dam-

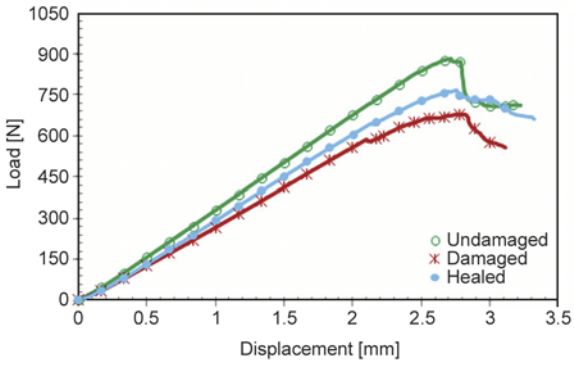

Figure 10. Representative load-displacement curves of undamaged, LVI-damaged (9.24 J) and healed carbon-epoxy composites samples by flexural testing

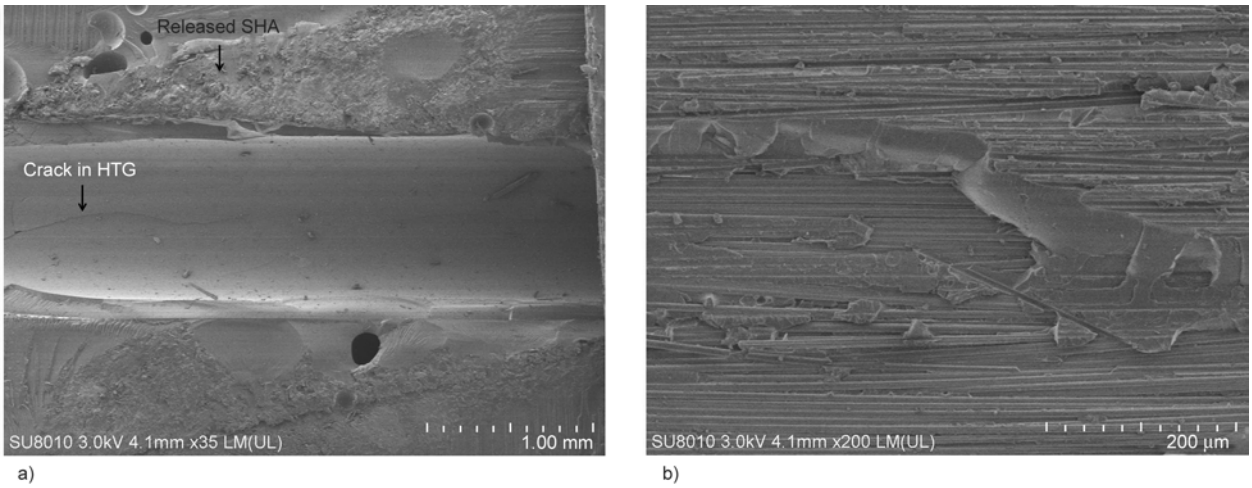

Figure 9. SEM micrographs of LVI-damaged microchanneled carbon-epoxy composite samples after healing (a) showing crack in HGT and release of SHA and (b) showing healing by SHA

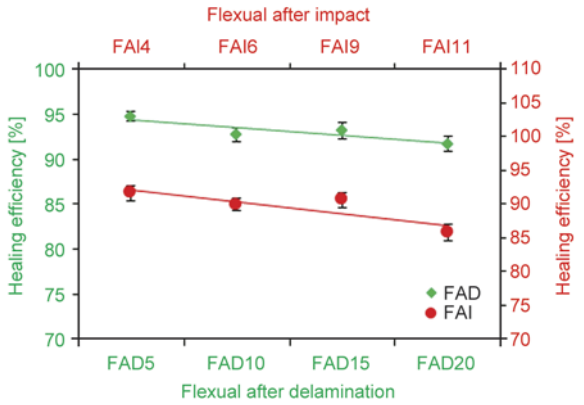

Figure 11. Healing efficiency of carbon-epoxy composites after LVI and M1D damage

aged by a range of LVI. It was observed that the healing and restoration of flexural strength was higher for LVI with smaller impact energies and vice versa. This was because of the reason that the higher impact energies caused greater damage with dense network of microcracks, which could not be completely filled by SHA due to its higher viscosity.

3.7. Effect of healing on the failure of FAI

As the healing mechanism involved the release of liquid SHA to the damage region, which filled the microcracks in the matrix phase and restored the flexural strength upon curing. In case of LVI, carbon fibers were also damaged along with resin and SHA only repaired the microcracks in resin not fibers. Hence, damage in terms of ruptured fibers remained there, also not all the microcracks were fully repaired. So, when LVI-damaged-healed samples were flexural loaded, the LVI damage zone still acted as stress concentration point and caused the healed-samples (Figure 12) to fail in a similar way as that of un-healed samples (Figure 7). Hence, healing did not significantly affect the failure behavior of FAI samples.

3.8. Effect of M1D damage on flexural strength

Effect of a series of M1D damage on the flexural strength of microchanneled carbon-epoxy composites was similar to the effect of LVI damage, but different in magnitude. 5 mm long M1D caused 11%

Figure 12. Digital photograph of healed-FAI failed microchanneled carbon-epoxy composite sample

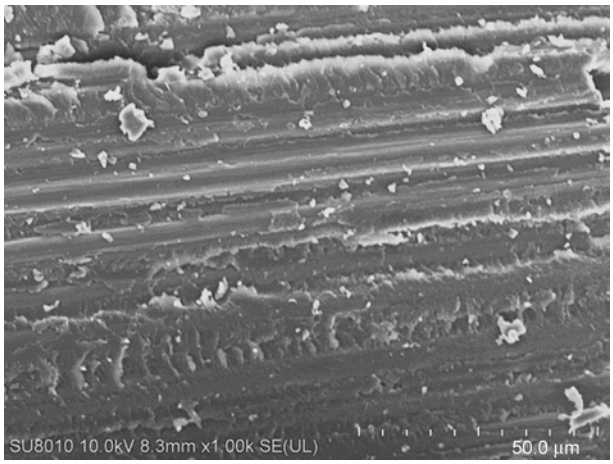

Figure 13. SEM micrographs of M1D damaged microchanneled carbon-epoxy composite sample before healing, showing mode-I delamination failure; River Pattern

decrease in the flexural strength of microchanneled carbon-epoxy composites that increased linearly with increase in M1D length (Figure 5). Figure 5 showed that the highest fall in flexural strength (20%) was due to presence of 20 mm long M1D. This loss was caused mainly due to the separation of layers by M1D. The applied load peeled the sample by ripping the resin not fibers, as the applied load was out of the plane of fiber plies. This breaking of resin in the opening tensile mode, left special marks in resin, known as river pattern, which can be seen in Figure 13.

SEM micrograph of the fracture surface of M1D damage region before healing is presented in Figure 13. Carbon fibers were found intact; their surfaces were smooth with no visible fiber breakage or damage. Hence, the M1D caused failure in matrix phase only. It can also be observed that loss of flexural strength after LVI damage was higher than the loss of flexural strength after M1D. This difference was found due to the type of damage both produced in the host laminate. LVI produced diverse type of damage that affected both fiber and matrix phases in all layers (Figure 6) with highest damage on the top ply (impact face) and lowest on the bottom layer (non-impact face). While M1D damaged only the mid-plane and mainly in the matrix phase without any fiber damage (Figure 13).

3.9. Effect of M1D damage on flexural failure

Similarly, on application of four-point-bending load on a microchanneled carbon-epoxy composite sample with induced M1D damage, it was taken by top

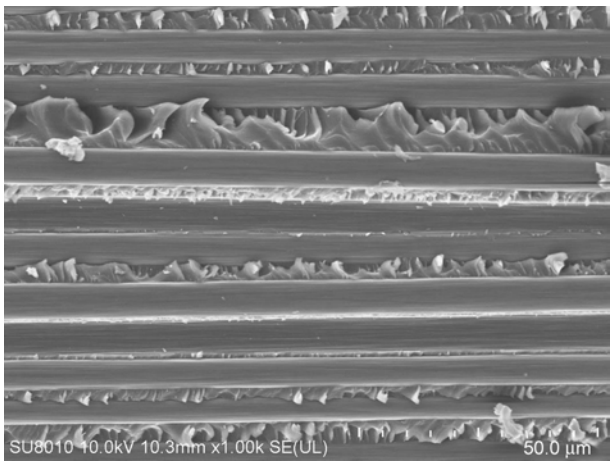

Figure 14. SEM micrograph of four-point-bend flexural failed after M1D damaged microchanneled carbon-epoxy composite sample before healing, showing significant interlaminar shear marks; Hackles

Figure 15. Digital photograph of healed-FAD failed microchanneled carbon-epoxy composite sample

ply first which was successively transferred to the remaining plies through fiber/resin interface. As the load increased, the sample started bending, but at the same time the delamination crack in the sample propagated and caused some slippage among carbon fiber layers. This slippage was the interlaminar shear that appeared as hackles in resin, which can be seen in SEM micrographs of Figure 14.

It was also noted that as the induced M1D damage increased, so was the interlaminar shearing among carbon fiber layers. However, final failure of the sample occurred with the breakage of top ply carbon fibers under compression and bottom ply under tension (Figure 15) i.e. similar to LVI damaged samples but with significant amount of shearing among laminate plies, which depended upon the induced M1D length.

3.10. Restoration of flexural strength after M1D

The flexural strength of undamaged microchanneled carbon-epoxy composites with HGTs of lengths 75, 70, 65 and 60 mm were 665.01, 671.49, 683.33 and 699.16 MPa respectively. In order to induce M1D damage, these samples were mode-I tensile loaded, which separated the layers by damaging the resin not fibers (Figure 13). Likewise, the lengths of M1D

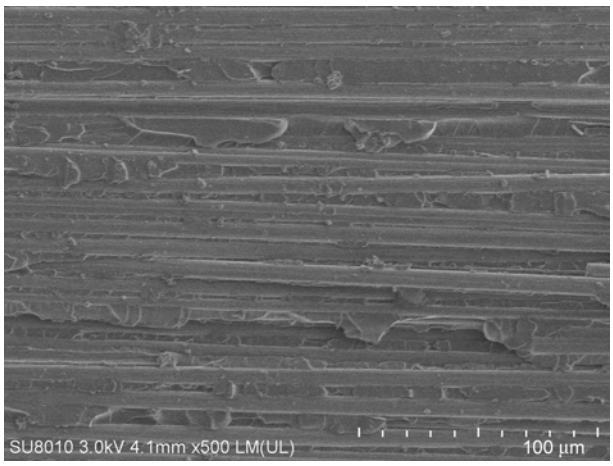

Figure 16. SEM micrographs of M1D damaged microchanneled carbon-epoxy composite sample after healing, showing release and filling of damage by SHA

were such selected that the delamination crack struck the circular edge of SHA-filled HGTs to release the SHA and fill the damage zone. This release of SHA and filling of delamination crack is shown in Figure 16. After release and fill of SHA, each sample was left for curing for 48 hours at room temperature. This curing of SHA re-bonded the detached layers and repaired the M1D damage and restored the flexural strength (~93%).

Similar to LVI damaged samples, healing and restoration of flexural strength after M1D damage was higher for smaller delamination lengths and lower for bigger delamination lengths (as shown in Figure 11). The reason for this analogous behavior was believed to be the same, i.e. viscosity build-up (with time) of resin limited the filling of larger M1D damage. This healing behavior of M1D-damaged microchanneled carbon-epoxy composite sample is presented in Figure 17.

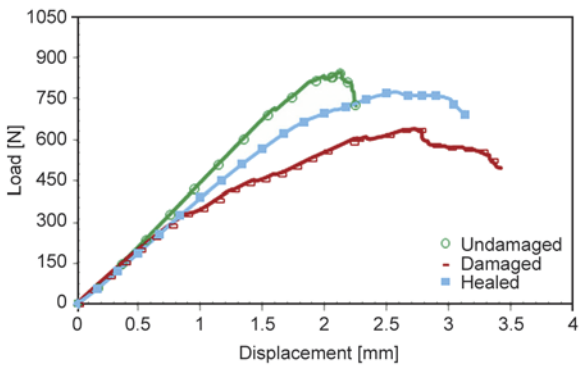

Figure 17. Representative load-displacement curves of undamaged, M1D-damaged (15 mm) and healed carbon-epoxy composites samples by flexural testing

Figure 18. Digital photograph of healed-FAD failed micro-channeled carbon-epoxy composite sample

3.11. Effect of healing on the failure of FAD

In comparison to impact, delamination occurred only in the matrix phase, which was comprehensively repaired by the action of SHA. So, when a flexural load was applied to M1D damaged-healed samples, they failed with the breakage of top and bottom plies carbon fibers (Figure 18) and a very minute shearing among plies due to absence of any starter delamination crack. Hence, healing significantly affected the failure behavior of FAD samples. The main difference was the amount of interlaminar shearing.

4. Conclusions

A biomimetic approach was used to develop and demonstrate a self-repairing capability of carbon-epoxy composites, which proved to be an efficient way to recover flexural strength after a range of LVI and M1D damage events. Damage produced by LVI was diverse that consisted of locally damaged fibers and widespread matrix microcracks, whereas M1D damage was limited to mid-plane and matrix phase only. Due to this reason LVI damage caused more loss in flexural strength and less healing efficiency than the M1D damage. The loss in flexural strength increased linearly with impact energy and delamination length. However, healing efficiency was found to decrease with increase in impact and delamination damage, which was believed to be due to inaccessibility of SHA to some microcracks as a consequence of its viscosity build-up with time. Failure of FAI and FAD samples were significantly different. FAI samples failed due to fiber breakage in the LVI region, while FAD samples failed due to interlaminar shearing in the delamination region and fiber breakage in the center of sample.

Acknowledgements

The authors would like to acknowledge the funding provided by NUAA Fundamental Research Funds (NO.NS2015060) and Jiangsu collaborative innovation center for advanced inorganic functional composites.

References

[1] Richardson M. O. W., Wisheart M. J.: Review of low-velocity impact properties of composite materials. Composites Part A: Applied Science and Manufacturing, **27**, 1123–1131 (1996). DOI: 10.1016/1359-835X(96)00074-7

[2] Saeed M. U., Chen Z., Chen Z., Li B.: Compression behavior of laminated composites subjected to damage induced by low velocity impact and drilling. Composites Part B: Engineering, **56**, 815–820 (2014). DOI: 10.1016/j.compositesb.2013.09.017

[3] Amaro A. M., Reis P. N. B., de Moura M. F. S. F.: Delamination effect on bending behaviour in carbon–epoxy composites. Strain, **47**, 203–208 (2011). DOI: 10.1111/j.1475-1305.2008.00520.x

[4] Ye L., Lu Y., Su Z., Meng G.: Functionalized composite structures for new generation airframes: A review. Composites Science and Technology, **65**, 1436–1446 (2005). DOI: 10.1016/j.compscitech.2004.12.015

[5] Heida J. H., Platenkamp D. J.: In-service inspection guidelines for composite aerospace structures. in '18th World Conference on Nondestructive Testing. Durban, South Africa' p.14 (2012).

[6] Wu D. Y., Meure S., Solomon D.: Self-healing polymeric materials: A review of recent developments. Progress in Polymer Science, **33**, 479–522 (2008). DOI: 10.1016/j.progpolymsci.2008.02.001

[7] Murphy E. B., Wudl F.: The world of smart healable materials. Progress in Polymer Science, **35**, 223–251 (2010). DOI: 10.1016/j.progpolymsci.2009.10.006

[8] Yuan Y. C., Yin T., Rong M. Z., Zhang M. Q.: Self healing in polymers and polymer composites. Concepts, realization and outlook: A review. Express Polymer Letters, **2**, 238–250 (2008). DOI: 10.3144/expresspolymlett.2008.29

[9] Murphy E. B., Bolanos E., Schaffner-Hamann C., Wudl F., Nutt S. R., Auad M. L.: Synthesis and characterization of a single-component thermally remendable polymer network: Staudinger and stille revisited. Macromolecules, **41**, 5203–5209 (2008). DOI: 10.1021/ma800432g

[10] Pingkarawat K., Mouritz A. P.: Stitched mendable composites: Balancing healing performance against mechanical performance. Composite Structures, **123**, 54–64 (2015). DOI: 10.1016/j.compstruct.2014.12.034

[11] Wang C. H., Sidhu K., Yang T., Zhang J., Shanks R.: Interlayer self-healing and toughening of carbon fibre/epoxy composites using copolymer films. Composites Part A: Applied Science and Manufacturing, **43**, 512–518 (2012). DOI: 10.1016/j.compositesa.2011.11.020

[12] Brown E. N., White S. R., Sottos N. R.: Microcapsule induced toughening in a self-healing polymer composite. Journal of Materials Science, **39**, 1703–1710 (2004). DOI: 10.1023/B:JMSC.0000016173.73733.dc

[13] Yin T., Rong M. Z., Wu J., Chen H., Zhang M. Q.: Healing of impact damage in woven glass fabric reinforced epoxy composites. Composites Part A: Applied Science and Manufacturing, **39**, 1479–1487 (2008). DOI: 10.1016/j.compositesa.2008.05.010

[14] Patel A. J., Sottos N. R., Wetzel E. D., White S. R.: Autonomic healing of low-velocity impact damage in fiber-reinforced composites. Composites Part A: Applied Science and Manufacturing, **41**, 360–368 (2010). DOI: 10.1016/j.compositesa.2009.11.002

[15] Yuan Y. C., Ye Y., Rong M. Z., Chen H. B., Wu J., Zhang M. Q., Qin S. X., Yang G. C.: Self-healing of low-velocity impact damage in glass fabric/epoxy composites using an epoxy–mercaptan healing agent. Smart Materials and Structures, **20**, 015024/1–015024/12 (2011). DOI: 10.1088/0964-1726/20/1/015024

[16] Hamilton A. R., Sottos N. R., White S. R.: Pressurized vascular systems for self-healing materials. Journal of the Royal Society Interface, **9**, 1020–1028 (2012). DOI: 10.1098/rsif.2011.0508

[17] Bond I. P., Trask R. S., Williams R.: Self-healing fiber-reinforced polymer composites. MRS Bulletin, **33**, 770–774 (2008).

[18] Pang J. W. C., Bond I. P.: A hollow fibre reinforced polymer composite encompassing self-healing and enhanced damage visibility. Composites Science and Technology, **65**, 1791–1799 (2005). DOI: 10.1016/j.compscitech.2005.03.008

[19] Roach D.: Real time crack detection using mountable comparative vacuum monitoring sensors. Smart Structures and Systems, **5**, 317–328 (2009). DOI: 10.12989/sss.2009.5.4.317

[20] Pang J. W. C., Bond I. P.: 'Bleeding composites' – damage detection and self-repair using a biomimetic approach. Composites Part A: Applied Science and Manufacturing, **36**, 183–188 (2005). DOI: 10.1016/j.compositesa.2004.06.016

[21] Soghrati S., Thakre P. R., White S. R., Sottos N. R., Geubelle P. H.: Computational modeling and design of actively-cooled microvascular materials. International Journal of Heat and Mass Transfer, **55**, 5309–5321 (2012). DOI: 10.1016/j.ijheatmasstransfer.2012.05.041

[22] Toohey K. S., Hansen C. J., Lewis J. A., White S. R., Sottos N. R.: Delivery of two-part self-healing chemistry via microvascular networks. Advanced Functional Materials, **19**, 1399–1405 (2009). DOI: 10.1002/adfm.200801824

[23] Hansen C. J., Wu W., Toohey K. S., White S. R., Sottos N. R., Lewis J. A.: Self-healing materials with interpenetrating microvascular networks. Advanced Materials, **21**, 4143–4147 (2009). DOI: 10.1002/adma.200900588

[24] Norris C. J., White J. A. P., McCombe G., Chatterjee P., Bond I. P., Trask R. S.: Autonomous stimulus triggered self-healing in smart structural composites. Smart Materials and Structures, **21**, 1–10 (2012). DOI: 10.1088/0964-1726/21/9/094027

[25] Hansen C. J., White S. R., Sottos N. R., Lewis J. A.: Accelerated self-healing via ternary interpenetrating microvascular networks. Advanced Functional Materials, **21**, 4320–4326 (2011). DOI: 10.1002/adfm.201101553

[26] Saeed M-U., Chen Z., Li B.: Manufacturing strategies for microvascular polymeric composites: A review. Composites Part A: Applied Science and Manufacturing, **78**, 327–340 (2015). DOI: 10.1016/j.compositesa.2015.08.028

[27] Bleay S. M., Loader C. B., Hawyes V. J., Humberstone L., Curtis P. T.: A smart repair system for polymer matrix composites. Composites Part A: Applied Science and Manufacturing, **32**, 1767–1776 (2001). DOI: 10.1016/S1359-835X(01)00020-3

[28] Trask R. S., Williams G. J., Bond I. P.: Bioinspired self-healing of advanced composite structures using hollow glass fibres. Journal of the Royal Society Interface, **4**, 363–371 (2007). DOI: 10.1098/rsif.2006.0194

[29] Williams G., Trask R., Bond I.: A self-healing carbon fibre reinforced polymer for aerospace applications. Composites Part A: Applied Science and Manufacturing, **38**, 1525–1532 (2007). DOI: 10.1016/j.compositesa.2007.01.013

[30] Williams G. J., Bond I. P., Trask R. S.: Compression after impact assessment of self-healing CFRP. Composites Part A: Applied Science and Manufacturing, **40**, 1399–1406 (2009). DOI: 10.1016/j.compositesa.2008.05.021

[31] Zainuddin S., Arefin T., Fahim A., Hosur M. V., Tyson J. D., Kumar A., Trovillion J., Jeelani S.: Recovery and improvement in low-velocity impact properties of e-glass/epoxy composites through novel self-healing technique. Composite Structures, **108**, 277–286 (2014). DOI: 10.1016/j.compstruct.2013.09.023

[32] Yue H-B., Fernández-Blázquez J. P., Beneito D. F., Vilatela J. J.: Real time monitoring of click chemistry self-healing in polymer composites. Journal of Materials Chemistry A, **2**, 3881–3887 (2014). DOI: 10.1039/C3TA14961G

[33] Kling S., Czigány T.: Damage detection and self-repair in hollow glass fiber fabric-reinforced epoxy composites via fiber filling. Composites Science and Technology, **99**, 82–88 (2014). DOI: 10.1016/j.compscitech.2014.05.020

[34] Kessler M. R., White S. R.: Self-activated healing of delamination damage in woven composites. Composites Part A: Applied Science and Manufacturing, **32**, 683–699 (2001). DOI: 10.1016/S1359-835X(00)00149-4

[35] Kessler M. R., Sottos N. R., White S. R.: Self-healing structural composite materials. Composites Part A: Applied Science and Manufacturing, **34**, 743–753 (2003).
DOI: 10.1016/S1359-835X(03)00138-6

[36] Patrick J. F., Hart K. R., Krull B. P., Diesendruck C. E., Moore J. S., White S. R., Sottos N. R.: Continuous self-healing life cycle in vascularized structural composites. Advanced Materials, **26**, 4302–4308 (2014).
DOI: 10.1002/adma.201400248

[37] ASTM Standard D5528-01: Standard test method for mode I interlaminar fracture toughness of unidirectional fiber-reinforced polymer matrix composites (2007).

[38] ASTM Standard D 6272-02, Standard test method for flexural properties of unreinforced and reinforced plastics and electrical insulating materials by four-point bending (2002).

[39] Brown E. N.: Use of the tapered double-cantilever beam geometry for fracture toughness measurements and its application to the quantification of self-healing. Journal of Strain Analysis for Engineering Design, **46**, 167–186 (2011).
DOI: 10.1177/0309324710396018

eXPRESS Polymer Letters Vol.10, No.4 (2016) 349–359
Available online at www.expresspolymlett.com
DOI: 10.3144/expresspolymlett.2016.32

Shape memory nanocomposite of poly(*L*-lactic acid)/graphene nanoplatelets triggered by infrared light and thermal heating

S. Lashgari[1,2], *M. Karrabi*[1*], *I. Ghasemi*[1], *H. Azizi*[1] , *M. Messori*[2], *K. Paderni*[2]

[1]Iran Polymer and Petrochemical Institute (IPPI), 14965/115, Tehran, Iran
[2]Department of Engineering 'Enzo Ferrari', University of Modena and Reggio Emilia, 41125 Modena, Italy

Received 3 September 2015; accepted in revised form 16 November 2015

Abstract. In this study, the effect of graphene nanoplatelets (GNPs) on the shape memory properties of poly(*L*-lactic acid) (PLLA) was studied. In addition to thermal activation, the possibility of infrared actuating of thermo-responsive shape memory PLLA/GNPs nanocomposite was investigated. The incorporated GNPs were expected to absorb infrared wave's energy and activate shape memory PLLA/GNPs. Different techniques such as differential scanning calorimetry (DSC), wide-angle X-ray diffraction (WAXD), field emission gun scanning electron microscope (FEG-SEM) and dynamic mechanical thermal analysis (DMTA) were used to characterize samples. DSC and WAXD results indicated that GNPs augmented crystallinity due to nucleating effect of graphene particles. GNPs improved both thermal and infrared activating shape memory properties along with faster response. Pure shape memory PLLA was slightly responsive to infrared light and its infrared actuated shape recovery ratio was 86% which increased to more than 95% with loading of GNPs. Drastic improvement in the crystallinity was obtained in nanocomposites with lower GNPs contents (0.5 and 1 wt%) due to finer dispersion of graphene which resulted in more prominent mechanical and shape memory properties enhancement. Infrared activated shape memory PLLA/GNPs nanocomposites can be developed for wireless remote shape control of smart medical and bio-systems.

Keywords: *smart polymers, infrared triggering, nanocomposites, poly(L-lactic acid), graphene*

1. Introduction

Shape memory polymers (SMPs) are a class of smart materials which can recover their primary shape after being deformed to temporary shape [1]. Nowadays these polymers have attracted tremendous attention owing to wide potential applications being expected for these materials in different industries. Smart textiles [2, 3], intelligent medical devices [4, 5] and heat shrinkable films [6] are only some current usages of these polymers. Many scientific studies on this materials are being done and several articles and reviews have been published on this area [1, 7–11]. The stimuli used for activation of SMPs are basically classified into three types; heat (thermo-responsive), light (photo-responsive) and chemical (chemo-responsive) [12]. Thermo- and chemo-responsive shape memory effects (SME) are intrinsic feature of most polymers and are not special characteristic of some special polymers [12]. Thermo-responsive SME is the most popular case and includes both heating and cooling [13]. Heating can be applied directly or non-directly. Stimuli such as electrical resistive heating [14], magnetic field [15], infrared and UV heating light [16, 17] are examples of non-direct heating. Although there are various actuation methods for activating SMPs, but most of shape memory polymers are only able to be actuated through direct heating [18] and triggering with other stimulus is more complex. Nevertheless, many new actuation methods enable remote controlling of SMPs which expand their application in the areas that were impossible for traditionally thermally

*Corresponding author, e-mail: m.karabi@ippi.ac.ir

responsive SMPs. Therefore, SMPs being responsive to other types of stimuli have been gaining increasing interest over the recent years. SMPs based on biopolymers are in spotlight more than the other polymers due to their potential usage in pharmaceutical and medical devices such as surgical sutures, vascular stents, shaping tissue and controlled drug delivery systems [19–23]. Among them poly(lactic acid) (PLA) is one of the most promising biopolymers derived from 100% renewable resources such as corn, tapioca roots and sugarcane which can be readily degraded to lactic acid through hydrolysis [24]. Therefore, it has more extensive application in the medical industry compared to other bio-polymers [25]. Due to its bio properties and intrinsic shape memory abilities, this polymer has attracted interests of researchers and industries in this field and its shape memory properties have been studied by some researchers until now [23, 24, 26–32] However, most of mentioned studies have focused on thermal actuation and researches on multi-stimuli poly(lactic acid) shape memory are still lacking. Paakinahoet and coworkers [18, 33] reported water induced poly(*D*,*L*-lactide) shape memory polymer which is able to recover its shape at the aqueous environment at body temperature. Zhang *et al*. [22], and Zheng *et al*. [34] produced PLLA-Fe_3O_4 shape memory composite with thermal and magnetic field responsiveness.

Actuation by stimuli other than heat needs special functionalities in the polymer which are acquired through different ways. One of the facile and effective routes is the incorporation of special fillers into polymeric systems. Among the fillers, graphene is one of the most important carbonaceous fillers which has a range of extraordinary mechanical, thermal and electrical properties [35, 36] attracted a lot of attention in the polymeric systems. Introduction of graphene into polymers confers novel properties to shape memory composites including quicker response to thermal activation and the capability of responding to other stimuli such as infrared (IR) light, electricity, magnetic and others. These unique properties of graphene have been used to produce different multi-stimuli responsive SMPs. Infrared light actuated SMPs are a class of these materials and some studies have been done in this regard [17, 37, 38]. Kashif *et al*. [37] have produced shape memory polyolefin elastomer/modified graphene nanocomposites responding to infrared light with healing properties. Feng *et al*. [38] have prepared IR actuated shape memory polyurethane with the aid of reduced graphene oxide and carbon nanotube hybrids. Park and Kim [17] have studied on the semi-crystalline polyurethane/graphene shape memory nanocomposite system responding to infrared light. Tang *et al*. [39] have added graphene to polyester/carbon nanofibers composite to improve its capability in responding to various stimuli. However, literature reporting on the graphene based biodegradable SMPs respondent to infrared light is still limited.

Herein, we reported one type of graphene-containing shape memory PLLA which is capable of responding to direct thermal heating and infrared light. The effect of graphene on crystallinity and its correlation with shape memory and thermomechanical properties are studied. To the best of our knowledge, although some studies have been done on the PLLA/graphene system [40–44] until now, but this system is not already reported and described in the literature in terms of shape memory behavior. On the other hand, the infrared triggering of shape memory PLLA has not been investigated so far and our experimental evidence regarding infrared sensitivity of PLLA/graphene composites can be helpful for designing remote controlling shape memory devices.

2. Experimental

2.1. Materials

Poly(*L*-lactic acid) PLLA 3251D (1.4 mol% *D*-lactic acid, 98.6 mol% *L*-lactic acid content, average molecular weight of 90~120 kg/mol) was obtained from Natureworks (USA). Graphene nanoplatelets GNPs (grade C-750, the average thickness of 1–5 nm, length of less than 2 μm and superficial area 750 m^2/g) were purchased from XG Sciences (Lansing, USA). Chloroform was supplied by Sigma-Aldrich.

2.2. Sample preparation

At first, PLLA and GNPs were dried in a vacuum oven at 80 °C for 12 h to remove moisture completely. PLLA/GNPs nanocomposite samples were prepared by solution casting at 0.5, 1, 2, 4 and 6 wt% loading of GNPs. Desired amounts of the dried GNPs were added to chloroform (75 mL) and stirred at room temperature for 1 day with a magnetic stirrer, then 75 mL of PLLA solution (200 mg/mL) was added to the suspension, after that, it was put in the ultrasonic bath (Elma T460) for 15 minutes, at last, final products were poured into Petri dish and left for

1 day at room temperature to allow chloroform evaporation following by drying in vacuum oven at 60 °C for 24 h for complete evaporation of solvent. After drying, the films were pressed in an electrically-heated hydraulic press at 210 °C under 1000 kPa pressure for 3 min after 5 min preheating and then quickly cooled to room temperature by circulating cold water. The samples were denoted according to GNPs [wt%] loadings as PLLA-GNP0.5, PLLA-GNP1, PLLA-GNP2, PLLA-GNP4 and PLLA-GNP6 with 0.5, 1, 2, 4 and 6 wt% of GNPs, respectively.

2.3. Characterization

2.3.1. Morphology

Fractured surfaces of the PLLA/GNPs nanocomposites were observed using a high-resolution field emission gun SEM microscope (FEG-SEM, Nova NanoSEM 450, FEI of USA). The samples were fractured in liquid nitrogen prior to FEG-SEM imaging.

2.3.2. DSC and WAXD

To study thermal properties of specimens and effect of graphene on these properties, differential scanning calorimetry (DSC) (TA Instruments DSC 2010, New Castle, DE, USA) analysis was carried out at nitrogen atmosphere. Thermal history of specimens was erased through a first heating scan from 0 to 250 °C at a heating rate of 10 °C/min, then cooled to the room temperature at a cooling rate of 10 °C/min, followed by a third scan at the same heating rate to 250 °C. The mid-point of the start and end of the transition in DSC curves was taken as the T_g^{DSC} value. The glass transition temperature (T_g^{DSC}), cold crystallization temperature (T_{cc}), cold crystallization enthalpy (ΔH_{cc}), melting temperature (T_m) and melting enthalpy (ΔH_m) were determined from the second heating curve. The degree of crystallization (χ_c) was obtained using the following Equation (1):

$$\chi_c[\,\%\,] = \frac{\Delta H_m - \Delta H_{cc}}{\Delta H_m^0(1-\varphi_f)} \cdot 100 \tag{1}$$

where ΔH and ΔH_{cc} are the melting enthalpy and the cold crystallization enthalpy of test sample respectively, ΔH_m^0 is the melting enthalpy of the 100% crystalline PLLA (93.0 J/g [45]) and φ_f is the weight percentage of filler.

For a better analysis of crystallinity, wide angle X-ray diffraction (WAXD) test was done on samples using Panalytical X' Pert Pro instrument. Test scanning rate was 5°/min at 40 kV and 100 mA with Cu-Kα1 irradiation (λ = 1.54 Å) in the range of 10~60°.

2.3.3. Shape memory performance

Shape memory performances of samples were investigated by two actuation methods, direct heating, and infrared light. Programming of temporary shape in direct heating actuation was carried out through a four-stage thermo-mechanical cycle by means of a dynamic mechanical thermal analysis instrument (DMA Q800, TA Instruments, New Castle, DE, USA). Rectangular strips of samples were programmed under fixed-strain condition according to later steps: (1) deforming the specimen at T_H = 75 °C under a loading ramp at 10 MPa·min^{-1} up to 100% strain, (2) cooling the specimen to T_L = 0 °C instantly by keeping the attained strain constant, (3) maintaining the sample at T_L for 30 min after removal the load, and (4) raising the temperature from T_L to T_H then maintaining at the latter for 30 min. Under these conditions, shape fixity rate (R_f) and shape recovery rate (R_r) are defined according to following Equations (2) and (3) [46]:

$$R_f(N) = \frac{\varepsilon_u(N)}{\varepsilon_m} \cdot 100\,\% \tag{2}$$

$$R_r(N) = \frac{\varepsilon_m - \varepsilon_p(N)}{\varepsilon_m - \varepsilon_p(N-1)} \cdot 100\,\% \tag{3}$$

where $\varepsilon_u(N)$ is the tensile strain after unloading at T_L in the N^{th} cycle (N), ε_m is maximum strain. $\varepsilon_p(N)$ and $\varepsilon_p(N-1)$ are the unrecovered strains after heating the sample to T_H in the N^{th} cycle and previous one, respectively.

Bending test [47, 48] was utilized to study the feasibility of IR actuation of SMP composites. Rectangular strips of PLLA/GNPs nanocomposites (60 mm× 5 mm×1 mm) were deformed into U-like shape at 75 °C followed by rapid cooling with liquid nitrogen to fix deformation. An infrared (IR) lamp (Philips, 150 W) was used as the IR activation light source. The distance between lamp and specimen was 25 cm. The power density to samples was around 20 mW/cm^2 measured by a light density meter. The recovery ratio (R_r) was calculated according to Equation (4), in which θ is the returned angle of the strip from temporary U-like shape to the original one. In all cases, more than three samples were tested, from which the mean and standard deviation were calcu-

lated. An infrared video camera (InfRec Thermo GEAR, G120) was used in our study to monitor the temperature distribution and shape recovery behavior simultaneously (Equations (4)):

$$R_r = \frac{\theta}{180^\circ} \cdot 100\% \quad (0^\circ < \theta < 180^\circ) \tag{4}$$

2.3.4. Dynamic mechanical thermal analysis (DMTA)

Thermomechanical properties of the samples were measured by means of DMA Q800 (TA Instruments, New Castle, DE, USA) using rectangular strips (overall length: 25 mm; length between grips: 8 mm; width: about 5 mm, thickness: 1 mm) operating in the tensile mode at an oscillation frequency of 1 Hz with a static force of 10 mN and a oscillation strain of 0.05%. The samples were measured over a temperature range from room temperature to 160 °C at a heating rate of 5 °C/min.

3. Results and discussion

3.1. Microstructure

Figure 1 shows the FEG-SEM micrographs of fractured surface of PLLA/graphene with 1 and 4 wt% of GNPs at the magnification of 12 000×. As can be seen, graphene nanoplatelets exhibited fine dispersion and uniform distribution in the matrix with a little aggregation in the latter sample (squares in Figure 1b) due to higher filler content. Therefore, it seems that better thermal and mechanical properties can be attained in nanocomposites with lower GNPs content. The homogenous distribution of graphene in the matrix is associated to the relatively good interaction of PLLA and GNPs resulting in uniform infrared absorption in the shape memory test which is investigated further.

3.2. Thermal and crystallinity analysis

Glass transition temperature (T_g) and crystallinity status are two important factors in T_g based semi-crystalline SMPs which are considered as the switching temperature and fixed phase of SMPs, respectively. So it is important to investigate the effect of graphene on the T_g and crystallinity of PLLA prior to shape memory studying. Figure 2 depicts cooling thermograms and 2nd heating thermograms of DSC scans and the detailed data derived from them are summarized in Table 1. As can be seen, T_g values of PLLA/ GNPs composites are slightly increased with addition of GNPs compared to pure PLLA. This may be attributed to chain mobility restriction caused by GNPs particles resulting in higher T_g temperatures. However, owing to small shifting in glass transition temperature, the switching temperature of all samples in shape memory tests can be considered identical. The peaks specified in the cooling thermograms are related to the crystallization temperature (T_c) of specimens. As can be seen, at low graphene loading (0.5 and 1 wt%) nanocomposites, the T_c peak intensified drastically and shifted to higher temperatures compared to pure PLLA. This means that the incorporation of graphene into PLLA at low contents favored the formation of crystalline domains and enhanced crystallinity percentage (%X_c) which are presented in Table 1. Undoubtedly, this significant rise of crystallinity is associated to the nucleating effect of graphene which enhances the crystallization kinetic of PLLA and leads to the formation of more crys-

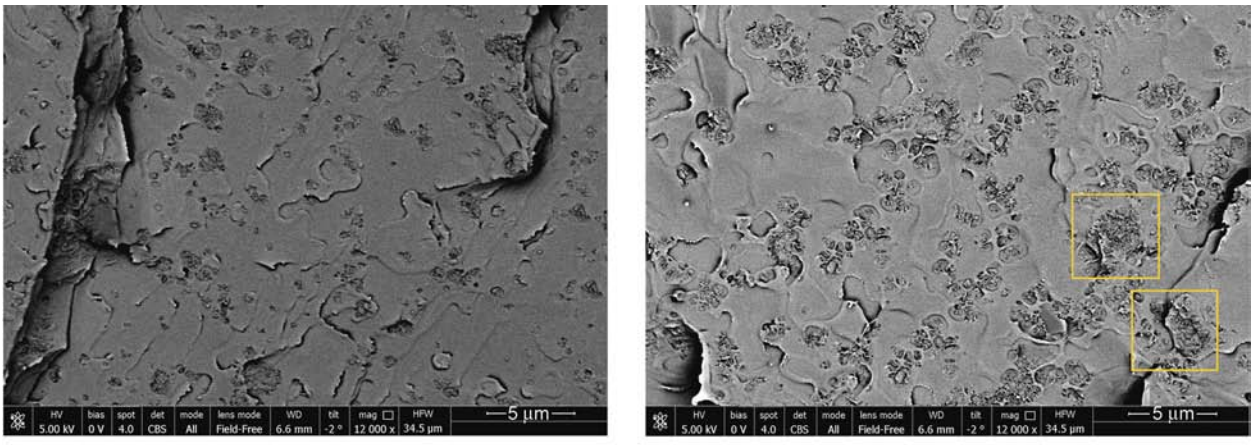

Figure 1. FEG-SEM images of (a) PLLA-GNP1 nanocomposite and (b) PLLA-GNP4 nanocomposite

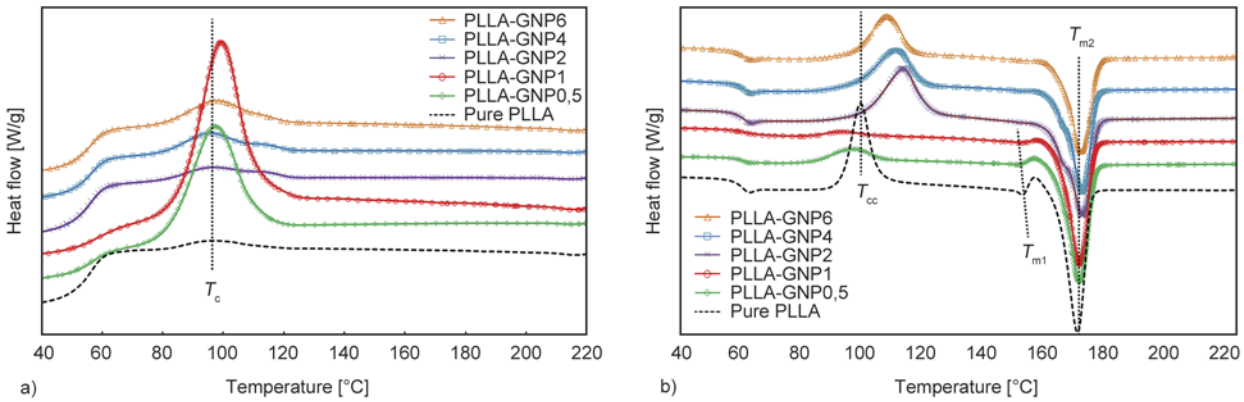

Figure 2. (a) cooling thermograms and (b) 2nd heating thermograms of pure PLLA and its nanocomposites with various loading of GNPs

Table 1. Thermal properties of PLLA and its composites derived from DSC analysis

Sample	DSC Data								
	%GNPs	T_g^{DSC}	T_{cc}	T_{m1}	T_{m2}	T_c	ΔH_{cc}	ΔH_m	$\%X_c$
Pure PLLA	0	59.9	98.4	150.9	168.6	96.0	41.2	49.3	8.7
PLLA-GNP0.5	0.5	61.3	96.2	149.6	169.2	97.2	13.4	47.5	36.8
PLLA-GNP1	1	61.0	92.9	150.1	169.3	99.2	6.9	44.7	41.1
PLLA-GNP2	2	60.1	112.2	162.8	170.3	95.9	32.0	40.5	9.4
PLLA-GNP4	4	60.5	110.0	–	170.1	95.3	32.3	39.3	7.8
PLLA-GNP6	6	60.0	104.5	–	169.2	97.8	32.1	39.8	8.8

tals. However, over 1 wt% graphene loading, T_c peaks shift back to lower temperatures and their intensity are decreased drastically. Meanwhile, their crystallinity percentage ($\%X_c$) are reduced to as low as pure PLLA in these samples. This is because, with the rise of graphene percentage, particles would be tending to aggregate as already illustrated in Figure 1. Therefore, although they act as the nucleating agent, but they would hinder chain mobility and depress the crystallinity at the same time. Following the changes in the crystallinity, addition of GNPs caused in shifting of cold crystallization temperature (T_{cc}) (Figure 2b) to lower temperatures at low graphene loadings (0.5 and 1 wt%) from 98.4 to 92.9 °C and shifting back to higher values as GNPs composition rises to 2 and higher wt% of GNPs . Therefore, few amounts of GNPs are seemed suitable for enhancement of crystallinity through providing nucleation sites.

Double melting point which is ascribed to melt-recrystallization mechanism or crystals with different structures or different degree of perfections [49] is observed in pure PLLA and nanocomposites. The sharp peak of T_{m1} in the pure PLLA may be related to melt re-crystallization of less perfect crystals formed during cold crystallization. However, presence of GNPs caused to decrease of this peak in the PLLA-GNP0.5 and PLLA-GNP1 due to their nucleating effect that leaded to faster crystallinity kinetics with the formation of more perfect crystals directly in the cooling process. As already mentioned, with increase of GNPs to more than 1 wt%, crystallinity percentage showed decreasing trend and melting peaks merged together and T_{m1} appeared as a step in main melting peak of PLLA-GNP2 and disappeared in the PLLA-GNP4 and PLLA-GNP6.

The disappearance of T_{m1} peak in the latter composites may correspond to their higher T_{cc} compared to pure PLLA which would result in the formation of more stable and perfect crystals during cold crystallization process due to enhancement of segment mobility at higher T_{cc} temperatures.

To gain more insight into crystallinity and effect of GNPs, WAXD analysis was carried out. Figure 3 exhibits the WAXD patterns of GNPs, pure PLLA, and its nanocomposites. The peak at $2\theta = 26.5°$ in GNPs is associated to the (002) diffraction peak of pristine graphene nanosheets. The GNPs peak is not observed in the composites containing of 0.5 and 1 wt% of graphene indicating a good exfoliation that was confirmed by FEG-SEM images (Figure 1a for PLLA-GNP1), however this peak appeared slightly (shown by arrow in Figure 3) beyond 2 wt% of GNPs loading (PLLA-GNP4 and PLLA-GNP6) which is related to the agglomerates that are not completely separated (as specified in Figure 1b for PLLA-

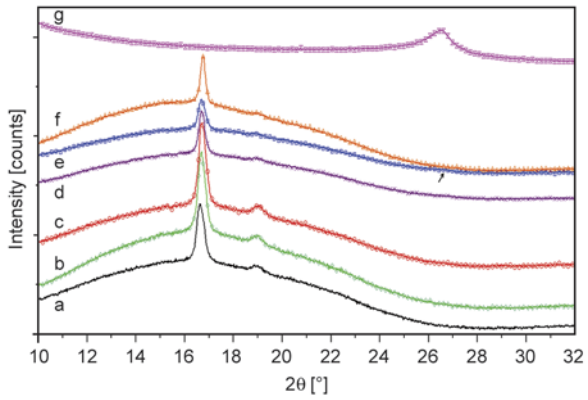

Figure 3. WAXD patterns of (a) pure PLLA, (b) PLLA-GNP0.5, (c) PLLA-GNP1, (d) PLLA-GNP2, (e) PLLA-GNP4, (f) PLLA-GNP6 and (g) GNPs

GNP4). The peaks around $2\theta = 16.7$ and 19° are ascribed to α crystals of PLLA [28]. These peaks are observed in all of nanocomposites suggesting the crystalline structure of PLLA is not changed with the incorporation of GNPs. The intensity of peaks increased enormously at low graphene loading (0.5 and 1 wt%). However, marginal changes are seen over 2 wt% GNPs fraction. These observations are in line with the DSC results and correspond to higher crystallinity percentage at lower GNPs content due to better dispersion and nucleating of graphene particles.

3.3. Thermo-mechanical analysis

Storage modulus (E') and damping factor ($\tan\delta$) diagrams of pure PLLA and its nanocomposites are shown in Figure 4. As expected, storage modulus of nanocomposites is enhanced below T_g compared to that of pure PLLA due to the reinforcing effect of GNPs particles. Moreover, as already has reported [50], in the nano-sized polymer composites, the size of fillers is similar to the size of polymer segments, so the thermomechanical behavior of polymer segments is more affected by the fillers which is considered as the friction interactions resulting to improved mechanical properties. However, the increasing is not in a monotonic trend and starts dropping beyond 4 wt%. This may be corresponding to the aggregates at the higher GNPs fractions (Figure 1b) lowering stiffening effect of graphene and leading to decrease of storage modulus. Meanwhile, as reported by Zhenge *et a*l. [32], higher glassy modulus will result in larger shape fixity in the cooling cycle and larger shape recovery in the heating process which is further corroborated by the shape memory results. The peaks of $\tan\delta$ curves are related to the glass transition temperatures (T_g^{DMTA}) of the samples. The T_g^{DMTA} of pure PLLA is ~80 °C and the addition of GNPs is caused to increase of T_g^{DMTA} due to the restriction effect of GNPs on the chain mobility of PLLA. The T_g obtained through DMTA is higher than the T_g acquired by DSC results. This is related to the difference of T_g definition in two techniques and also the heat transport hysteresis for larger scale samples in DMTA, while the DSC transition being measured is in smaller scale segmental mobility, which occurs at lower temperatures [51, 52]. In addition, the peak height of $\tan\delta$ decreases in the nanocomposites compared to pure PLLA due to decreasing in the energy dissipation as a result of elastic GNPs presence.

3.4. Shape memory properties

3.4.1. Thermal-activation

The typical cyclic shape memory test for pure PLLA and PLLA-GNP1 are plotted in Figure 5 which shows temperature and strain as a function of time.

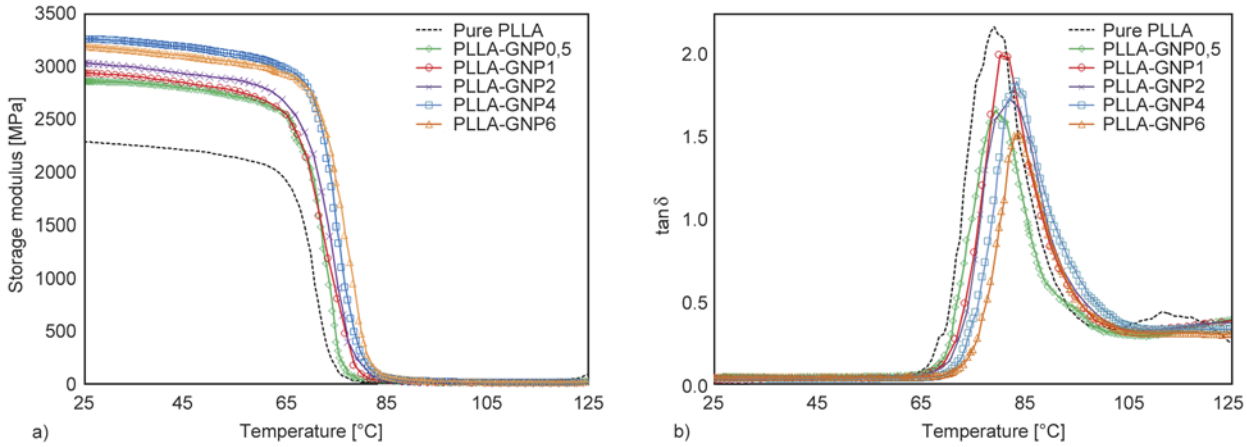

Figure 4. Temperature dependence of (a) storage modulus (E') and (b) loss factor ($\tan\delta$) of pure PLLA and its nanocomposites with GNPs

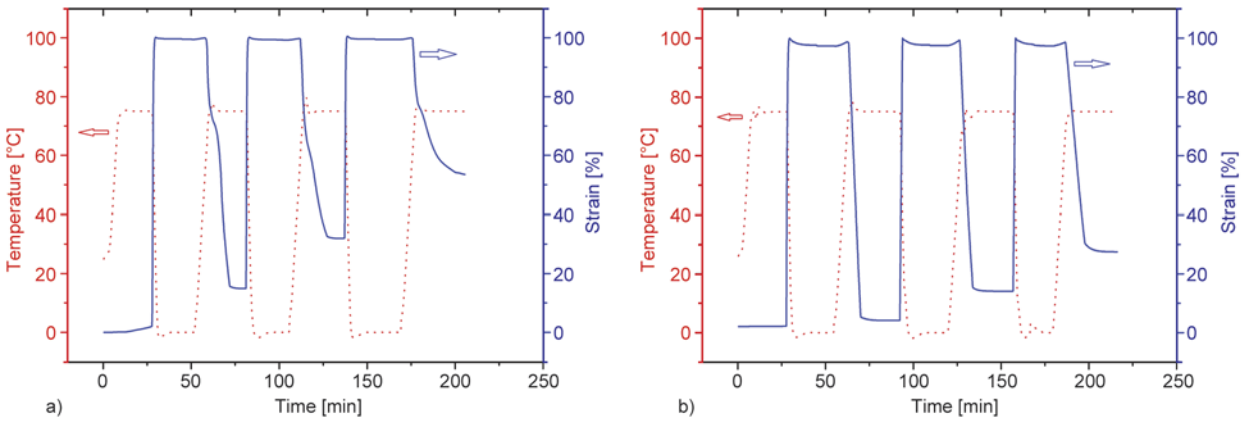

Figure 5. Shape memory cycle of (a) pure PLLA and (b) PLLA-GNP1 utilized with DMA instrument

Detailed shape memory parameters including shape fixity (R_f), shape recovery (R_r) and stress at maximum deformation derived from the plots are presented in Table 2. As can be observed, R_f and R_r of pure PLLA at the first cycle are 98.3 and 85% respectively. The shape memory effect of PLLA is associated to the crystalline and amorphous phase of PLLA acting as fixed and reversible phase respectively [24, 53]. The stress at maximum deformation is higher for nanocomposites compared to pure PLLA due to the enhancing effect of GNPs in the mechanical properties of nanocomposites already mentioned. Figure 6 shows the shape recovery and shape fixity of samples as a function of graphene content. By incorporating of graphene into PLLA, its shape memory properties increases and reaches to optimum at the PLLA-GNP1 then starts reduction at the higher contents of graphene. However, nearly all nanocomposites exhibited higher shape fixity and shape recovery compared to pure PLLA. This may be attributed to the enhancement of crystallinity and thermomechanical properties of nanocomposites resulting in more stable fixing phase leading to better fixation and recovery. Meanwhile, graphene improves heat conductivity which results in more efficient heat transfer during cooling and heating processes leading to faster response with less dissipation of energy and higher values of shape fixity and shape recovery in the nanocomposites.

Table 2. Shape memory properties of pure PLLA and its composites with GNPs actuated by thermal heating at 100% deformation strain

Cycle no.	$\varepsilon_p(N)^*$ [%]	$R_r(N)^{**}$ [%]	$R_f(N)^{***}$ [%]	Stress at max. deformation strain [MPa]
Pure PLLA				
1	14	85±3	98.3	1.0
2	25	80±2	98.2	0.8
3	34	71±1	98.0	0.7
PLLA-GNP0.5				
1	8	91±3	99.2	1.6
2	19	84±2	99.1	1.5
3	30	76±1	98.6	1.3
PLLA-GNP1				
1	2	97±2	99.1	1.7
2	11	89±3	99.0	1.6
3	21	84±2	99.0	1.5
PLLA-GNP2				
1	9	90±3	99.3	1.7
2	20	84±2	99.2	1.4
3	29	78±2	99.1	1.3
PLLA-GNP4				
1	9.1	90±2	99.4	1.7
2	21.1	83±3	99.2	1.3
3	31.0	76±3	99.1	1.2
PLLA-GNP6				
1	11.3	88±2	99.4	1.6
2	23.4	81±2	99.1	1.3
3	32.6	74±3	99.0	1.1

$^*\varepsilon_p(N)$ is the unrecovered strain at the N^{th} cycle after heating the sample to T_H temperature
$^{**}R_r(N)$ is the shape recovery rate at the N_{th} cycle
$^{***}R_f(N)$ is the shape fixity rate at the N^{th} cycle

As it is well known [21] the crystalline part of PLLA polymer has more effect on shape memory properties than the amorphous phase, so decreasing trend of shape memory parameters for composites beyond 1 wt% graphene can be attributed to the occurrence of aggregates (Figure 1b) and crystallinity reduction leading to weakening of fixed phase and lowering shape memory performance. With increasing cycle number in the shape memory test, R_r shows decreasing trend due to irreversible processes such as slippage of crystalline domains, plastic deformation of PLLA chains, breaking down of some physical linkage and other factors which cannot be

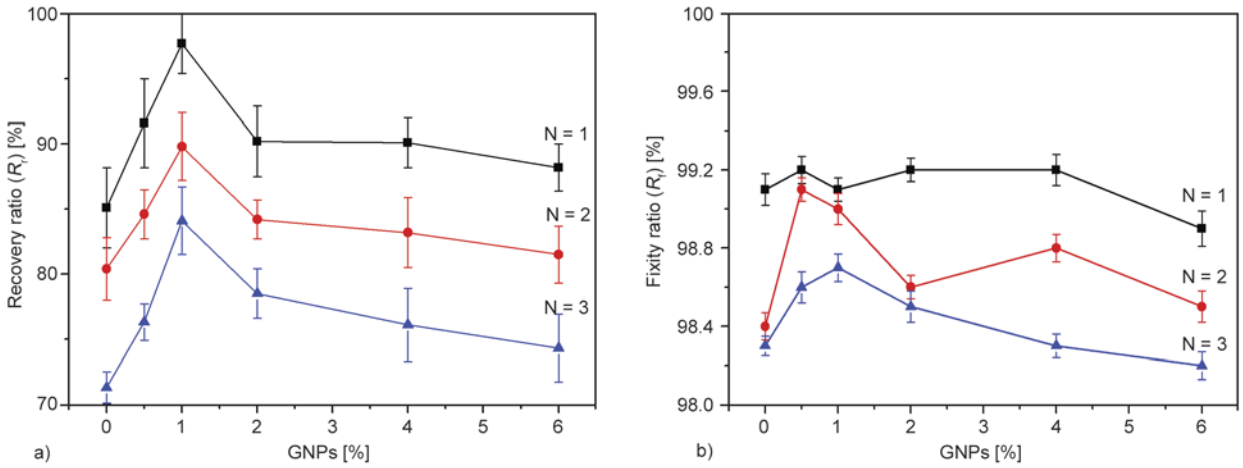

Figure 6. (a) Recovery ratio and (b) fixity ratio relationship versus %GNPs of thermo-activated PLLA nanocomposites; *N* indicates cycle number

recovered during recovery process and result in decreasing R_r. The reduction of R_f may also be correlated to the deformation and displacement of crystalline phase which acts as the fixing part.

3.4.2. Infrared activation

Figure 7 illustrates the thermo-camera images of a free recovery process in the pure PLLA, PLLA-GNP1 and PLLA-GNP6 composites actuated by infrared radiation. The infrared absorption of pure PLLA was low as did not start recovering after 25 s. Graphene enhanced IR absorption of PLLA remarkably which resulted in faster and higher recovery of original shape. The recovering is through transforming infrared light into heat and increasing temperature to switching temperature. As can be seen, at t = 20 s, pure PLLA did not start recovering but PLLA-GNP1 and PLLA-GNP6 recovered around 50 and 90% respectively. The PLLA-GNPs specimens with higher GNPs loadings exhibited faster recovery with lower induction time. This is because more infrared energy is absorbed and transformed into thermal energy within the same radiation time. However, equilibrium recovery which is presented in Table 3 had optimum and reached to maximum (99%) in PLLA-GNP1. This shows that shape recovery of polymers with T_g based switching temperature is accompanied by softening of the glassy

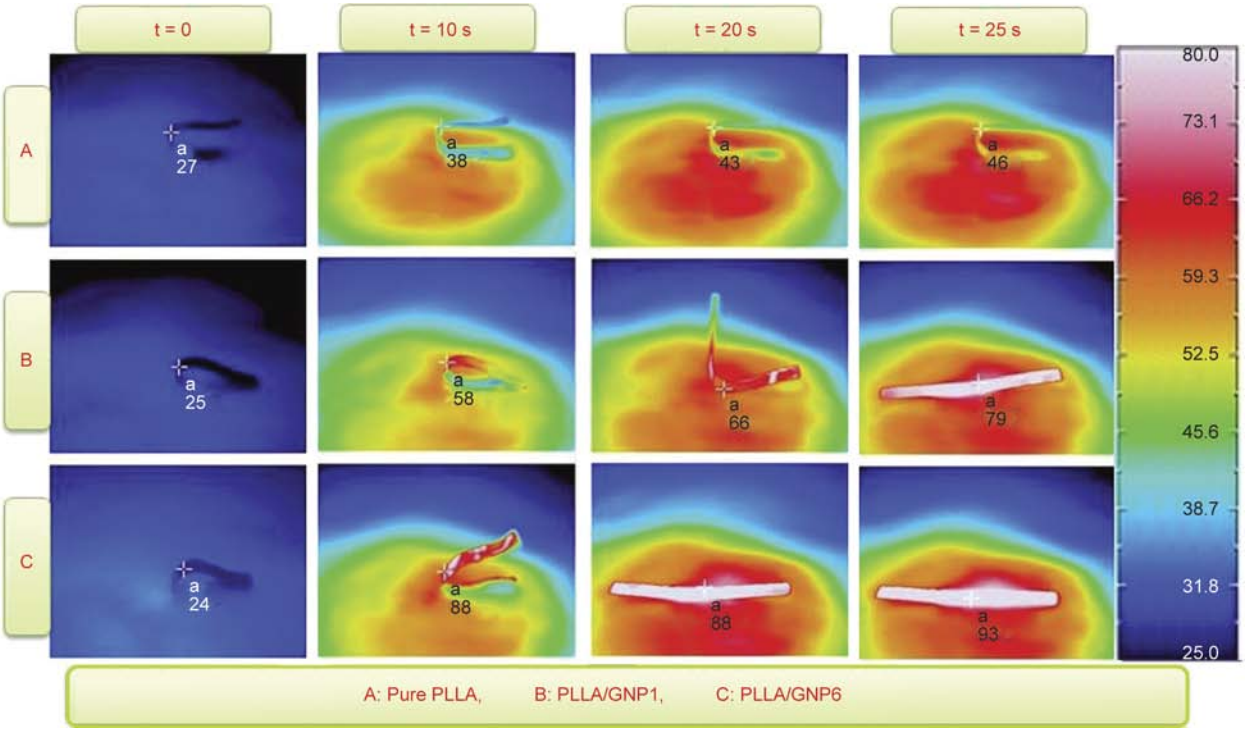

Figure 7. Temperature distribution snapshots of pure PLLA and its nanocomposites during infrared actuation recovery

Table 3. Start time of recovery, equilibrium R_r and max. surface temperature at equilibrium recovery of PLLA/GNPs composites activated by IR

	PLLA	PLLA-GNP0.5	PLLA-GNP1	PLLA-GNP2	PLLA-GNP4	PLLA-GNP6
Start time [s]	154	23	16	14	11	8
Equilibrium R_r [%]	86	98	99	98	94	95
Max. surface temperature at equilibrium recovery	79	86	90	96	103	110

amorphous phase to the rubbery state. This phenomenon is done through energy absorption and chain motion due to entropic elasticity. Although higher GNPs loading helps more energy absorption, but at the same time, it can disturb chain recovery. This should depress shape recovery at graphene loading of higher 2 wt%. The pure PLLA reaches to equilibrium recovery of 86% after 5 min, indicating low infrared absorbability of this polymer.

The maximum surface temperature of samples due to exerting infrared light is shown in Figure 7 and written in Table 3. PLLA may crystallize upon heating over 95°C during infrared heating which would worse its SME remarkably. Therefore, over heating by infrared would be a big concern in the cyclic activation test. To overcome this problem, the light intensity should be adjusted in such a way that leads to not more than 90~95 °C surface temperature increment.

4. Conclusions

In summary, using GNPs in shape memory PLLA enables infrared triggering of shape memory PLLA which is very intriguing in novel applications due to remote control ability of this biodegradable SMP. The effect of GNPs on morphology, crystallinity and thermomechanical properties of PLLA and their correlation to shape memory performance were studied. GNPs had a fine and uniform dispersion in the PLLA matrix at low fractions of GNPs which was resulted in remarkable enhancement of PLLA crystallinity due to nucleating effect of GNPs that was also confirmed by WAXD results. At higher GNPs loading (beyond 2 wt%), the particles started aggregating which was proved by FEG-SEM images and resulted in crystallinity reduction. Thermo-mechanical properties of PLLA were improved by GNPs addition and were leaded to the enhancement of shape memory performance. Recovery ratio of pure PLLA by infrared triggering was only 86% which reached to more than 95% in all of the nanocomposites. Meanwhile, improved mechanical properties of nanocomposites resulted in higher stress deformation of SMPs that is a positive point in SMPs. Finally, compared to pure PLLA, PLLA-graphene nanocomposites showed higher shape memory recovery, stronger recovery stress and quicker response to the stimulus in both activating method.

Acknowledgements

The authors would like to thank Dr. Chiara Ferrari (for thermo-camera photos), Dr. Mauro Zapparoli (for FEG-SEM images) and Dr. Massimo Tonelli (for WAXD analysis) in the CIGS center of University of Modena and Reggio Emillia.

References

[1] Liu C., Qin H., Mather P. T.: Review of progress in shape-memory polymers. Journal of Materials Chemistry, **17**, 1543–1558 (2007). DOI: 10.1039/b615954k

[2] Stylios G. K., Wan T.: Shape memory training for smart fabrics. Transactions of the Institute of Measurement and Control, **29**, 321–336 (2007). DOI: 10.1177/0142331207069479

[3] Hu J.: Shape memory polymers and textiles. Woodhead Publishing Limited, Cambridge (2007).

[4] Sokolowski W., Metcalfe A., Hayashi S., Yahia L., Raymond J.: Medical applications of shape memory polymers. Biomedical Materials, **2**, S23–S27 (2007). DOI: 10.1088/1748-6041/2/1/S04

[5] Maitland D., Benett W. J., Bearinger J. P., Wilson T. S., Small W., Schumann D. L., Jensen W. A., Ortega J. M., Marion J. E., Loge J. M.: Shape memory polymer medical device. U.S. Patent 7744604 B2, USA (2010).

[6] Morshedian J., Khonakdar H. A., Rasouli S.: Modeling of shape memory induction and recovery in heat-shrinkable polymers. Macromolecular Theory and Simulations, **14**, 428–434 (2005). DOI: 10.1002/mats.200400108

[7] Kolesov I., Dolynchuk O., Radusch H-J.: Shape-memory behavior of cross-linked semi-crystalline polymers and their blends. Express Polymer Letters, **9**, 255–276 (2015). DOI: 10.3144/expresspolymlett.2015.24

[8] Raja M., Ryu S. H., Shanmugharaj A. M.: Thermal, mechanical and electroactive shape memory properties of polyurethane (PU)/poly(lactic acid) (PLA)/CNT nanocomposites. European Polymer Journal, **49**, 3492–3500 (2013). DOI: 10.1016/j.eurpolymj.2013.08.009

[9] Leng J., Lan X., Liu Y., Du S.: Shape-memory polymers and their composites: Stimulus methods and applications. Progress in Materials Science, **56**, 1077–1135 (2011).
DOI: 10.1016/j.pmatsci.2011.03.001

[10] Xie T.: Recent advances in polymer shape memory. Polymer, **52**, 4985–5000 (2011).
DOI: 10.1016/j.polymer.2011.08.003

[11] Hu J., Zhu Y., Huang H., Lu J.: Recent advances in shape–memory polymers: Structure, mechanism, functionality, modeling and applications. Progress in Polymer Science, **37**, 1720–1763 (2012).
DOI: 10.1016/j.progpolymsci.2012.06.001

[12] Huang W. M., Zhao Y., Wang C. C., Ding Z., Purnawali H., Tang C., Zhang J. L.: Thermo/chemo-responsive shape memory effect in polymers: A sketch of working mechanisms, fundamentals and optimization. Journal of Polymer Research, **19**, 9952/1–9952/34 (2012).
DOI: 10.1007/s10965-012-9952-z

[13] Wang C. C., Huang W. M., Ding Z., Zhao Y., Purnawali H.: Cooling-/water-responsive shape memory hybrids. Composites Science and Technology, **72**, 1178–1182 (2012).
DOI: 10.1016/j.compscitech.2012.03.027

[14] Lu H., Liu Y., Gou J., Leng J., Du S.: Electroactive shape-memory polymer nanocomposites incorporating carbon nanofiber paper. International Journal of Smart and Nano Materials, **1**, 2–12 (2010).
DOI: 10.1080/19475411003612749

[15] Buckley P. R., McKinley G. H., Wilson T. S., Small W., Benett W. J., Bearinger J. P., McElfresh M. W., Maitland D. J.: Inductively heated shape memory polymer for the magnetic actuation of medical devices. IEEE Transactions on Biomedical Engineering, **53**, 2075–2083 (2006).
DOI: 10.1109/TBME.2006.877113

[16] Sodhi J. S., Rao I. J.: Modeling the mechanics of light activated shape memory polymers. International Journal of Engineering Science, **48**, 1576–1589 (2010).
DOI: 10.1016/j.ijengsci.2010.05.003

[17] Park J. H., Kim B. K.: Infrared light actuated shape memory effects in crystalline polyurethane/graphene chemical hybrids. Smart Materials and Structures, **23**, 025038/1–025038/7 (2014).
DOI: 10.1088/0964-1726/23/2/025038

[18] Paakinaho K., Heino H., Pelto M., Hannula M., Törmälä P., Kellomäki M.: Programmed water-induced shape-memory of bioabsorbable poly(D,L-lactide): Activation and properties in physiological temperature. Journal of Materials Science: Materials in Medicine, **23**, 613–621 (2012).
DOI: 10.1007/s10856-011-4538-6

[19] Huang W. M., Song C. L., Fu Y. Q., Wang C. C., Zhao Y., Purnawali H., Lu H. B., Tang C., Ding Z., Zhang J. L.: Shaping tissue with shape memory materials. Advanced Drug Delivery Reviews, **65**, 515–535 (2013).
DOI: 10.1016/j.addr.2012.06.004

[20] Karger-Kocsis J., Kéki S.: Biodegradable polyester-based shape memory polymers: Concepts of (supra) molecular architecturing. Express Polymer Letters, **8**, 397–412 (2014).
DOI: 10.3144/expresspolymlett.2014.44

[21] Nabipour Chakoli A., Sui J., Amirian M., Cai W.: Crystallinity of biodegradable polymers reinforced with functionalized carbon nanotubes. Journal of Polymer Research, **18**, 1249–1259 (2011).
DOI: 10.1007/s10965-010-9527-9

[22] Zhang X., Lu X., Wang Z., Wang J., Sun Z.: Biodegradable shape memory nanocomposites with thermal and magnetic field responsiveness. Journal of Biomaterials Science, Polymer Edition, **24**, 1057–1070 (2013).
DOI: 10.1080/09205063.2012.735098

[23] Lu X. L., Cai W., Gao Z., Tang W. J.: Shape memory effects of poly(L-lactide) and its copolymer with poly (ε-caprolactone). Polymer Bulletin, **58**, 381–391 (2007).
DOI: 10.1007/s00289-006-0680-6

[24] Meng Q., Hu J., Ho K., Ji F., Chen S.: The shape memory properties of biodegradable chitosan/poly(L-lactide) composites. Journal of Polymers and the Environment, **17**, 212–224 (2009).
DOI: 10.1007/s10924-009-0141-z

[25] Hamad K., Kaseem M., Yang H. W., Deri F., Ko Y. G.: Properties and medical applications of polylactic acid: A review. Express Polymer Letters, **9**, 435–455 (2015).
DOI: 10.3144/expresspolymlett.2015.42

[26] Dong H. Q., Liu L. J., Li Y. Y.: Shape-memory behavior of poly(L-lactide)/poly(ε-caprolactone) blends. Advanced Materials Research, **226**, 171–174 (2011).
DOI: 10.4028/www.scientific.net/AMR.266.171

[27] Ghobadi E., Heuchel M., Kratz K., Lendlein A.: Influence of the addition of water to amorphous switching domains on the simulated shape-memory properties of poly(L-lactide). Polymer, **54**, 4204–4211 (2013).
DOI: 10.1016/j.polymer.2013.05.064

[28] Yan B., Gu S., Zhang Y.: Polylactide-based thermoplastic shape memory polymer nanocomposites. European Polymer Journal, **49**, 366–378 (2013).
DOI: 10.1016/j.eurpolymj.2012.09.026

[29] Lu X., Cai W., Zhao L.: Study on the shape memory behavior of poly(L-Lactide). Materials Science Forum, **475–479**, 2399–2402 (2005).
DOI: 10.4028/www.scientific.net/MSF.475-479.2399

[30] Wong Y. S., Xiong Y., Venkatraman S. S., Boey F. Y. C.: Shape memory in un-cross-linked biodegradable polymers. Journal of Biomaterials Science, Polymer Edition, **19**, 175–191 (2008).
DOI: 10.1163/156856208783432516

[31] Wong Y. S., Venkatraman S. S.: Recovery as a measure of oriented crystalline structure in poly(L-lactide) used as shape memory polymer. Acta Materialia, **58**, 49–58 (2010).
DOI: 10.1016/j.actamat.2009.08.075

[32] Zheng X., Zhou S., Li X., Weng J.: Shape memory properties of poly(D,L-lactide)/hydroxyapatite composites. Biomaterials, **27**, 4288–4295 (2006). DOI: 10.1016/j.biomaterials.2006.03.043

[33] Paakinaho K., Hukka T. I., Kastinen T., Kellomäki M.: Demonstrating the mechanism and efficacy of water-induced shape memory and the influence of water on the thermal properties of oriented poly(D,L-lactide). Journal of Applied Polymer Science, **130**, 4209–4218 (2013). DOI: 10.1002/app.39513

[34] Zheng X., Zhou S., Xiao Y., Yu X., Li X., Wu P.: Shape memory effect of poly(D,L-lactide)/Fe_3O_4 nanocomposites by inductive heating of magnetite particles. Colloids and Surfaces B: Biointerfaces, **71**, 67–72 (2009). DOI: 10.1016/j.colsurfb.2009.01.009

[35] Potts J. R., Dreyer D. R., Bielawski C. W., Ruoff R. S.: Graphene-based polymer nanocomposites. Polymer, **52**, 5–25 (2011). DOI: 10.1016/j.polymer.2010.11.042

[36] Stankovich S., Dikin D. A., Dommett G. H. B., Kohlhaas K. M., Zimney E. J., Stach E. A., Piner R. D., Nguyen S. T., Ruoff R. S.: Graphene-based composite materials. Nature, **442**, 282–286 (2006). DOI: 10.1038/nature04969

[37] Kashif M., Chang Y-W.: Supramolecular hydrogen-bonded polyolefin elastomer/modified graphene nanocomposites with near infrared responsive shape memory and healing properties. European Polymer Journal, **66**, 273–281 (2015). DOI: 10.1016/j.eurpolymj.2015.02.007

[38] Feng Y., Qin M., Guo H., Yoshino K., Feng W.: Infrared-actuated recovery of polyurethane filled by reduced graphene oxide/carbon nanotube hybrids with high energy density. ACS Applied Materials and Interfaces, **5**, 10882–10888 (2013). DOI: 10.1021/am403071k

[39] Tang Z., Kang H., Wei Q., Guo B., Zhang L., Jia D.: Incorporation of graphene into polyester/carbon nanofibers composites for better multi-stimuli responsive shape memory performances. Carbon, **64**, 487–498 (2013). DOI: 10.1016/j.carbon.2013.07.103

[40] Wang H., Qiu Z.: Crystallization kinetics and morphology of biodegradable poly(L-lactic acid)/graphene oxide nanocomposites: Influences of graphene oxide loading and crystallization temperature. Thermochimica Acta, **527**, 40–46 (2012). DOI: 10.1016/j.tca.2011.10.004

[41] Wang H., Qiu Z.: Crystallization behaviors of poly(L-lactic acid)/graphene oxide nanocomposites from the amorphous state. Thermochimica Acta, **526**, 229–236 (2011). DOI: 10.1016/j.tca.2011.10.006

[42] Sabzi M., Jiang L., Liu F., Ghasemi I., Atai M.: Graphene nanoplatelets as poly(lactic acid) modifier: Linear rheological behavior and electrical conductivity. Journal of Materials Chemistry A, **1**, 8253–8261 (2013). DOI: 10.1039/c3ta11021d

[43] Norazlina H., Kamal Y.: Graphene modifications in polylactic acid nanocomposites: A review. Polymer Bulletin, **72**, 931–961 (2015). DOI: 10.1007/s00289-015-1308-5

[44] Murariu M., Dechief A. L., Bonnaud L., Paint Y., Gallos A., Fontaine G., Bourbigot S., Dubois P.: The production and properties of polylactide composites filled with expanded graphite. Polymer Degradation and Stability, **95**, 889–900 (2010). DOI: 10.1016/j.polymdegradstab.2009.12.019

[45] Garlotta D.: A literature review of poly(lactic acid). Journal of Polymers and the Environment, **9**, 63–84 (2002). DOI: 10.1023/a:1020200822435

[46] Lendlein A.: Characterization methods for shape-memory polymers. in 'Shape-memory polymer' (eds.: Wagermaier W., Kratz K., Heuchel M., Lendlein A.) Springer, Berlin, Vol 226, 97–145 (2010).

[47] Tobushi H., Hayashi S., Hoshio K., Makino Y., Miwa N.: Bending actuation characteristics of shape memory composite with SMA and SMP. Journal of Intelligent Material Systems and Structures, **17**, 1075–1081 (2006). DOI: 10.1177/1045389x06064885

[48] Leng J., Wu X., Liu Y.: Infrared light-active shape memory polymer filled with nanocarbon particles. Journal of Applied Polymer Science, **114**, 2455–2460 (2009). DOI: 10.1002/app.30724

[49] Huang H-D., Ren P-G., Xu J-Z., Xu L., Zhong G-J., Hsiao B. S., Li Z-M.: Improved barrier properties of poly(lactic acid) with randomly dispersed graphene oxide nanosheets. Journal of Membrane Science, **464**, 110–118 (2014). DOI: 10.1016/j.memsci.2014.04.009

[50] Yu K., Liu Y., Leng J.: Shape memory polymer/CNT composites and their microwave induced shape memory behaviors. RSC Advances, **4**, 2961–2968 (2014). DOI: 10.1039/c3ra43258k

[51] Xu J., Shi W., Pang W.: Synthesis and shape memory effects of Si–O–Si cross-linked hybrid polyurethanes. Polymer, **47**, 457–465 (2006). DOI: 10.1016/j.polymer.2005.11.035

[52] Wunderlich B.: Basics of thermal analysis. in 'Thermal analysis of polymeric materials' (ed.: Wunderlich B.) Springer, Berlin, 71–188 (2005).

[53] Lu X. L., Sun Z. J., Cai W., Gao Z. Y.: Study on the shape memory effects of poly(L-lactide-*co*-ε-caprolactone) biodegradable polymers. Journal of Materials Science: Materials in Medicine, **19**, 395–399 (2008). DOI: 10.1007/s10856-006-0100-3